



TECHNISCHE
UNIVERSITÄT
WIEN

DISSERTATION

Nonlinear Characterization and Modeling of Magnetic Tunnel Junction (MTJ)-Based Magnetic Sensors

submitted in partial fulfillment of the requirements for the degree of
Doctor of Philosophy

by

Ekaterina Auerbach

Student number: 01529334

The dissertation was reviewed by

Priv.-Doz. Dr. techn. Dieter Süß

Prof. Dr. Michael Feiginov

Dr. habil. Ursula Ebels

Vienna, 21.05.2019



TECHNISCHE
UNIVERSITÄT
WIEN

DISSERTATION

Nichtlineare Charakterisierung und Modellierung von magnetische Tunnelwiderstand basierten Magnetsensoren

ausgeführt zum Zwecke der Erlangung des akademischen Grades einer
Doktorin der technischen Wissenschaften

von

Ekaterina Auerbach

Matrikelnummer: 01529334

Die Dissertation wurde begutachtet von:

Priv.-Doz. Dr. techn. Dieter Süss

Prof. Dr. Michael Feiginov

Dr. habil. Ursula Ebels

Wien, 21.05.2019

Erklärung

Ekaterina Auerbach
Rue Belliard 197, Bte. 10
1040 Brüssel, Belgien

Ich erkläre hiermit an Eides Statt durch meine eigenhndige Unterschrift, dass ich die vorliegende Arbeit selbständig verfasst und keine anderen als die angegebenen Quellen und Hilfsmittel verwendet habe. Alle Stellen, die wörtlich oder inhaltlich den angegebenen Quellen entnommen wurden, sind als solche kenntlich gemacht. Die vorliegende Arbeit wurde bisher in gleicher oder ähnlicher Form noch nicht als Magister-/Master-/Diplomarbeit/Dissertation eingereicht.

Ort, Datum

Ekaterina Auerbach

Abstract

As magnetic nanodevices (*e.g.*, magnetic sensors) continue to shrink in size, the inherent nonlinear nature of magnetization dynamics may emerge during device operation. Firstly, the energy barrier separating the two possible magnetic states is directly proportional to the nanomagnet's volume. Thus, thermal fluctuations in these nanomagnets might cause thermally-induced transitions from one state to another. Secondly, for a smaller ferromagnetic sample, the same bias voltage corresponds to a larger current density. The latter may result in large-angle magnetization precession where the nonlinear nature of the Landau-Lifshitz-Gilbert (LLG) equation is especially pronounced. To optimize these devices and/or choose the most favorable operating point, one must first develop a characterization protocol tailored to nonlinear measurements in the presence of dynamic effects.

As these effects occur in the gigahertz range, *i.e.*, ferromagnetic resonance (FMR) in nanoelements, their characterization would greatly benefit from advances in microwave measurement techniques. In particular, a comprehensive nonlinear analysis of magnetic sensors can be accomplished using a nonlinear vector network analyzer, which measures the incident and reflected waves' (A_1 and B_1 , respectively) magnitudes and phases at the excitation frequency and harmonic components to which energy may be transferred due to the device's nonlinear characteristics.

The problem studied in this thesis is the identification of the new resonances at fractional frequencies of the free layer (FL) FMR mode resulting from the nonlinear nature of the spin-torque (ST)-induced magnetization dynamics. We discovered that all characterized magnetic sensors' DC responses reveal peaks at frequencies that are the integer fractions ($1/2$, $1/3$, $1/4$, and $1/6$) of the devices' natural FL FMR frequency. These peaks, in turn, generate the second and third harmonics of B_1 . New spectral lines at fractional frequencies of the devices' FMR modes were observed using an alternative measurement technique, and the results of this study are also reported in this work.

A complimentary micromagnetic study showed that the experimentally observed DC response at frequencies that are the integer fractions of the FL's resonant precession frequency can be defined by a low-order nonlinearity and strong magnetodipolar feedback between the magnetic layers adjacent to an MgO barrier. Additionally, the harmonic response is enhanced by the mutual ST effect between these layers.

Most importantly, strong magnetodipolar feedback permitted sub-harmonic injection locking within a wide range of integer fractions, which can be used in the development of a new generation of frequency multipliers.

Acknowledgements

I would like to acknowledge the help and support of those people who directly and indirectly contributed to the completion of this work. I will mention them in the order in which they entered my life during this Ph.D. journey.

Firstly, I would like to thank Savas Gider for mentoring me since the day he hired me for my first internship in the United States of America and introducing me to magnetism and its applications. Besides closely supervising my work, he proposed the collaborative project between Western Digital (WD) and TU Wien that became the foundation of this thesis. Even after leaving WD, he never abstained from reviewing my results and sending me his valuable comments. I would also like to thank Daniele Mauri and Gonçalo Albuquerque for providing me with the samples and answering my inquiries when I needed specific information about a sample or WD's read head designs.

I am grateful to my research advisor, Prof. Dieter Süß, for his assistance with my Ph.D. application and continued support. He carefully considered all my initiatives, though not all of them yielded fruitful results. None of this work would have been accomplished if Prof. Holger Arthaber had not let me use his laboratory where most of the presented measurements originate. I spent an inordinate amount of time at his RF lab learning advanced microwave measurement techniques and engaging in conversations with Norbert Leder, Bernhard Pichler, and others. Norbert always was ready with suggestions for new experiments when I had completely exhausted my stockpile of ideas. He belongs to a small group of engineers who enjoy considering the physical nature of the observed experimental phenomena when interpreting measurements or designing new experiments. As for Bernhard, only because of his “successfully fried” device under test did we have a chance to obtain the nonlinear vector network analyzer (NVNA) measurements. Lucky me!

Even though my Erasmus+ research exchange was a slight detour in completing this work, I am happy to have had spent this time at the ELEC Department of the Vrije Universiteit Brussel. Specifically, I would like to thank Prof. Yves Rolain for his help in interpreting my nonlinear measurements with his physical insights. Prof. Rolain and Norbert both are able to reflect on scientific problems beyond their discipline, which makes them extremely flexible scientists. I hope to acquire this quality one day, too.

Honestly, I do not think that I would have submitted this thesis without the mountainous help and support of Dr. Dmitry Berkov. He helped me structure my work so that it no longer seemed like a incoherent bunch of observations. During my research exchange at the General Numerics Research Lab, Dr. Berkov treated me like one of his colleagues and

taught me basically everything I know about micromagnetic modeling. His help prevented me from become completely disillusioned with this field... and my work.

Lastly, I want to thank my family, the Auerbachs and the Chernobrovkins. This voyage could not have been completed without the support and love of my husband. I am terribly happy that all of them can finally witness my success.

Contents

Abbreviations	vi
1 Introduction to experimental and numerical studies of magnetization dynamics	1
1.1 Fundamentals of magnetization dynamics	1
1.2 Ferromagnetic resonance characterization	11
1.3 Numerical modeling of magnetization dynamics	15
2 Read head system	26
2.1 Magnetic read sensors	26
2.2 Ferromagnetic resonance frequencies	29
2.3 Tunnel magnetoresistance effect	31
2.4 Summary	31
3 Direct observation of high-frequency magnetization dynamics under DC bias	32
3.1 Spectrum analysis in frequency domain	32
3.2 Waveform analysis in time domain	36
3.3 Summary	39
4 Coupling between the AC excitation signal and magnetization precession	40
4.1 Vector network analysis in frequency domain	40
4.2 Strong coupling between the AC excitation signal's phase noise floor and magnetization precession	45
4.3 Summary	50
5 DC and harmonic response resulting from strongly nonlinear magnetization dynamics	51
5.1 Steady-state DC readout	53
5.2 Harmonic response under one- and two-tone AC excitation signal	56
5.2.1 One-tone measurement	56
5.2.2 Two-tone measurement	59
5.3 Probing nonlinear magnetization dynamics with a nonlinear vector network analyzer	61
5.4 Summary	67
6 Micromagnetic simulations of strongly nonlinear magnetization dynamics	68

6.1	Modeling methodology	68
6.2	Modeling considerations	69
6.3	Results and discussion	73
6.3.1	DC response	73
6.3.2	Harmonic response	77
6.4	Summary	78
7	Conclusion	79
	Appendices	80
A	Noise reduction <i>via</i> spectral subtraction and signal filtering in the frequency domain	80
B	Smith chart analysis: single resonant mode	82
C	Anomalous sample	83
D	AC-power-to-current conversion	84
E	Effect of magnetic parameters on read sensor's dynamic regime	85
F	Effect of spin-torque parameters on read sensor's DC response	87
	References	88

Abbreviations

AC alternating current. 12–15, 32, 40, 45–47, 50, 52–56, 63–66, 69, 70, 77, 79, 80, 83–85

AFM antiferromagnetic. 28, 29, 70, 71

ASD amplitude spectral density. 34–36

BLS Brillouin light scattering. 11

CPP current-perpendicular-to-plane. 55, 71

DC direct current. 12–15, 32–35, 38–40, 42–56, 58, 61–67, 69, 70, 72–79, 81, 83, 85, 87

DFL dual free layer. 28, 29, 34, 35, 39

DUT device under test. 32, 40, 42, 55, 56, 59–62, 82

EM electromagnetic. 28

ESD electrostatic discharge. 27

FD finite-difference. 18–20

FE finite element. 18, 19

FFT Fast Fourier transform. 19

FL free layer. 7, 14, 15, 28–30, 32–36, 38, 39, 43, 45–49, 52, 54, 55, 63, 64, 66–79, 81, 85, 86

FMR ferromagnetic resonance. 11–13, 15, 29, 30, 32–36, 39, 40, 43–50, 55, 61, 63, 67, 68, 70–74, 76–79, 82, 83, 85

GMR giant magnetoresistance. 32, 71

IF intermediate frequency. 62

IFBW intermediate frequency bandwidth. 14, 43, 44, 46, 64–66, 83

IM inter-modulation. 59, 60

IM3 inter-modulation products of the third order. 59, 60

LL Landau-Lifshitz. 4

LLB Landau-Lifshitz-Bloch. 6

LLG Landau-Lifshitz-Gilbert. 4–7, 19, 20, 22–25, 68, 69

MOKE magneto-optical Kerr. 11

MSW-SER magnetostatic wave straight-edge resonator. 12

MTJ magnetic tunnel junction. 26, 30, 31, 40, 44, 45, 52–54, 58, 68–71, 76, 79

NL noise level. 46, 47

NVNA nonlinear vector network analyzer. 15, 61–65, 67, 73, 77, 83

ODE ordinary differential equation. 23, 24

PL pinned layer. 7, 15, 28–30, 32, 33, 36, 43, 47, 48, 52, 55, 64, 68–73, 75, 76, 78, 81

RBW resolution bandwidth. 13, 33, 34, 47, 48

RF radio frequency. 10, 17, 18, 27, 28, 31, 46, 56, 58

RMS root-mean-square. 41, 63, 84

SFL single free layer. 28, 29, 32, 33

SH stripe height. 30, 38

SNR signal-to-noise ratio. 36, 81

ST spin-torque. 7, 8, 10, 11, 14, 15, 30, 32, 33, 36, 40, 51–53, 55, 58, 68–70, 73–75, 78, 79, 85, 87

STFT short-time Fourier transform. 37, 38

T-FMR thermal noise ferromagnetic resonance. 42, 46–48, 63

TMR tunnel magnetoresistance. 26–32, 40, 51–54, 58, 69, 74, 76, 77, 84

TR-MOKE time-resolved magneto-optical Kerr. 11

TR-SKM time-resolved scanning Kerr microscopy. 11

VNA vector network analyzer. 13, 14, 27, 28, 40, 42–46, 61, 62

VNA-FMR vector network analyzer-based ferromagnetic resonance. 13–15, 40, 42, 46,
54

1 Introduction to experimental and numerical studies of magnetization dynamics

1.1 Fundamentals of magnetization dynamics

The mesoscopic theory of magnetism bridges the gap between Maxwell's macroscopic theory of electromagnetic fields, which describes bulk magnetic properties, and quantum theory that describes magnetic properties on the atomic level. Micromagnetism treats the ferromagnets' magnetic state *via* the local magnetization vector field $\mathbf{M}(\mathbf{r}, t)$. At temperatures much lower than the Curie temperature T_c , its magnitude is equal to the spontaneous magnetization [1]:

$$|\mathbf{M}(\mathbf{r}, t)| = M_s. \quad (1)$$

The magnetization magnitude is assumed to remain constant:

$$\mathbf{M} = M_s \mathbf{m}, \quad \mathbf{m} \cdot \mathbf{m} = 1. \quad (2)$$

In the ground state, the exerted torque onto the magnetization \mathbf{M} is zero [1]:

$$\mathbf{m} \times \mathbf{H}_{\text{eff}} = 0, \quad (3)$$

where the effective field \mathbf{H}_{eff}

$$\mathbf{H}_{\text{eff}} = -\frac{1}{\mu_0 M_s} \frac{\delta \varepsilon}{\delta \mathbf{m}} \quad (4)$$

is the negative variational derivative of the energy density ε with respect to magnetization.

The corresponding micromagnetic energy has the following contributions [1, 2]:

$$E = \int_V \left[-\mu_0 M_s \mathbf{m} \cdot \mathbf{H}_{\text{ext}} + \varepsilon_{\text{an}}(\mathbf{m}) + A (\nabla \mathbf{m})^2 - \frac{1}{2} \mu_0 M_s \mathbf{m} \cdot \mathbf{H}_{\text{md}} \right] d^3 r. \quad (5)$$

Equation (5) describes the interaction of the local magnetization \mathbf{M} with an external field and crystal lattice as well as magnetic moments with one another. The latter consists of

short-range quantum mechanical exchange and long-range magnetodipolar interactions. The energy in the external field \mathbf{H}_{ext} orients the magnetization parallel to the external field. The magnetocrystalline anisotropy energy describes the interaction of the magnetization with the crystal lattice. It orients the magnetization in the preferred direction, which depends on the crystalline structure. The exchange energy is responsible for the atomic magnetic moments' alignment within the ferromagnetic body. It penalizes nonuniformities and favors uniform magnetization dynamics. The magnetodipolar energy accounts for the dipole-dipole interaction of magnetic moments within the ferromagnet and favors the existence of magnetic domains [3].

Other energy contributions may include, *e.g.*, energy due to magnetostrictive interactions between elastic stress and spontaneous magnetization. Specifically, the stress-induced displacement influences the magnetic behavior (*e.g.*, domain wall displacement), whereas magnetic properties can alter the elastic ones (*e.g.*, elongation in the direction of magnetization) [4].

Each energy term contributes to the effective field [1, 2]:

$$\mathbf{H}_{\text{eff}} = \mathbf{H}_{\text{ext}} + \mathbf{H}_{\text{an}} + \mathbf{H}_{\text{exch}} + \mathbf{H}_{\text{md}}. \quad (6)$$

\mathbf{H}_{ext} is the external field (also known as Zeeman field).

\mathbf{H}_{an} and \mathbf{H}_{exch} are the anisotropy and exchange fields [5]:

$$\begin{aligned} \mathbf{H}_{\text{an}} &= -\frac{1}{\mu_0 M_s} \frac{\delta \varepsilon_{\text{an}}}{\delta \mathbf{m}}, \\ \mathbf{H}_{\text{exch}} &= \frac{2A}{\mu_0 M_s} \nabla^2 \mathbf{m}, \end{aligned} \quad (7)$$

where ε_{an} is the anisotropy energy density. A is the exchange stiffness constant; its typical value in ferromagnets is 10^{-11} J/m.

The uniaxial anisotropy effect is the most common. Assuming that $\mathbf{m} = \mathbf{M}/M_s$ coincides with the z -axis, the anisotropy energy density may be written as an even function of $m_z = \cos \theta$, or, equivalently,

$$m_x^2 + m_y^2 = 1 - m_z^2 = \sin^2 \theta. \quad (8)$$

The anisotropy energy density can be expanded as a series:

$$\varepsilon_{\text{an}}(\mathbf{m}) = K_1^{\text{un}} \sin^2 \theta + K_2^{\text{un}} \sin^4 \theta + K_3^{\text{un}} \sin^6 \theta + \dots, \quad (9)$$

where θ is the angle between the direction of \mathbf{m} and the crystal's anisotropy axis.

If $K_1^{\text{un}} > 0$, the anisotropy energy is minimal at $\theta = 0$ and $\theta = \pi$. Then, \mathbf{m} lies along either $+z$ or $-z$ axis. This condition is referred to as the easy-axis anisotropy. Alternatively, if $K_1^{\text{un}} < 0$, the anisotropy energy is minimal at $\theta = \pi/2$. Then, \mathbf{m} may point in any direction in the x - y plane. This condition is known as the easy-plane anisotropy.

In a cubic crystal,

$$\varepsilon_{\text{an}}(\mathbf{m}) = K_1^{\text{cub}}(\alpha_1^2 \alpha_2^2 + \alpha_2^2 \alpha_3^2 + \alpha_1^2 \alpha_3^2) + \dots, \quad (10)$$

where α_1 , α_2 , and α_3 are the components of \mathbf{m} in a local coordinate system. In Eqs. (9) and (10), K_i^{un} and K_i^{cub} are the corresponding anisotropy constants defined as energy per unit volume [J/m³].

If $K_1^{\text{cub}} > 0$, the anisotropy energy has six minima corresponding to $\pm x$, $\pm y$, and $\pm z$ directions. If $K_1^{\text{cub}} < 0$, the anisotropy energy minima point in the direction of the cube's vertices. This condition is referred to as the hard-axis anisotropy [6].

The magnetodipolar field \mathbf{H}_{md} can be introduced in the following manner. The condition $\nabla \cdot \mathbf{B} = 0$ and the relationship between \mathbf{B} , \mathbf{H} , and \mathbf{M}

$$\mathbf{H} = \frac{1}{\mu_0} \mathbf{B} - \mathbf{M} \quad (11)$$

lead to

$$\nabla \cdot \mathbf{H} = -\nabla \cdot \mathbf{M}. \quad (12)$$

Introducing a scalar quantity ρ_{mag}

$$\rho_{\text{mag}} = -\nabla \cdot \mathbf{M}, \quad (13)$$

we arrive at

$$\nabla \cdot \mathbf{H} = \rho_{\text{mag}}. \quad (14)$$

This equation mimics the corresponding Maxwell's equation that states that electric charges generate electric fields. Even though magnetic charges (as well as the magnetic charge density ρ_{mag} introduced above) do not exist, this concept is a convenient mathematical tool for evaluating the magnetodipolar energy [3].

The magnetodipolar field is determined by solving the following equations [1]:

$$\begin{aligned}\nabla \times \mathbf{H}_{\text{md}} &= 0, \\ \nabla \cdot \mathbf{H}_{\text{md}} &= -\nabla \cdot \mathbf{M}.\end{aligned}\tag{15}$$

If the system is not at equilibrium, $\mathbf{M} \times \mathbf{H}_{\text{eff}} \neq 0$, the local magnetization dynamically evolves. Landau and Lifshitz originally described the effective-field-induced magnetization dynamics as follows [1]:

$$\frac{d\mathbf{m}}{dt} = -\gamma_0 \mathbf{m} \times \mathbf{H}_{\text{eff}},\tag{16}$$

where $\gamma_0 = 2.2 \times 10^5 \text{ A}^{-1}\text{ms}^{-1}$ is the absolute value of the gyromagnetic ratio associated with the electron's spin. It determines the precession rate. This equation, however, does not describe the interactions with a thermal bath that lead to damping. The following Landau-Lifshitz (LL) and Landau-Lifshitz-Gilbert (LLG) formulations account for the energy decrease due to these interactions by introducing an additional damping term [1]:

$$\frac{d\mathbf{m}}{dt} = -\gamma \mathbf{m} \times \mathbf{H}_{\text{eff}} - \lambda \gamma \mathbf{m} \times (\mathbf{m} \times \mathbf{H}_{\text{eff}})\tag{17}$$

and

$$\frac{d\mathbf{m}}{dt} = -\gamma_0 \mathbf{m} \times \mathbf{H}_{\text{eff}} + \alpha \mathbf{m} \times \frac{d\mathbf{m}}{dt},\tag{18}$$

where α is the (dimensionless) Gilbert damping.

Equation (18) is inapplicable in its original form because it contains the time derivative of magnetization on both right- and left-hand-side. Multiplying both sides of Eq. (18) by \mathbf{m} , using the vector identity $\mathbf{a} \times (\mathbf{b} \times \mathbf{c}) = \mathbf{b}(\mathbf{a} \cdot \mathbf{c}) - \mathbf{c}(\mathbf{a} \cdot \mathbf{b})$, and observing that $\mathbf{m} \cdot d\mathbf{m}/dt = 0$, we arrive to the LL equation in the Gilbert form [1]:

$$\frac{d\mathbf{m}}{dt} = -\frac{\gamma_0}{1 + \alpha^2} \mathbf{m} \times \mathbf{H}_{\text{eff}} - \alpha \frac{\gamma_0}{1 + \alpha^2} \mathbf{m} \times (\mathbf{m} \times \mathbf{H}_{\text{eff}}).\tag{19}$$

Based on Eq. (19), Eqs. (17) and (18) are mathematically equivalent provided that $\gamma = \gamma_0/(1+\alpha^2)$ and $\lambda = \alpha$. Their treatment of damping, however, is quite different. In Eq. (17), the damping term pushes the magnetization in the direction of the effective field so that the magnetization magnitude is still preserved. This formulation, however, cannot be used in the overdamped regime ($\lambda \geq 1$) where the damping term dominates the magnetization motion. With increasing damping, Eq. (17) predicts acceleration of the magnetization motion, which contradicts the purpose of damping. On the contrary, Eq. (18) correctly describes the magnetization motion for all damping constants. This formulation for the magnetization dynamics conserves the magnetization magnitude in addition to insuring that the damping term slows down the magnetization precession [7].

Let's review some practical approaches to analysis of magnetization dynamics. If the spontaneous magnetization only slightly deviates from its equilibrium configuration, the resultant *small* magnetization motions can be described by the linearized LLG equation. Let's consider a small perturbation of $\delta\mathbf{m}$ around \mathbf{m}_0 :

$$\mathbf{m} = \mathbf{m}_0 + \delta\mathbf{m}, \quad (20)$$

where $|\delta\mathbf{m}| \ll 1$. As the perturbation must preserve the magnetization magnitude, $|\mathbf{m}|^2 = 1$, $\delta\mathbf{m}$ must be orthogonal to \mathbf{m}_0 :

$$\delta\mathbf{m} \cdot \mathbf{m}_0 = 0. \quad (21)$$

So, $\delta\mathbf{m}$ can be expressed in terms of the linear combination of unit vectors in the plane perpendicular to \mathbf{m}_0 :

$$\delta\mathbf{m} = \delta m_1 \mathbf{e}_1 + \delta m_2 \mathbf{e}_2, \quad (22)$$

where

$$\begin{aligned} \mathbf{e}_1 &= \frac{(\mathbf{e}_z \times \mathbf{m}_0) \times \mathbf{m}_0}{|(\mathbf{e}_z \times \mathbf{m}_0) \times \mathbf{m}_0|}, \\ \mathbf{e}_2 &= \frac{\mathbf{e}_z \times \mathbf{m}_0}{|\mathbf{e}_z \times \mathbf{m}_0|}. \end{aligned} \quad (23)$$

After substituting Eq. (22) into the LLG Eq. (18), linearizing the resultant equation with respect to $\delta\mathbf{m}$, and neglecting the higher-order terms, we arrive at the equation expressed

in terms of the *independent* magnetization components:

$$\frac{d}{dt} \begin{pmatrix} \delta m_1 \\ \delta m_2 \end{pmatrix} = A_0 \begin{pmatrix} \delta m_1 \\ \delta m_2 \end{pmatrix}. \quad (24)$$

The definition of A_0 can be found in [8].

Most applied problems (*e.g.*, spin injection, large-field dynamics) result in *large* magnetization motions where the nonlinear nature of the LLG equation is especially pronounced.

At high temperatures, one must use the Landau-Lifshitz-Bloch (LLB) formulation where the magnetization magnitude is no longer preserved [9]:

$$\frac{1}{\gamma} \frac{d\mathbf{m}}{dt} = -\mathbf{m} \times \mathbf{H}_{\text{eff}} + \alpha_{\parallel} \frac{(\mathbf{m} \cdot \mathbf{H}_{\text{eff}}) \mathbf{m}}{m^2} - \alpha_{\perp} \frac{\mathbf{m} \times (\mathbf{m} \times \mathbf{H}_{\text{eff}})}{m^2}, \quad (25)$$

where $\mathbf{m} = \mathbf{M}/M_s$. The longitudinal and transverse damping constants are given by

$$\alpha_{\parallel} = 2\lambda \frac{T}{3T_c}, \quad \alpha_{\perp} = \lambda \left[1 - \frac{T}{3T_c} \right], \quad (26)$$

where λ is the damping parameter describing coupling to the thermal bath at the atomic level.

In the LLB equation, the magnetization has two relaxation mechanisms: parallel and perpendicular to the external magnetic field. The relaxation of the magnetization component perpendicular to the external magnetic field is analogous to the LLG's damping term, while the magnetization component parallel to the external magnetic field relaxes to the equilibrium as a consequence of thermal excitations [9].

For a small ferromagnetic particle with an uniaxial anisotropy and zero external magnetic field, the energy barrier is directly proportional to its volume V_0 :

$$E = K_1^{\text{un}} V_0, \quad (27)$$

where K_1^{un} is the anisotropy constant. This energy barrier separates the two possible magnetic states [10].

Thus, thermal fluctuations in sub-micrometer ferromagnets might cause thermally-induced transitions from one state to another. In the presence of thermal excitations, proper description of magnetization dynamics in such tiny ferromagnets (*e.g.*, read heads) becomes vital.

In the LLG equation, thermal effects are accounted for by an additional contribution to the effective field \mathbf{H}_{eff} . This additional term \mathbf{H}_{th} describes random fluctuations induced by the interaction of the ferromagnet with the thermal bath, which leads to the following stochastic LLG equation [7]:

$$\frac{d\mathbf{m}}{dt} = -\gamma\mathbf{m} \times (\mathbf{H}_{\text{eff}} + \mathbf{H}_{\text{th}}) - \gamma\lambda\mathbf{m} \times [\mathbf{m} \times (\mathbf{H}_{\text{eff}} + \mathbf{H}_{\text{th}})], \quad (28)$$

where $\gamma = \gamma_0/(1+\alpha^2)$ and $\lambda = \alpha$.

In Eq. (28), the random fluctuation field \mathbf{H}_{th} has the following statistical properties:

$$\begin{aligned} \langle \mathbf{H}_{\xi,i}^{\text{th}} \rangle &= 0, \\ \langle \mathbf{H}_{\xi,i}^{\text{th}}(0) \mathbf{H}_{\psi,j}^{\text{th}}(t) \rangle &= 2D\delta(t)\delta_{ij}\delta_{\xi\psi}. \end{aligned} \quad (29)$$

Equations (29) mean that thermal fluctuations are uncorrelated in space and time. i, j are the discretization cell indices; $\xi, \psi = x, y, z$. The noise power D is proportional to the system temperature T :

$$D = \frac{\lambda}{1 + \lambda^2} \frac{kT}{\gamma\mu}, \quad (30)$$

where μ is the magnetic moment magnitude.

Equations (17) and (18) describe magnetization dynamics driven by the external magnetic field. Let's review how these classical formulations can incorporate the magnetization dynamics in multilayers driven by both the external magnetic field and *spin-polarized current*. In the simplest approximation, one of the multilayers' ferromagnetic layers is assumed to be perfectly fixed (pinned layer) while the other one (free layer) is free to move in response to the external magnetic field or current-induced torque. Assuming electron flow from the pinned layer to the free layer, electrons first become polarized by the pinned layer. Then, the difference in polarization generates torque onto the free layer. If the exerted torque is large enough, it excites the free layer's continuous precession or reverses the magnetization of the free layer (this effect is called "switching"). In the standard LLG [Eq. (18)], additional spin-torque (ST) terms—damping-like and field-like—account for the ST contribution [11, 12]:

$$\frac{d\mathbf{m}}{dt} = -\gamma_0\mathbf{m} \times \mathbf{H}_{\text{eff}} + \alpha\mathbf{m} \times \frac{d\mathbf{m}}{dt} - \gamma_0a_j\mathbf{m} \times (\mathbf{m} \times \mathbf{P}) - \gamma_0b_j\mathbf{m} \times \mathbf{P}, \quad (31)$$

where \mathbf{P} is the pinned layer's polarization; a_j and b_j are the ST coefficients proportional to the current density. In Eq. (31), the first ST term is the damping-like torque, also referred to as the Slonczewski torque. The second ST term is described as a contribution from an additional magnetic field (hence, the name “field-like”).

The ferromagnetic resonance is a practical approach to analysis of magnetization dynamics in magnetic nanostructures. It is characterized by a ferromagnetic resonance frequency ω_{res} and a linewidth $\Delta\omega$. Under the effective field \mathbf{H}_{eff} , perfectly aligned magnetic moments result in continuous precession characterized by a spatially uniform, homogeneous mode. Without damping (*i.e.*, $\alpha = 0$), the resonant precession frequency is equal to [13–16]:

$$\omega_{\text{res}} = \gamma_0 H_{\text{eff}}. \quad (32)$$

In the presence of damping, the resonant precession frequency has an additional frequency shift [15]:

$$\omega_{\text{res}} = \gamma_0 \sqrt{1 + \alpha^2} H_{\text{eff}}. \quad (33)$$

Equation (32), however, is valid only for a sphere with no shape anisotropy resulting from the demagnetizing field. Demagnetizing fields associated with a non-spherical ferromagnetic sample's shape alter ω_{res} as follows:

$$\omega_{\text{res}} = \gamma_0 \sqrt{[H_{\text{eff}} + (N_x - N_z)M_s] \times [H_{\text{eff}} + (N_y - N_z)M_s]}, \quad (34)$$

where N_x , N_y , and N_z are the demagnetizing shape factors [13–15]. Here, we discuss exclusively ferromagnetic samples that are *uniformly* magnetized as, only for them, the demagnetizing factors have a rigorous meaning. Thus, the resonant precession frequency essentially depends on the ferromagnet's shape and saturation magnetization M_s . For a thin ferromagnetic layer, $N_x = N_z = 0$ and $N_y = 1$, thus resulting in [13–15]:

$$\omega_{\text{res}} = \gamma_0 \sqrt{H_{\text{eff}} (H_{\text{eff}} + M_s)}. \quad (35)$$

The anisotropy energy also affects the ferromagnetic resonant condition. In a single crystal, the required resonant field strength depends on the direction of the crystal axis relative to the sample's shape axis. In a polycrystalline sample, the ferromagnetic resonance is broader than in a single crystal due to the distribution of the resonant field strengths [14].

Considering the effect of the anisotropy energy in terms of an equivalent magnetic field, the corresponding torque onto the ferromagnet is equal to:

$$\frac{\partial \varepsilon_{\text{an}}}{\partial \theta} = \mathbf{M} \times \mathbf{H}_{\text{an}}. \quad (36)$$

\mathbf{H}_{an} can be expressed in terms of an effective demagnetizing field [14]:

$$\begin{aligned} H_x^{\text{an}} &= -N_x^{\text{an}} M_x, \\ H_y^{\text{an}} &= -N_y^{\text{an}} M_y. \end{aligned} \quad (37)$$

The new ferromagnetic resonant condition must account for these equivalent demagnetizing factors [14]:

$$\omega_{\text{res}} = \gamma_0 \left\{ [H_{\text{eff}} + (N_x + N_x^{\text{an}} - N_z)M_s] \times [H_{\text{eff}} + (N_y + N_y^{\text{an}} - N_z)M_s] \right\}^{1/2}. \quad (38)$$

The ferromagnetic resonance has a certain linewidth, which is understood as ΔH on the field scale at a fixed frequency or $\Delta \omega$ on the frequency scale at a fixed magnetic field (Fig. 1) [15, 16]:

$$\Delta \omega = \left(\frac{d\omega}{dH} \right) \Delta H. \quad (39)$$

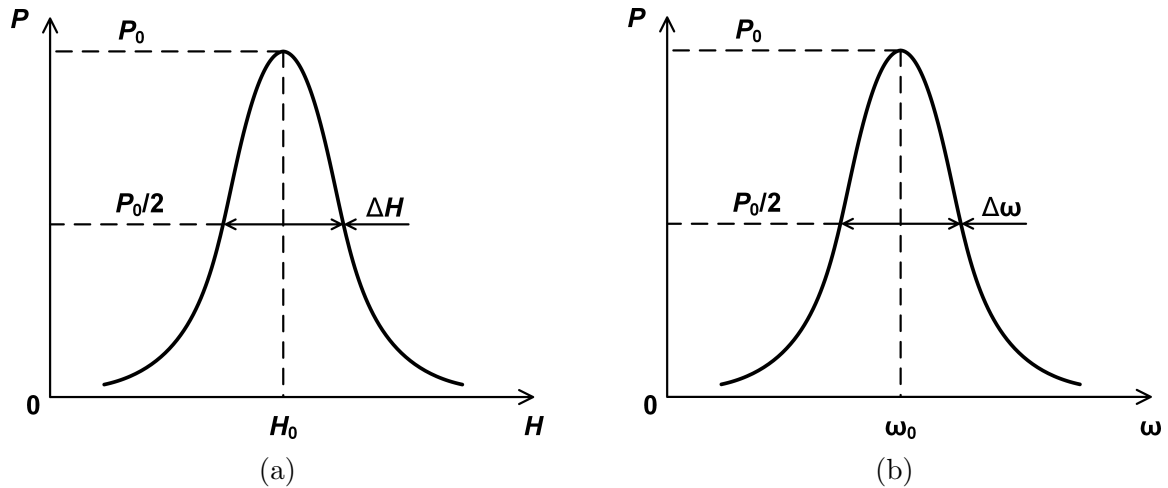


Fig. 1. Ferromagnetic resonance characterized *via* the magnetic power absorption P as a function of the (a) applied magnetic field or (b) frequency

The relationship between the ferromagnetic resonant linewidth and damping can be approximated as follows [17]:

$$\Delta\omega = \alpha\omega_{\text{res}}. \quad (40)$$

Besides the power absorption curve, the ferromagnetic resonance can be characterized *via* the susceptibility tensor that relates the radio frequency (RF) magnetization and the RF magnetic field (Fig. 2) [16]. For a ferromagnetic sample magnetized along the z -axis,

$$\begin{pmatrix} m_x \\ m_y \end{pmatrix} = \begin{pmatrix} \chi_{xx} & \chi_{xy} \\ \chi_{yx} & \chi_{yy} \end{pmatrix} \begin{pmatrix} h_x \\ h_y \end{pmatrix}. \quad (41)$$

In Eq. (41), the components of the susceptibility tensor can be calculated from the parameters of the ferromagnetic resonance condition [16].

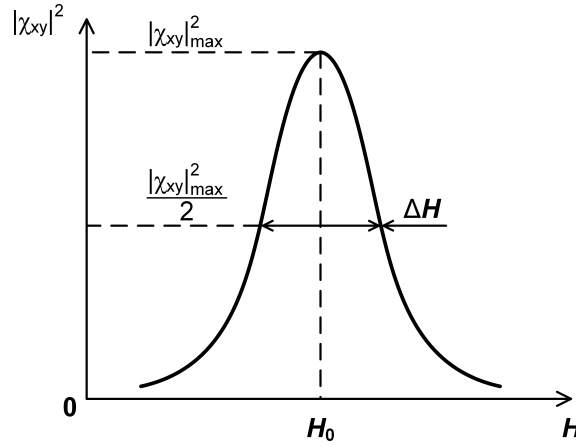


Fig. 2. Ferromagnetic resonance characterized *via* $|\chi_{xy}|^2$

The criterion for determining the linewidth is

$$|\chi_{xy}|_{\Delta H} = \frac{|\chi_{xy}|_{\text{max}}}{\sqrt{2}}. \quad (42)$$

In case of large-amplitude magnetization oscillations resulting from spin injection or large-field excitation, the ferromagnetic resonance frequency ω_{res} exhibits an additional frequency shift. This shift may be associated with the nonlinear frequency dependence on the amplitude of the driving force (*via* the effective field \mathbf{H}_{eff}). In practice, the damping constant α may also depend on the amplitude of the driving force [18] in a nonlinear fashion.

The two ST terms [recall Eq. (31)] also qualitatively affect the ferromagnetic resonance frequency and linewidth: the damping-like term affects the resonances' linewidth and amplitude while the field-like term shifts the resonance frequency [12].

The demagnetizing field is homogeneous only in special cases, such as for an ellipsoid, sphere, infinite circular cylinder, *etc.* In a ferromagnetic sample of an arbitrary shape, the inhomogeneous demagnetizing field produces non-homogeneous magnetization oscillations. The non-homogeneous magnetization oscillations, in turn, lead to non-homogeneous resonant conditions throughout the sample [15].

1.2 Ferromagnetic resonance characterization

The characterization of magnetization dynamics helps quantify numerous magnetic properties, such as saturation magnetization, anisotropy, damping, *etc.* The magnetization dynamics can be induced by various excitation mechanisms: magnetic, thermal, optical, ST, *etc.* This naturally led to the development of various experimental techniques that capture the resultant magnetization dynamics in either time or frequency domain.

One of the most common techniques is the time-resolved magneto-optical Kerr (TR-MOKE) microscopy. It achieves a few tens of fs in time and sub- μm spatial resolution. To date, it is considered the most efficient technique to probe ultrafast magnetization dynamics. Together with a scanning microscope, time-resolved scanning Kerr microscopy (TR-SKM) can image the time evolution of the magnetization's spatial distribution. In the magneto-optical Kerr (MOKE) experiment, the magneto-optical interaction between the linearly polarized light and the magnetic sample under test introduces an additional component k , such that the linearly polarized light incident on the surface becomes elliptically polarized. This component provides the measure of the sample's *local* magnetization defined at the position of the laser spot [19].

Brillouin light scattering (BLS) is a traditionally frequency-domain optical technique for space-, time-, or phase-resolved characterization of magnetization dynamics. It is based on the interaction between an incoming photon (a laser source) and spin waves in a magnetic sample under test. During scattering, the total energy of the system is conserved while the scattered photon may experience either a decrease or increase in its energy by respectively emitting or absorbing a spin wave [19].

In traditional ferromagnetic resonance (FMR) spectroscopy, a resonant absorption by magnetic dipoles takes place in the ferromagnetic sample under test when a microwave field is applied perpendicular to the static magnetic field. The FMR phenomenon occurs when the frequency of the microwave field matches the natural resonance frequency in the magnetic sample. At this resonance frequency, the microwave signal is strongly absorbed [19].

Both BLS and MOKE offer some advantages over FMR. First, the MOKE technique is

highly localized, which eliminates problems caused by variations and non-homogeneities over large areas. As MOKE's spacial resolution is limited only by the laser spot, it can provide localized measurements, *e.g.*, of local damping. BLS offers remarkable sensitivity down to a monolayer of magnetic material thickness. Both techniques, however, require expensive equipment and complicated optical alignment procedures [19].

In bulk ferromagnetic samples, the FMR can be measured using a microwave cavity-based technology at a fixed frequency defined by the cavity's resonant frequency. The sample is placed in a resonant cavity and supplied with microwave and static magnetic fields. The static magnetic field is swept within a few Tesla using electromagnets. The energy reflected from or transmitted through the cavity indicates the resonant absorption of the microwave energy by the ferromagnetic sample under test. Because of the microwave cavities' narrow bandwidth, cavity-based FMR measurements are typically performed at a fixed microwave frequency [16, 19].

The non-cavity-based approaches can implement both a frequency sweep at a fixed magnetic field and magnetic field sweep at a fixed microwave frequency. As was shown in the experimental work of Kalarickal *et al.*, the frequency and field sweeps yield the same linewidth [20].

One of the non-cavity-based techniques, namely the waveguide-based frequency-variation approach utilizing the shift in the FMR, operates as follows. First, the ferromagnetic sample is placed inside a shorted waveguide located between the two poles of an electromagnet. The electromagnet is driven by DC and AC current so that the sample is excited by a combination of the microwave and static magnetic fields. Then, the change in the operating frequency from ω_1 to ω_2 produces a subsequent shift ΔH in the power absorption curves [16].

Other non-cavity-based techniques, *e.g.*, the ones based on magnetostatic resonators or slot-coplanar junctions, can achieve an even wider operating bandwidth. In the magnetostatic resonator method, the ferromagnetic sample under test is placed on top of a piece of microstrip transmission line. The whole structure represents a magnetostatic wave magnetostatic wave straight-edge resonator (MSW-SER). The spacer between the sample and the microstrip line's central conductor controls the coupling strength. The bias magnetic field can tune the MSW-SER's resonant frequency thus enabling the measurement over a wide frequency range [16].

In magnetic trilayers, the giant or tunneling magnetoresistance effect translates the magnetization dynamics into resistance oscillations, thus allowing the characterization of magnetization dynamics using standard electrical measurement apparatus.

High-frequency magnetization dynamics can be excited in a *non-frequency-selective* man-

ner using a DC power supply. Then, the resultant AC oscillations can be directly observed with an oscilloscope (in time domain) or a spectrum analyzer (in frequency domain) labeled as “Measurement Instrument” in Fig. 3 [21–23].

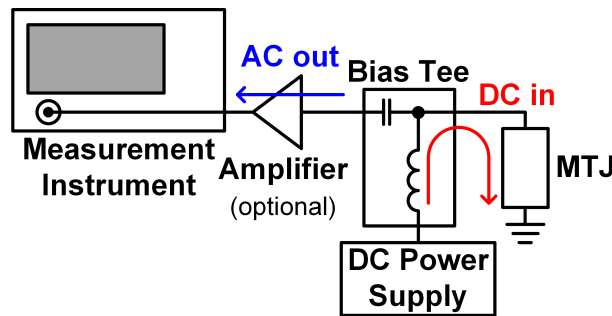


Fig. 3. Direct observation of high-frequency magnetization dynamics under the DC bias

Pros and cons of both the spectrum analyzer and oscilloscope readouts can be summarized as follows:

- To simply determine the FMR frequency and linewidth, the spectrum analyzer and oscilloscope can be used interchangeably.
- To isolate the signal instabilities, it is beneficial to perform the real-time oscilloscope measurements. The real-time oscilloscope suits this application better than the sampling one because it captures a large number of data points in one continuous record, which is ideal for characterization of non-stationary signals in an uncontrolled environment. As for the sampling oscilloscope, it constructs the full waveform over successive acquisitions, thus being suitable for characterization of repeatable signals in a controlled environment [24].
- Certain applications might require retaining the signal’s phase information, which is accessible with an oscilloscope, but not with a spectrum analyzer.
- Using an adequate resolution bandwidth (RBW), spectrum analysis can easily distinguish between two spectral peaks in the frequency domain. As for the oscilloscope measurements, they would require signal processing considerations regarding windowing: narrow window response provides better frequency resolution while the wider window response produces more accurate amplitude measurements [25].
- Both measurement instruments are unsuitable at a high DC bias because it likely leads to the tunnel barrier breakdown.

A combination of AC and DC signals excites magnetization dynamics in a *frequency-selective* manner (*i.e.*, non-simultaneous excitation of selected FMR modes). Similar to the description above, the resultant system response can be recorded in either frequency or time domain.

The frequency-domain measurement typically utilizes a vector network analyzer (VNA-FMR) and thus relies on coupling between the VNA's incident wave and the signal resulting from the magnetization dynamics [26]. The unstable phase relation between magnetization precession and the VNA's incident wave can make this measurement technique inefficient for characterization of magnetization dynamics in multilayers. This problem may be approached at the design stage by engineering the samples under test so that the initial (equilibrium) angle between the multilayer's adjacent magnetic moments is well-controlled [23]. Alternatively, the VNA's intermediate frequency bandwidth (IFBW) can be sufficiently lowered (see Fig. 22) to reduce point-to-point variations (point-to-point as opposed to trace-by-trace averaging⁽¹⁾). This technique may also suffer from heating effects at a high DC bias.

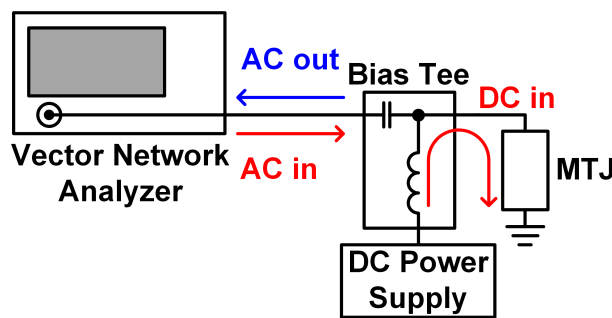


Fig. 4. VNA-FMR relying on coupling between the VNA's incident wave and the signal resulting from the magnetization dynamics

In the time domain, the magnetization dynamics can be excited by the AC and DC mixing pulse while the resultant resistance oscillation is detected with an oscilloscope [28]. This measurement technique reduces the influence of heating effects because it utilizes short DC bias pulses. The main disadvantage of this measurement scheme, however, is the low dynamic range limited by the magnetizations' relaxation time. In this context, the term "dynamic range" refers to the usable power range for signals of interest limited by the system noise floor and maximum tolerable signal levels used for the excitation of magnetization oscillations.

Magnetization dynamics are inherently nonlinear. To experimentally observe these nonlinear dynamics, however, it is often necessary to excite the system with high magnetic fields or AC powers. In special cases, it is possible to drive the magnetic system into a (quasi-)chaotic regime where small changes in the initial magnetization conditions lead to vastly different dynamics [29].

A measured quantity that can be used to characterize nonlinear magnetization dynamics

⁽¹⁾The IFBW is a variable filter used to reduce noise. Narrower IFBW results in additional data samples at each frequency point. Thus, the IFBW reduction insures point-to-point averaging. In sweep-to-sweep averaging, in turn, each data point is computed based on an exponential average of consecutive sweeps weighted by a user-specified averaging factor [27].

is the magnetic system's DC response. Magnetic trilayers' DC response has a measurable contribution around the resonant precession frequency of the free layer due to the ST rectification phenomenon. The physics behind this effect can be thought of as follows. The AC signal applied to a trilayer generates a torque onto the free layer spin moment. When the frequency of the AC excitation signal is close to the resonant precession frequency of the free layer spin moment, the free layer spin is tilted towards either more parallel or more anti-parallel orientation with respect to the pinned layer magnetization during each half-cycle of the input AC signal. The difference between these two states produces a measurable DC response [30].

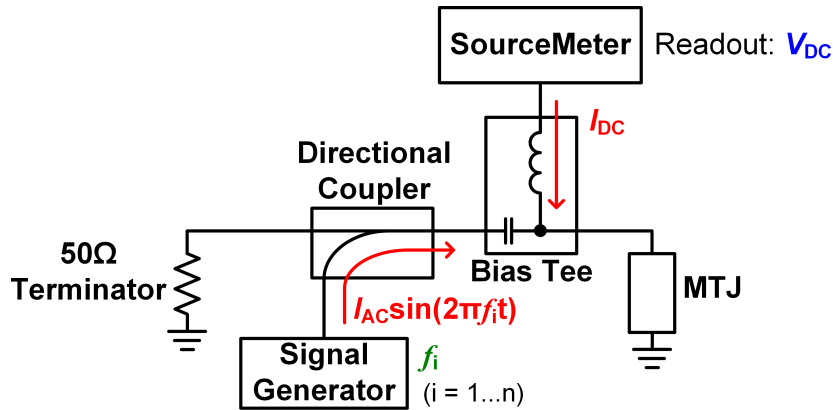


Fig. 5. DC readout FMR measurement relying on the ST rectification phenomenon

The DC response can be obtained if the sample under test is excited with a combination of the DC bias current and AC signal while the DC voltage across the sample is measured with a voltmeter [30]. Alternatively, the DC response can be extracted by driving the sample with a modulated AC signal and measuring the output signal using a lock-in amplifier [31]. If the signal detected by the amplifier is in-phase with the reference signal, the detected signal is rectified by the lock-in process. Otherwise, it is perfectly suppressed. This maximizes the signal-to-noise ratio of the measurement.

Since nonlinear effects are involved, it is highly desired to obtain the response not only at the DC or excitation frequency (as in the VNA-FMR) but also at harmonic components. This can be accomplished with an NVNA (in frequency domain) and/or full-scale micro-magnetic modeling (in time domain). These techniques are discussed in greater detail in the subsequent chapters.

1.3 Numerical modeling of magnetization dynamics

The theory of one macrospin assumes that the magnetization vector has the same magnitude and direction throughout the ferromagnetic sample [29, 32, 33]. This approximation allows the characterization and study of magnetization dynamics, including nonlinear and

chaotic behavior, as the more complicated physics of films and nanostructures would require a numerical treatment due to the magnetization non-homogeneities throughout the material.

The simplest macrospin approach based on the Stoner-Wohlfarth concept describes the physics of tiny magnetic single-domain particles. Because of such treatment, there are no domain walls and one must consider only the coherent domain rotation [32, 33]. At $T = 0$ K, a single-moment particle must have an elliptical shape [33]. The particle has a uniaxial anisotropy and is subject to an external magnetic field applied at an angle ϕ . If the magnetization of the particle is at an angle θ to the direction of the external field, the system energy is equal to

$$E = E_{\text{an}} + E_{\text{ext}} = K_1^{\text{un}} \sin^2 \theta V_0 - \mu_0 M_s H_{\text{ext}} \cos(\theta - \phi) V_0, \quad (43)$$

where V_0 is the particle volume.

A ferromagnetic sample of a finite size has a magnetostatic energy contribution given by $\mu_0 N_{ij} \mathbf{M}_i \mathbf{M}_j / 2$, where the demagnetization coefficients N_{ij} are determined by the sample's shape. The magnetization \mathbf{M} is represented by its individual moments. If we combine the anisotropy and demagnetizing energies, we obtain

$$K_1^{\text{un}} \sin^2 \theta V_0 + \frac{1}{2} \mu_0 (N_{\perp} M_x^2 + N_{\perp} M_y^2 + N_{\parallel} M_z^2) V_0, \quad (44)$$

which yields [6]

$$\left[K_1^{\text{un}} + \frac{1}{2} \mu_0 M_s^2 (N_{\perp} - N_{\parallel}) \right] \sin^2 \theta V_0 + \text{const.} \quad (45)$$

Here, \parallel and \perp denote the demagnetization coefficients parallel and perpendicular to the z -axis.

Thus, the effective anisotropy can be defined as

$$K_{\text{eff}} = \left[K_1^{\text{un}} + \frac{1}{2} \mu_0 M_s^2 (N_{\perp} - N_{\parallel}) \right]. \quad (46)$$

The total energy of the Stoner-Wohlfarth model can be re-written as

$$E = K_{\text{eff}} \sin^2 \theta V_0 - \mu_0 M_s H_{\text{ext}} \cos(\theta - \phi) V_0. \quad (47)$$

At equilibrium, the magnetization points in the direction θ^* corresponding to the energy minimum. Analytic solutions are possible for $\phi = 0, \pi/4, \pi/2$ while the rest can be numerically computed. For each ϕ of interest, one can visualize the trajectory of the magnetization direction that lowers the energy and the corresponding hysteresis loops. Even a system with no irreversible effects associated with domain-wall pinning like the Stoner-Wohlfarth model can lead to a hysteresis simply due to the presence of anisotropies [32,33].

One of the limitations of the Stoner-Wohlfarth model is the critical characteristic size above which a single domain is no longer expected. To determine the critical particle size, one may use the following condition: the demagnetization energy becomes equivalent to the exchange energy, such that

$$\begin{aligned} \frac{1}{2}\mu_0 N_{ij} \mathbf{M}_i \mathbf{M}_j &\sim \frac{1}{2}\mu_0 M_s^2 N_c, \\ \frac{A_{ij}}{M_s^2} \frac{\partial M_k}{\partial x_i} \frac{\partial M_k}{\partial x_j} &\sim \frac{A}{R_c^2}, \end{aligned} \quad (48)$$

where N_c is the demagnetization coefficient along the preferred axis, typically the length of an elliptically-shaped particle. $i, j, k = 1, 2, 3$ while A_{ij} is the exchange constant along i, j directions.

Assuming that $A_{ij} \sim A$ regardless of i, j , the condition above results in the following critical radius:

$$R_c \sim \sqrt{\frac{2A}{\mu_0 M_s^2 N_c}}. \quad (49)$$

Under this condition, the exchange energy (arising from inhomogeneities due to spatial variation of \mathbf{M}) is no longer the largest contribution to the total energy [33].

Let's review how the special case of a macrospin approximation can be applied to the characterization of the nonlinear and chaotic magnetization dynamics. Considering an elliptical or rectangular sample with arbitrary demagnetizing factors N_x, N_y , and N_z , we treat the magnetization \mathbf{M} as a macrospin. The magnetic energy density has contributions from the demagnetizing field, static external field H applied along the z -axis, and the RF field $h(t) = h \cos(\omega t)$ applied along the x -axis [29].

The total energy density of the sample is

$$\varepsilon = \frac{1}{2}\mu_0 (N_x M_x^2 + N_y M_y^2 + N_z M_z^2) - \mu_0 M_z H - \mu_0 M_x h \cos(\omega t). \quad (50)$$

The demagnetizing factors add up to 1: $N_x + N_y + N_z = 1$ [34]. In case of a rectangular sample, the demagnetizing field actually varies within the sample, whereas in the elliptical case, the demagnetizing field is uniform throughout. If the rectangular sample is sufficiently small, the demagnetizing factors can be evaluated either in the center of the sample or by averaging the field over the sample volume [29].

In the absence of damping, the magnetization dynamics is given by

$$\frac{d\mathbf{M}}{dt} = -\gamma_0 \mathbf{M} \times \left(-\frac{1}{\mu_0} \frac{\delta \varepsilon}{\delta \mathbf{M}} \right). \quad (51)$$

Substituting Eq. (50) into (51) results in the following differential equations of the three magnetization components:

$$\begin{aligned} \frac{dM_x}{dt} &= -\gamma_0 M_y [H + (N_y - N_z) M_z], \\ \frac{dM_y}{dt} &= \gamma_0 [H + (N_x - N_z) M_z] - \gamma_0 h M_z \cos(\omega t), \\ \frac{dM_z}{dt} &= -\gamma_0 (N_x - N_y) M_x M_y + \gamma_0 h M_y \cos(\omega t). \end{aligned} \quad (52)$$

These differential equations contain nonlinear terms involving products of the magnetization components as well as of the RF field h with the magnetization components. For small deviations of the magnetization from its equilibrium direction (*i.e.*, assuming that $M_x \ll M_z$, $M_y \ll M_z$, and $M_z \sim M_s$), these equations can be linearized.

When this assumption is no longer valid, M_x and M_y magnetization components become comparable with M_z . This dynamic regime is characterized by large-angle magnetization precession where the quadratic nonlinear terms in the damped equation of motion become dominant. Above a certain threshold, the magnetization trajectory may become chaotic, producing different trajectories because of small variations in the initial conditions.

The macrospin model can indeed be used to describe certain nonlinear magnetization dynamics in nanoelements. It can even foresee the route to chaos *via* bifurcations. But the macrospin model eventually breaks down, *e.g.*, for larger nanoelements whose magnetization dynamics must be treated micromagnetically to properly capture their transition to chaos [29].

Depending on the problem complexity, numerical treatment of magnetization processes by means of the finite-difference (FD), finite element (FE), or other methods might allow better understanding of the underlying physics. Compared to analytical methods, nu-

merical ones use fewer restrictions and simplifications when it comes to complex systems, thus offering more accurate solutions [35].

The FD method approximates the differential equations' *solutions* using the finite difference equations to approximate the derivatives. First, it implies a discretization of the computational region with a rectangular grid. Then, each derivative is approximated by a certain discretization scheme [35].

In the FE method, the goal is to approximate the partial differential (or integral) *equations*. This can be done by approximating the partial differential equation with a system of ordinary differential equations [35].

The FD and FE methods' considerations can be summarized as follows [2, 35, 36]:

- The FD method approximates the differential equation while the FE method approximates the solution.
- The FE mesh (discretization/approximation of the computational region) is able to handle complex geometries while the FD method is limited to flat surfaces.
- The FD method can be easily implemented in a straightforward fashion while the FE method requires re-writing the original problem in its weak (or variational) form.
- The FD method allows the efficient evaluation of the demagnetizing energy [*e.g.*, using the Fast Fourier transform (FFT) methods] and accessibility of higher-order methods. As for the FE method, its dense matrices can be approximated by the product of two lower-rank matrices [hierarchical (\mathcal{H} -) matrices method]. This allows for more efficient assembly, storage, and matrix-vector multiplication.

All numerical results presented here were obtained using the FD micromagnetic package **MicroMagus**. Let's review the numerical solution of the LLG equation based on the FD method in more detail. First, the sample is discretized into cuboids using a uniform rectangular mesh ($\Delta_x \times \Delta_y \times \Delta_z$), and the magnetization is sampled at points $(x_0 + i\Delta_x, y_0 + j\Delta_y, z_0 + k\Delta_z)$ [2]. The maximum mesh size is defined by the so-called "micromagnetic lengths": exchange length $l_{\text{exch}} = \sqrt{A/K}$ and demagnetizing length $l_{\text{demag}} = \sqrt{2A/\mu_0 M_s^2}$ [2, 37]. The exchange length is proportional to the domain wall width. It gives an estimation of the characteristic length within which exchange interactions are dominant. Therefore, it is expected that on a scale on the order of l_{exch} the magnetization is spatially uniform [2]. The demagnetizing length l_{demag} is the width of an isolated Bloch wall and is relevant for soft magnetic materials whose $l_{\text{demag}} \ll l_{\text{exch}}$ [37].

MicroMagus utilizes an energy-based approach, meaning that the magnetic energy is given primacy and is computed directly from the discretized magnetization, whereas the

effective field is derived from the resultant energy. The energy, being an integral quantity, has less variation than the field and is therefore easily approximated. This makes the energy-based approach more advantageous than the field-based one where the numerical solution to the LLG equation is found on the basis of a direct evaluation of the effective field components [2].

As stated above in Eq. (5), the Zeeman energy in its continuous form is equal to

$$E_{\text{ext}} = -\mu_0 \int_V \mathbf{M} \cdot \mathbf{H}_{\text{ext}} d^3r. \quad (53)$$

Then, the FD approximation to the Zeeman energy is

$$E_{\text{ext}} \approx -\mu_0 \sum_i \mathbf{M}(\mathbf{r}_i) \cdot \mathbf{H}_{\text{ext}}(\mathbf{r}_i) \Delta V_i, \quad (54)$$

where i runs over all cells, \mathbf{r}_i is the center of the rectangular cell i , and ΔV_i is the volume of cell i [2].

Recalling Eqs. (9) and (10), the magnetocrystalline anisotropy energy models for uniaxial and cubic materials

$$\begin{aligned} E_{\text{an}}^{\text{un}} &= - \int_V K_1^{\text{un}} (\mathbf{m} \cdot \mathbf{u})^2 d^3r, \\ E_{\text{an}}^{\text{cub}} &= \int_V [K_1^{\text{cub}} (\alpha_1^2 \alpha_2^2 + \alpha_2^2 \alpha_3^2 + \alpha_3^2 \alpha_1^2) \\ &\quad + K_2^{\text{cub}} (\alpha_1^2 \alpha_2^2 \alpha_3^2)] d^3r \end{aligned} \quad (55)$$

can be approximated as follows:

$$\begin{aligned} E_{\text{an}}^{\text{un}} &\approx - \sum_i K_1^{\text{un}}(\mathbf{r}_i) (\mathbf{m}(\mathbf{r}_i) \cdot \mathbf{u}(\mathbf{r}_i))^2 \Delta V_i, \\ E_{\text{an}}^{\text{cub}} &\approx \sum_i [K_1^{\text{cub}}(\mathbf{r}_i) (\alpha_1^2(\mathbf{r}_i) \alpha_2^2(\mathbf{r}_i) + \alpha_2^2(\mathbf{r}_i) \alpha_3^2(\mathbf{r}_i) + \alpha_1^2(\mathbf{r}_i) \alpha_3^2(\mathbf{r}_i)) \\ &\quad + K_2^{\text{cub}}(\mathbf{r}_i) (\alpha_1^2(\mathbf{r}_i) \alpha_2^2(\mathbf{r}_i) \alpha_3^2(\mathbf{r}_i))] \Delta V_i, \end{aligned} \quad (56)$$

where \mathbf{u} is the anisotropy axis; \mathbf{m} , \mathbf{u} , α [2].

By combining the constant $\mathbf{m}^2 = 1$ and the vector relation $|\nabla f|^2 = \nabla \cdot (f \nabla f) - f \nabla^2 f$, the exchange energy in Eq. (5) can be expressed in either of the following forms:

$$\begin{aligned}
E_{\text{exch}} &= \int_V [A(\nabla \mathbf{m})^2] d^3r \\
&= - \int_V \left[A \mathbf{m} \cdot \left(\frac{\partial^2 \mathbf{m}}{\partial x^2} + \frac{\partial^2 \mathbf{m}}{\partial y^2} + \frac{\partial^2 \mathbf{m}}{\partial z^2} \right) \right] d^3r.
\end{aligned} \tag{57}$$

The latter expression is somewhat easier to manipulate and is used to obtain a discrete approximation for the exchange energy.

First, the simplest numerical approximation for the derivative operator is

$$\frac{\partial^2 \mathbf{m}}{\partial x^2}(\mathbf{r}) = \frac{1}{\Delta_x^2} [\mathbf{m}(\mathbf{r} + \Delta_x \hat{x}) - 2\mathbf{m}(\mathbf{r}) + \mathbf{m}(\mathbf{r} - \Delta_x \hat{x})] + O(h^2). \tag{58}$$

The analogous expressions for $\partial^2 \mathbf{m} / \partial y^2$ and $\partial^2 \mathbf{m} / \partial z^2$ lead to a seven-point approximation for the exchange energy equation involving magnetization at the point \mathbf{r}_i and its six closest neighbors [2, 38]:

$$E_{\text{exch}} \approx - \sum_i \Delta V_i A \sum_j \mathbf{m}(\mathbf{r}_i) \cdot [\mathbf{m}(\mathbf{r}_i + \boldsymbol{\epsilon}_j) - \mathbf{m}(\mathbf{r}_i)] / |\boldsymbol{\epsilon}_j|^2, \tag{59}$$

where $\mathbf{r}_i + \boldsymbol{\epsilon}_j$, varying over j , specifies each of the six closest neighbors to \mathbf{r}_i in the discretized mesh.

In Eq. (59), $\mathbf{m}(\mathbf{r}_i) \cdot \mathbf{m}(\mathbf{r}_i)$ can be replaced with $\mathbf{m}^2 = 1$, thus making

$$E_{\text{exch}} \approx - \sum_i \Delta V_i A \sum_j [\mathbf{m}(\mathbf{r}_i) \cdot \mathbf{m}(\mathbf{r}_i + \boldsymbol{\epsilon}_j) - 1] / |\boldsymbol{\epsilon}_j|^2. \tag{60}$$

The magnetodipolar energy contribution in Eq. (5)

$$E_{\text{md}} = -\frac{\mu_0}{2} \int_V \mathbf{M} \cdot \mathbf{H}_{\text{md}} d^3r \tag{61}$$

can be expressed as

$$E_{\text{md}} \approx \frac{\mu_0}{2} \sum_{i,j} \Delta V_i \mathbf{M}^T(\mathbf{r}_i) N(\mathbf{r}_i, \mathbf{r}_j) \mathbf{M}(\mathbf{r}_j). \tag{62}$$

$N(\mathbf{r}_i, \mathbf{r}_j)$ is the 3×3 matrix evaluated analytically assuming that the magnetization inside each discretization cell is homogeneous [2].

The energy-based approach is obviously convenient if the goal is to find the equilibrium magnetization state *via* direct energy minimization. The choice of a minimization technique is determined by a particular micromagnetic problem depending on a type of magnetic material (soft *versus* hard), magnetization structure (localized *versus* extended), geometry (bulk *versus* thin film), *etc.* Most minimization methods, however, agree on the termination criterion based on the reduced torque. This means that the minimization stops when a torque acting on each magnetic moment becomes smaller than a given threshold: $|\mathbf{m}_i \times \mathbf{H}_i^{\text{eff}}| < \varepsilon$. The values of ε should be small enough (*e.g.*, 10^{-3} – 10^{-4}) so that no further changes in the equilibrium magnetization state are observed if smaller ε are used. As this criterion provides information about the discretization cell’s state, it is more sensitive than the alternative method whose termination criterion uses the information about the total energy change [39].

Almost all magnetic systems have many configurations (metastable states) driving the energy to minimum. Among them, there is a global minimum. Thus, there are algorithms that search for the 1) nearest (to the initial magnetization configuration) local energy minimum and 2) global energy minimum, which is the lowest energy minimum of the system under study. Methods that are designed to find the global energy minimum are quite slow and impractical for large-scale micromagnetic problems. For this reason, we focus on finding the local quasi-equilibrium, metastable system configuration [39].

A local minimum can be found using one of the following methods [39]:

1. Apply a standard numerical minimization method (*e.g.*, conjugate gradient).
2. Solve the LLG equation of motion for the system’s magnetization configuration.
3. Iterate until the magnetization is aligned parallel to the corresponding effective field (*i.e.*, equilibrium state).

Among standard numerical minimization methods, the conjugate gradient is the most suitable one when applied to micromagnetic problems. Due to the nonlinear constraint $m_x^2 + m_y^2 + m_z^2 = 1$, the standard conjugate gradient method (which is suitable only for independent variables) cannot be used. To circumvent this problem, it can be transformed into spherical coordinates where the magnetic moment’s components are independent. This, however, reveals a well-known numerical problem: if a magnetic moment is sufficiently close to the polar axis ($\theta \approx 0$ or $\theta \approx \pi$), its small movements can lead to arbitrary changes of ϕ . If moments do not remain sufficiently far from the polar axis, the minimization procedure requires automatic “restarts” of the method to keep the moments away from the polar axis, thus resulting in slow convergence [39]. Instead, one can use the modified conjugate gradient method introduced in [40]. In this work, the gradient direction is projected onto the plane perpendicular to the magnetic moment’s local direction, thus

ensuring the approximate conservation of the moment magnitude.

Alternatively, the equilibrium state can be found with the help of the relaxation methods using the LLG equation of motion applied to the system's magnetization configuration in the effective field. The LLG equation of motion for the i -th discretization cell can be written as:

$$\frac{d\mathbf{M}_i}{dt} = -\gamma\mathbf{M}_i \times \mathbf{H}_i^{\text{eff}} - \gamma\frac{\lambda}{M_s}\mathbf{M}_i \times (\mathbf{M}_i \times \mathbf{H}_i^{\text{eff}}). \quad (63)$$

The solution of Eq. (63) should converge to the equilibrium magnetization configuration (energy minimum) in the limit $t \rightarrow \infty$. This means that by solving Eq. (63) for a sufficiently long time, we can approach the equilibrium magnetization state. As we are not interested in simulating the magnetization dynamics, Eq. (63) can be further reduced by omitting the $\mathbf{M}_i \times \mathbf{H}_i^{\text{eff}}$ term responsible for the magnetization precession around the effective field:

$$\frac{d\mathbf{M}_i}{d\tau} = -\lambda\mathbf{M}_i \times (\mathbf{M}_i \times \mathbf{H}_i^{\text{eff}}\{\mathbf{M}\}), \quad (64)$$

where $\tau = t\gamma M_s$ is the reduced time. $\{\mathbf{M}\}$ indicates that the effective field depends on the *entire* magnetization configuration. Finally, one can solve the system of ordinary differential equations (ODEs) by choosing one of the existing methods. However, one must take into account the peculiarities of micromagnetic problems: 1) to assure the solution stability (*i.e.*, that the system energy decreases after each integration step), the integration steps must be small; 2) due to the competition between the strong, short-range exchange interactions and weak, long-range dipolar forces, the equation of motion is extremely “stiff,” thus making the use of implicit methods impractical. For these same reasons, the explicit Euler method with an adaptive step-size control proved to be successful [39].

The underlying principle of the “alignment” methods is that to reach the equilibrium state, it is sufficient to have all magnetic moments aligned parallel to the effective field so that no further rotation of magnetic moments may occur. This can be achieved iteratively by first aligning each moment along the corresponding effective field $\mathbf{H}_i^{\text{eff}}$. Second, we need to re-evaluate $\mathbf{H}_i^{\text{eff}}$ for the new magnetization state. Finally, the equilibrium configuration is found if the convergence criterion has been met. To make these methods applicable to micromagnetic problems, however, they must be modified, *e.g.*, by introducing the under-relaxation procedure [39].

The numerical study of magnetization dynamics, in turn, reduces to the integration of the

corresponding LLG equation of motion. The main challenge, however, occurs in simulating magnetization dynamics while taking into account thermal fluctuations (temperature $T > 0$ K). Recalling Eq. (28), thermal fluctuations can be accounted for by an additional contribution, \mathbf{H}_{th} , to the deterministic effective field \mathbf{H}_{eff} , thus leading to the stochastic LLG equation of motion. Equation (28) can be further simplified by omitting \mathbf{H}_{th} in the dissipation term:

$$\frac{d\mathbf{M}}{dt} = -\gamma\mathbf{M} \times (\mathbf{H}_{\text{eff}} + \mathbf{H}_{\text{th}}) - \gamma\frac{\lambda}{M_s}\mathbf{M} \times (\mathbf{M} \times \mathbf{H}_{\text{eff}}). \quad (65)$$

The corresponding thermal fluctuation field in the dissipation term must be accounted for by proper re-scaling the fluctuation power [7, 39].

The numerical treatment of Eq. (65) can by no means be performed the same way as with ODEs. To demonstrate this, let's review the simplest analogous problem—motion of small particles in a viscous medium:

$$\dot{x} = \frac{1}{\eta}F_{\text{det}}(t) + a(x, t)\xi_L(t), \quad (66)$$

where η is the friction coefficient, F_{det} is a deterministic force, and ξ_L is the random (or Langevin) force. $\xi_L(t)$ is usually assumed to be a random Gaussian variable with the following statistical properties:

$$\begin{aligned} \langle \xi(t) \rangle &= 0, \\ \langle \xi(0), \xi(t) \rangle &= 2D\delta(t), \end{aligned} \quad (67)$$

where the fluctuation power $D \sim T$. $a(x, t)$ shows that the noise characteristics can be both coordinate- and time-dependent [7, 39].

If we were to integrate Eq. (66) as an ODE,

$$W(t) = \int_0^t \xi(t') dt', \quad (68)$$

the result would represent a random process since the integrand is a random variable. $W(t)$ is the standard Wiener process (also known as Brownian motion) and is not differentiable: $[W(t+\Delta t) - W(t)]/\Delta t$ almost certainly diverges at the limit $\Delta t \rightarrow 0$. Because the derivative of $W(t)$ does not exist, this problem cannot be treated as an ODE.

Instead, we can re-write the product $\xi(t) dt$ as the differential of the Wiener process and define the corresponding integral

$$I = \int a(x, t) dW(t) \quad (69)$$

as the Riemann-Stieltjes integral of the approximating sum:

$$\begin{aligned} I &= \lim_{n \rightarrow \infty} \sum_{i=1}^n a(x(\tau_i), \tau_i) \Delta W(\Delta t_i) \\ &= \lim_{n \rightarrow \infty} \sum_{i=1}^n a(x(\tau_i), \tau_i) [W(t_i) - W(t_{i-1})], \end{aligned} \quad (70)$$

where τ_i is in the i -th sub-interval $[t_{i-1}, t_i]$ [7, 39].

Now, the problem is to define the limit and, specifically, choose the intermediate points τ_i . In Itô calculus, τ_i coincides with the leftmost point of the interval: $\tau_i = t_{i-1}$. The Stratonovich integral defines τ_i in the middle of the interval: $\tau_i = (t_{i-1} + t_i)/2$. The choice of the intermediate points τ_i becomes critical if the noise in the stochastic equation is multiplicative as the two standard choices (Itô *versus* Stratonovich) lead to different solutions.

In Eq. (65), the noise is multiplicative and is found in the cross product of the random thermal field and magnetic moments. Thus, it is only logical to suggest the Stratonovich interpretation to solve the stochastic LLG. Numerically, different integration schemes naturally converge to different stochastic integrals. If the magnetization magnitude is preserved, however, the two treatments of the stochastic equation are equivalent [7, 39].

Finally, it is worth mentioning the necessity of an adaptive step-size control. The basic idea is to reduce the step-size if the error exceeds the respective tolerance. It is required to achieve a fixed solution accuracy at a minimum computational cost [7, 39].

2 Read head system

This thesis presents a study of magnetization dynamics in MgO-based magnetic tunnel junctions (MTJs) that were designed to perform the read function in modern hard disk drives. This fact is emphasized so that the reader understands the challenges associated with the characterization and micromagnetic modeling of production samples coming from the presence of extrinsic device components (*i.e.*, magnetic shields, parallel resistor, sputtered and plated leads) and the insufficiency of the information about the samples. These challenges are discussed in more detail in the subsequent sections.

2.1 Magnetic read sensors⁽²⁾

The magnetic head is an essential part of modern hard disk drives and consists of the writer and reader. It is integrated into the head slider flying a few nanometers over the recording media (Fig. 6). The writer records the information on the media's recording layer when an alternating current is supplied to the write coil. In the small area adjacent to the recording layer, the main recording pole generates a high magnetic field (1.2–2 T) that produces magnetization transitions. A soft underlayer guides the write field flux through the recording layer back to the write head's return pole [42].

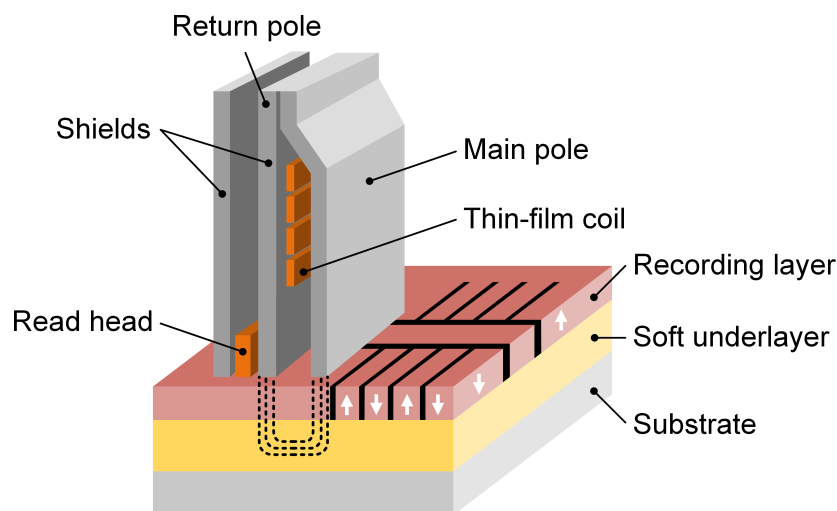


Fig. 6. Schematic of the perpendicular magnetic recording process

The reader, in turn, senses the magnetization transitions between the recorded “up” or “down” bits. Presently, reader paths consist of the tunnel magnetoresistance (TMR) sensor, electrically conductive shields, and the connecting leads that bridge the pads with the shields (Fig. 7). The shields should be sufficiently large to isolate the TMR sensor

⁽²⁾The results of this section are published in part in [41].

from the field from adjacent bits and large writer fields. The parallel resistor width and length are chosen so that it has a resistance ranging from 1.5 to 3 k Ω . The parallel resistor in this system is required to reduce TMR resistance variations. The shunt resistors are electrically connected to the leads made of sputtered material (*e.g.*, gold) and the ground pad. Typical values of the shunt resistors are from 20 to 25 k Ω . These resistors also provide electrostatic discharge (ESD) protection during wafer fabrication. Current TMR read heads have reader resistance ranging from 300 to 2000 Ω . TMR resistance varies linearly depending on magnetic flux from the media.

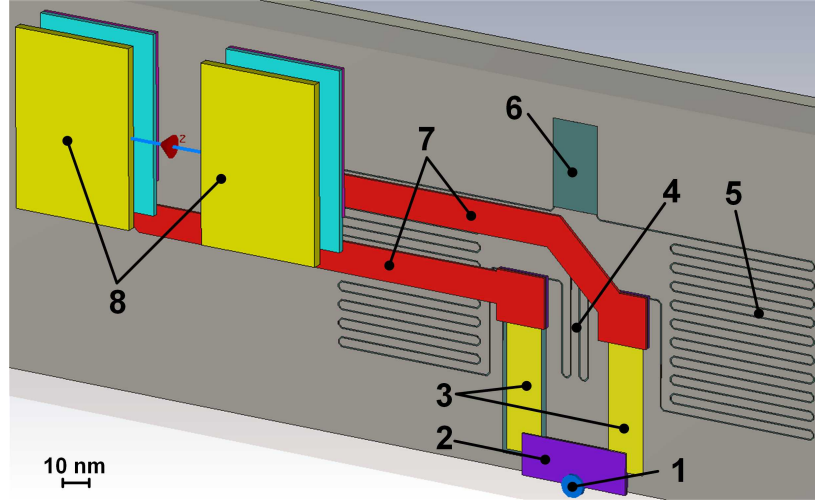


Fig. 7. Reader path: 1—TMR sensor, 2—magnetic shields, 3—sputtered leads, 4—parallel resistor, 5—shunt resistor, 6—ground pad, 7—plated leads, 8—pads

We characterized the read head system's radio frequency (RF) performance with a vector network analyzer (VNA). A VNA is intended to measure ratios of the incident and reflected traveling waves' (A_1 and B_1 , respectively) magnitude and phase at the excitation frequency. For a 1-port device, the relationship between A_1 and B_1 waves can be expressed as follows:

$$B_1(\omega) = S_{11}(\omega)A_1(\omega), \quad (71)$$

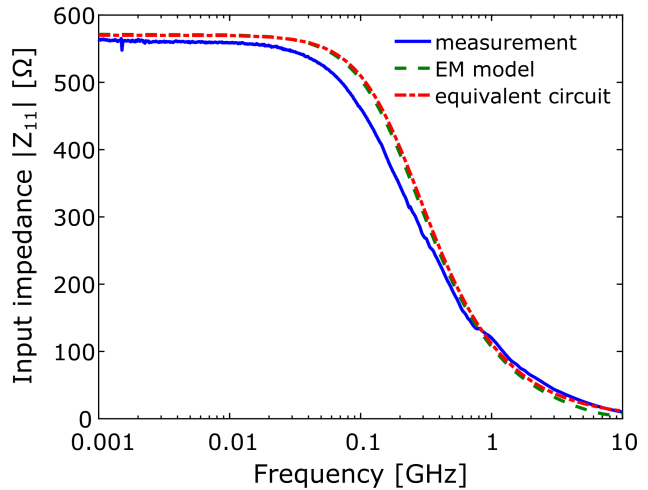
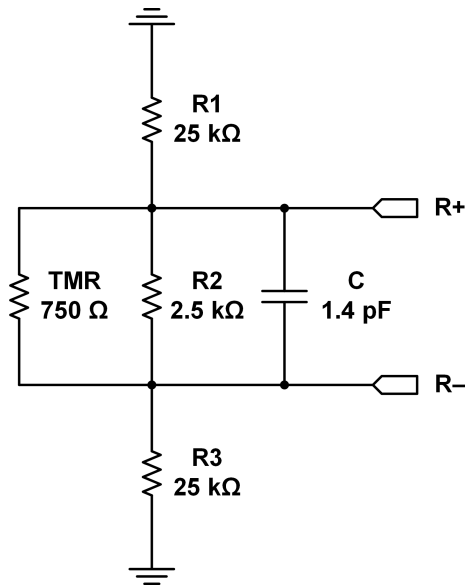
where $S_{11}(\omega)$ are the 1-port S-parameters, or scattering parameters. They properly describe the device's response to a small-signal stimulus, for which it can be approximated as *linear* around a fixed DC, or static, operating point.

The 50 Ω -referenced S_{11} and input impedance Z_{11} are related as follows:

$$Z_{11} = Z_0 \left(\frac{1 + S_{11}}{1 - S_{11}} \right), \quad (72)$$

where Z_0 is the 50- Ω system impedance [43].

We compared the electromagnetic (EM) and equivalent circuit (Fig. 8a) reader simulations with the VNA measurements. Figure 8b shows the bandwidth reduction due to the RC roll-off characteristic coming from the parallel resistor and shield-to-shield capacitance.



(a) Reader equivalent circuit [44]: $R2$ is the parallel resistor, $R1$ and $R3$ are the shunt resistors, and C is the shield capacitance. $R+$ and $R-$ are the probe pads. The schematic shows typical values.

(b) Measured input impedance seen between $R+$ and $R-$. The EM model is a CST FE model of the read head. The equivalent circuit is a Keysight ADS lumped element model as shown in (a).

Fig. 8. Measured and simulated RF performance of the read head system

While the EM and equivalent circuit reader models treat the TMR sensor as a simple 750- Ω resistor, its composition and principle of operation are much more complex than those of a simple resistor. A simplified stack of modern hard disk drives' single free layer (SFL) TMR sensors (Fig. 9a) consists of several layers comprising a single structure: free layer (FL), pinned layer (PL), and the antiferromagnetic (AFM) layer. The AFM layer fixes the PL's magnetization orientation *via* exchange coupling. The PL usually consists of two layers separated by a Ru layer coupling them antiferromagnetically. This reduces the stray field from the PL onto the FL. The Side Bias field sets the FL orthogonal to the PL, the most sensitive point. The stack's shape is tapered to ensure the PL's sufficient pinning. The PL is usually assumed to be perfectly pinned while the FL, separated from the PL by a thin MgO barrier, moves in response to the field from the magnetic media. Device resistance is proportional to the change in the relative orientation of the FL and PL [45].

One of the ways to decrease the read gap (distance between the top and bottom magnetic shields) is to make the AFM layer thinner. If the AFM IrMn layer is too thin, however, its grains become thermally unstable [46]. This renders the magnetization direction of the PL insufficiently pinned as well as increases the low-frequency ($1/f$) noise. In a dual

free layer (DFL) sensor (Fig. 9b), the two coupled FLs are biased with the compound Side Bias and hard Rear Bias. To keep the FLs in the orthogonal configuration, the Rear Bias pulls the FLs towards the in-plane hard axis and the Side Bias magnets bias them in opposite directions [47]. Thus, the DFL sensor provides an opportunity to eliminate the AFM layer, thus enabling a thinner gap and reducing the low-frequency noise [48, 49].

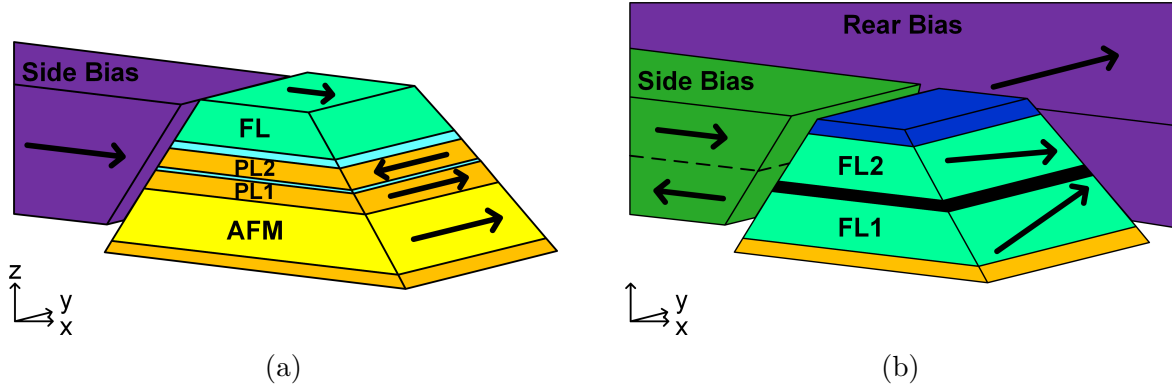


Fig. 9. Cut views of the (a) SFL and (b) DFL sensors. The right Side Bias and top/bottom shields are not shown. The top/bottom shields are located in $+/-z$ directions and designed, *e.g.*, to absorb the stray magnetic field from adjacent bits.

For the most part, this manuscript is devoted to the characterization and micromagnetic modeling of the SFL sensors' magnetization dynamics. Whenever possible, however, their performance is contrasted to that of the DFL sensors.

2.2 Ferromagnetic resonance frequencies⁽³⁾

Even though it is frequently assumed that the PL is fixed, it is actually pinned by a finite effective field. Room-temperature thermal fluctuations result in random magnetization dynamics of *both* the FL and PL, which can be quantified by their ferromagnetic resonance (FMR) modes [13]. Typical FMR frequencies of the FL and PL are in the range of several gigahertz (Fig. 10a).

In the DFL sensor, the in-phase and out-of-phase uniform oscillations of both the FL1 and FL2 produce the lower-frequency acoustic and optical modes (Fig. 10b). If the two FLs are identical, the acoustic mode can be completely suppressed.

To recover the non-uniform modes, it is important to take into account the composite structure of each FL and the corresponding coupling strengths (Fig. 11). There are two reasons for composite structure of each FL: layers on both sides of the barrier have higher saturation magnetization M_s to enhance the TMR, while the low M_s layers make

⁽³⁾The results of this section are published in part in [50].

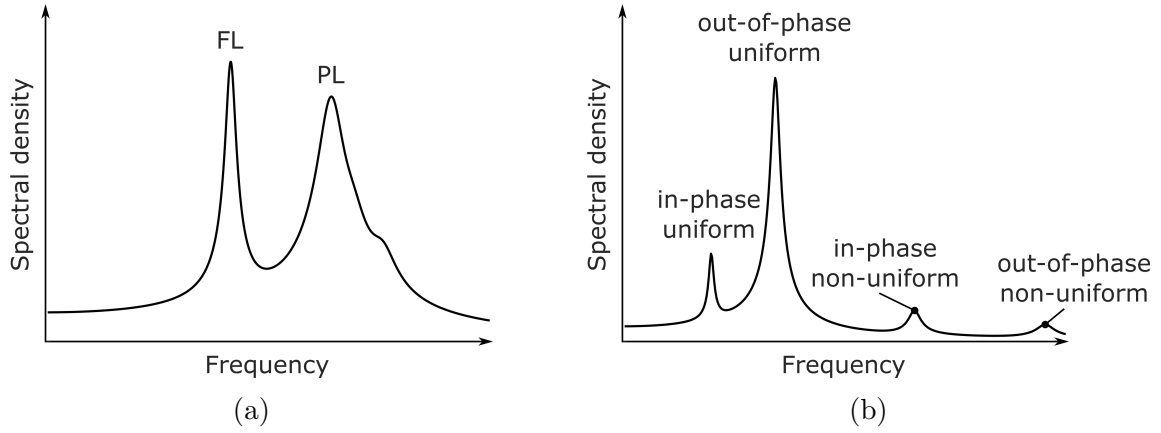


Fig. 10. Exemplary spectra produced by the (a) FL and PL magnetization fluctuations and (b) in-phase and out-of-phase movement of the two FLs

FLs softer [51, 52]. The high and low M_s layers can rotate both in-phase and out-of-phase at high frequencies (intralayer modes). The higher-frequency acoustic and optical non-uniform modes exhibit “buckling” motion. It is interesting to note that the optical “buckling” mode does not significantly contribute to the total spectral density as its phase cancels out in the stripe height (SH) direction (y -axis) [50].

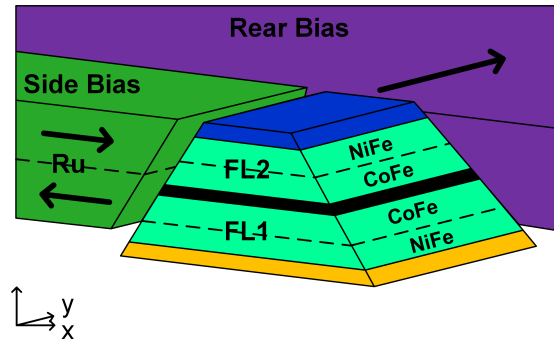


Fig. 11. Fig. 9b assumes monolithic FLs. In reality, each FL is a composite structure.

When under excitation, the spin-torque (ST) effect influences the thermal magnetization fluctuations and is taken into account by the two ST terms [recall Eq. (31)]. As mentioned in Section 1.1, contributions of both terms can be directly seen in the FMR spectrum: the damping-like term affects the resonance’s linewidth and amplitude while the field-like term shifts the resonant frequency [12].

The subsequent sections focus on FMR characterization and micromagnetic modeling of magnetization dynamics resulting from both thermal and ST contributions.

2.3 Tunnel magnetoresistance effect

The TMR effect is a change in the MTJ's electrical resistance with the relative orientation of the MTJ's magnetic layers usually set by an external magnetic field. The fundamental theory of tunneling through an MgO barrier can be found in [53].

The TMR effect can be described with a different level of complexity. The simplest models are based on the semiclassical approximation and often used for analysis of the tunneling I - V curves. These models, however, fail to describe the TMR itself as they do not account for changes associated with the magnetization configuration. Quantitative understanding of TMR, in turn, requires sophisticated calculations based on relativistic electronic band structure [54] and is beyond the scope of this work.

In this work, we use the qualitative description of the TMR's angular dependence between the two continuously varying magnetization vectors, \mathbf{m}_1 and \mathbf{m}_2 [55]:

$$R = \frac{1}{G} = \frac{R_{\perp}}{1 + \frac{\Delta_{\text{TMR}}}{2} \cos \theta}, \quad (73)$$

where R_{\perp} is the sensor resistance at the orthogonal magnetization state, Δ_{TMR} is the TMR ratio. The cosine of the angle θ is defined between the adjacent layers' magnetizations: $\cos \theta = \mathbf{m}_1 \cdot \mathbf{m}_2$.

Equation (73) is different from the generally used formulations describing a linear variation of the MTJ's resistance with $\cos \theta$, which appears to be valid only for small values of TMR [55].

2.4 Summary

In this chapter, we presented the various levels of complexity of the devices under investigation. On the system level, we described the read head function in the recording process. On the device level, we elaborated on the state-of-the-art reader path. Finally, we depicted the MgO-based MTJ embedded in the reader path. We characterized the devices' RF performance by their measured input impedance. Then, we presented the characterization of the MTJs' magnetization dynamics *via* ferromagnetic resonance.

3 Direct observation of high-frequency magnetization dynamics under DC bias

As discussed in Section 1.2, high-frequency magnetization dynamics translate into resistance oscillations due to the giant or tunnel magnetoresistance (GMR or TMR, respectively) effect and can be characterized using standard electrical measurement techniques.

In Fig. 3, the input AC signal may have two distinct regimes. If the DC-driven spin-torque (ST) effect is small, then the “Measurement Instrument” senses thermally-excited magnetization fluctuations (often referred to as “magnetic noise”). In this case, the resultant AC signal originates due to fluctuations of both the free and pinned layer (FL and PL, respectively) movements at angles large enough to produce measurable precession. Alternatively, if the DC-driven ST exceeds the damping torque, then ST can *coherently* excite stable steady-state magnetization precession at ferromagnetic resonance (FMR) frequencies [56].

In Section 1.2, we also discussed the advantages and disadvantages of analyzing the sought after electrical event as a function of time or frequency. In the frequency domain, we can use a spectrum analyzer to better determine the signal’s *harmonic content*. In the time domain, we can use an oscilloscope to view the signal’s time-dependent, *instantaneous value*. This chapter is devoted to specific examples of the spectrum and waveform analysis applied to signals originating from magnetization dynamics.

3.1 Spectrum analysis in frequency domain⁽⁴⁾

This section focuses on the spectrum-analyzer-based FMR characterization of magnetization dynamics in magnetic read heads. The power spectra presented below were obtained under various DC bias levels (current or voltage) and normalized with respect to the data obtained at zero DC bias. This normalization compensated for irregularities of the components used in the measurement setup and “ripples” arising from mismatched interfaces, thus isolating the performance of the device under test (DUT).

Figure 12 shows the power spectra of a $30 \times 35 \text{ nm}^2$ single free layer (SFL) tunnel junction read head at different values of the DC bias current. Its resistance-area product and TMR ratio are $0.4 \Omega\mu\text{m}^2$ and 90%, respectively. The spectrum-analyzer-based FMR measurement technique successfully revealed the expected FL and PL FMR modes (Fig. 10a) arising from high-frequency magnetization dynamics.

⁽⁴⁾The results of this section are published in part in [50] and presented at [57].

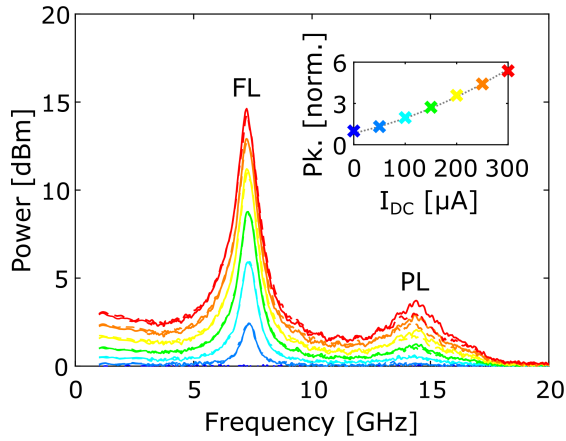


Fig. 12. Power spectra of an SFL tunnel junction read head obtained for different DC bias currents. The inset shows the quadratic growth of the FL peak amplitude with the DC bias current. Positive DC bias (solid line) corresponds to the electron flow from the PL to FL. Agilent E4446A spectrum analyzer's resolution bandwidth (RBW) was set to 51 kHz.

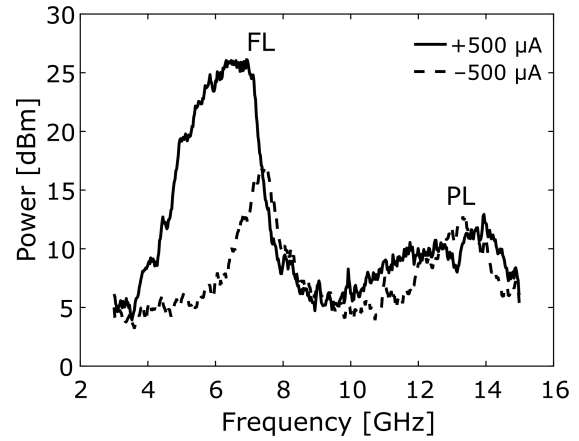


Fig. 13. Qualitatively different power spectra of an SFL tunnel junction read head obtained for opposite DC bias currents. At $+500 \mu\text{A}$, the FL peak transitions to the nonlinear regime *via* foldover. This sample is different from the one in Fig. 12, hence the difference in the FL and PL FMR frequencies. The spectrum analyzer's RBW was set to 100 kHz.

In the previous works, this measurement technique was used to quantify, *e.g.*, thermally-excited magnetic noise in tunnel junction read heads [22] as well as the ST-driven FMR excitation in Co/Cu/Co-layered nanostructures [21]. The latter manifests itself in the asymmetry of the FMR peaks with respect to the DC bias polarity because the effects of spin-polarized current are expected to be asymmetric with respect to the polarity of the DC bias. In [21], Kiselev *et al.* used the evolution of spectral lines to study the transition from the small-amplitude precession to the large-amplitude dynamic regime. At a threshold bias current, the FMR peaks started growing by two orders of magnitude along with an abrupt shift in FMR frequencies.

In Fig. 12, the power spectra acquired for opposite DC bias currents (solid and dashed lines) do not exhibit any qualitative difference, thus allowing us to attribute these FMR peaks to thermally-excited magnetization fluctuations of both the FL and PL. To state this quantitatively requires an analysis of the measurement uncertainty. Such analysis, however, is beyond the scope of this work. As in the published works, we also observe qualitative differences in the read heads' power spectra obtained at a higher DC bias current of the opposite polarities. At $+500 \mu\text{A}$ DC bias current, the FL peak exhibits an abrupt increase, broadening, red shift, and transition to the nonlinear regime *via* foldover (Fig. 13). Figure 12, in turn, shows the monotonic, quadratic growth of the FL peak amplitude with an increasing absolute value of the DC bias current.

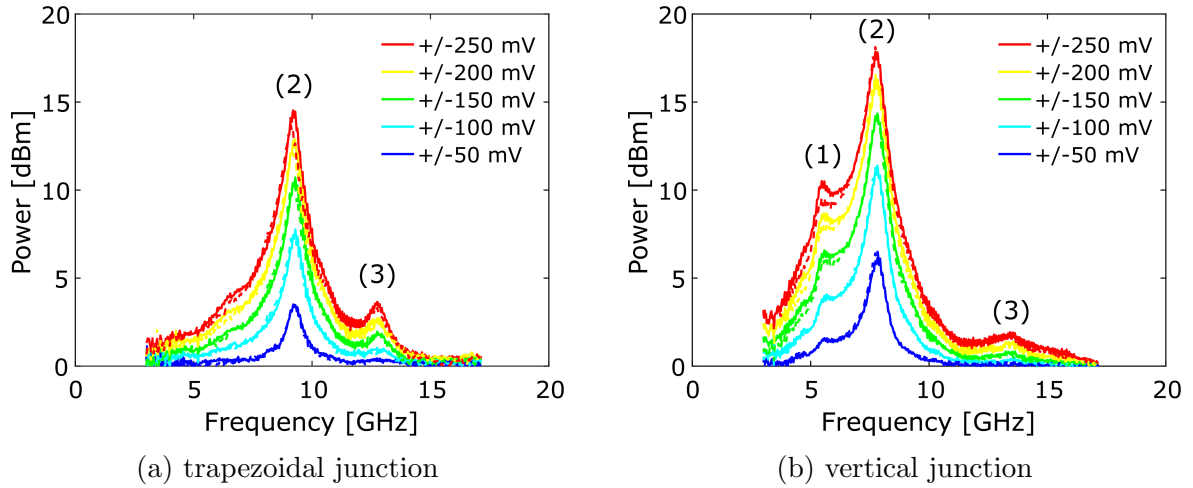


Fig. 14. DFL read heads' FMR modes: (1) in-phase, uniform a.k.a. “acoustic”; (2) out-of-phase, uniform a.k.a. “optical”; (3) in-phase, non-uniform. The spectrum analyzer's RBW was set to 100 kHz.

Concerning DFL sensors, their power spectra shown in Fig. 14 are counterintuitive to our initial supposition expressed in Section 2.2: if the two FLs are identical, the uniform acoustic mode [labeled as (1) in Fig. 14] can be completely suppressed. Specifically, Fig. 14 shows that compared to DFL sensors with a vertical junction, sensors with a trapezoidal junction typically (for a population of 22 characterized samples with both trapezoidal and vertical junctions) exhibit a suppressed uniform acoustic mode. A suppressed acoustic mode would translate into lower “tails” of this mode and, subsequently, lower magnetic

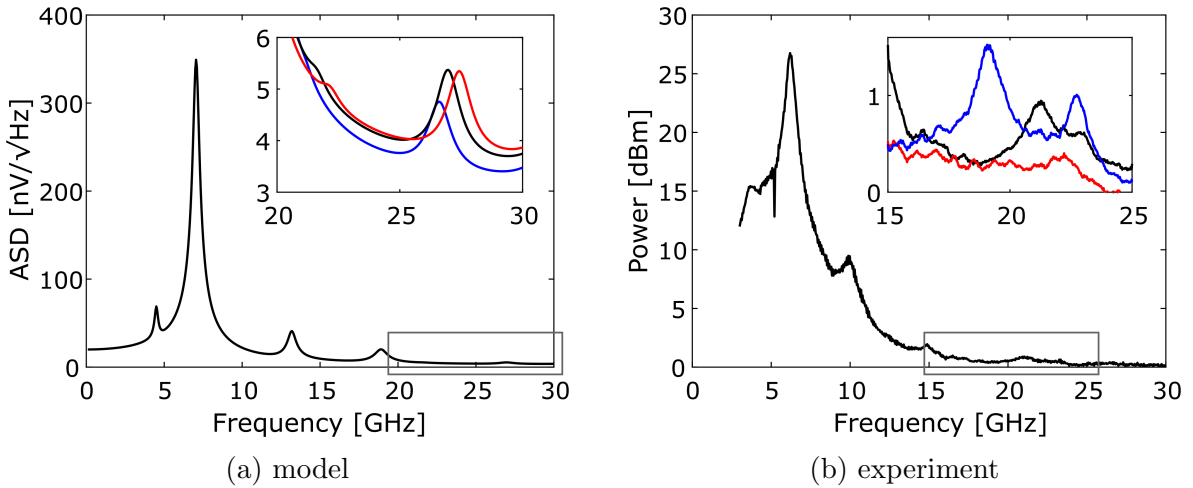


Fig. 15. Higher-order symmetry modes manipulated by a permanent magnet's field applied along the y -axis: $-$ +35 mT; $-$ 0 mT; $-$ -35 mT. (a) The simulated amplitude spectral density (ASD) acquired through a full 3-D micromagnetic simulation of the DFL's lossless excitation eigenmodes [58, 59]. (b) The power spectrum obtained under the DC bias voltage of +500 mV. To recover the higher-order symmetry modes, the spectrum analyzer's RBW was reduced to 10 kHz (inset) while the full spectrum is obtained at RBW of 30 kHz.

noise contribution within the reader bandwidth of up to 1 GHz. Thus, the spectrum analyzer readout in conjunction with the DC excitation can be effectively used to evaluate the noise performance of different read head designs.

In contrast with previous works [47, 48], we used the spectrum analyzer FMR characterization to reveal not only the the DFL’s higher-frequency acoustic and optical non-uniform modes but also the still-higher-frequency modes above the 15–20 GHz range (Fig. 15). Through an analysis of the stack’s amplitude spectral density (ASD), these were identified as being higher-order “buckling” modes having a non-uniform motion along both y - and x -axis (Fig. 16). These modes are shown to be sensitive to an applied field along the y -axis modifying the bias FLs equilibrium magnetization configuration. Due to the presence of magnetic shields and bias magnets (Figs. 7 and 9), production samples are least suited for FMR characterization with an applied magnetic field. The shields would distort the external field such that one is unable to control the relative orientation of the FLs to the degree required for such studies. Nevertheless, Figs. 15a and 15b seem to qualitatively agree, thus allowing us to make a statement about the origin of these still-higher-frequency modes.

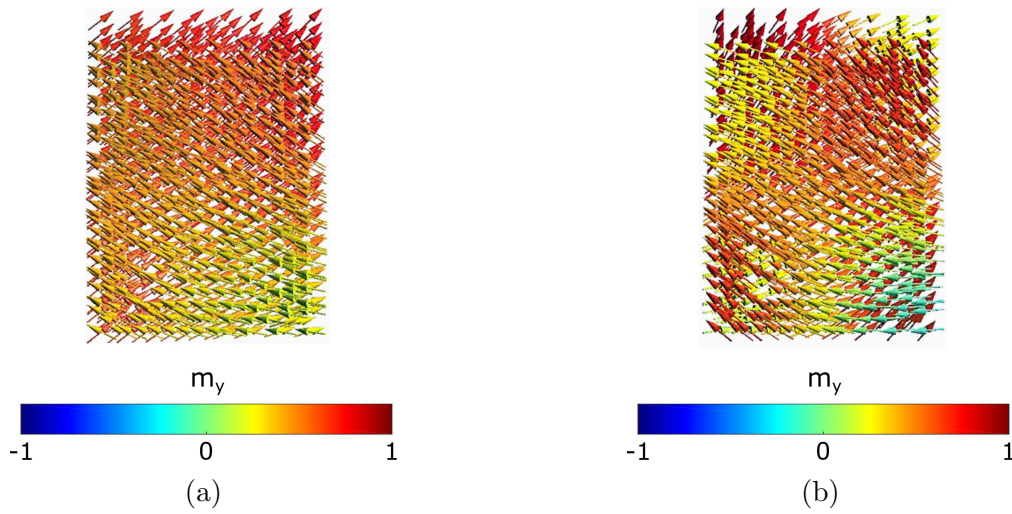


Fig. 16. The micromagnetic simulation showed that the (a) lower and (b) upper higher-order non-uniform modes are complex four-fold symmetry modes [57].

Finally, the absence of any large peaks (or “tails”) within (or extending to) the measured 30 GHz window allowed us to conclude that the intralayer couplings on the low/high M_s interfaces must be stronger than $2\text{--}3 \text{ erg/cm}^2$ ⁽⁵⁾, indicating good ferromagnetic coupling at these interfaces (Fig. 17).

⁽⁵⁾where $1 \text{ erg/cm}^2 = 10^{-3} \text{ J/m}^2$

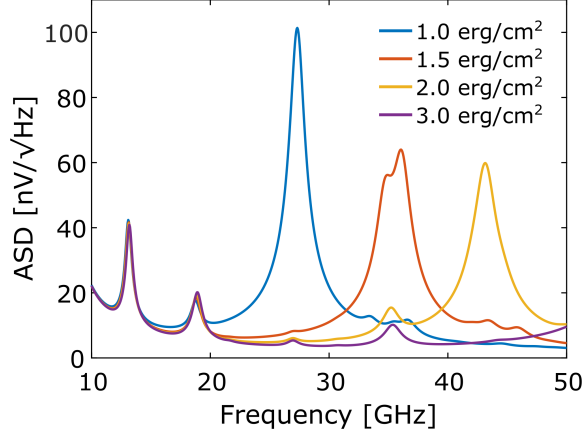


Fig. 17. Simulated ASD curves obtained for different intralayer couplings. Higher intralayer coupling strengths push intralayer modes to higher frequencies. Interfacial coupling strength between the low and high M_s layers (fig. 11) within each FL must be stronger than 2–3 erg/cm^2 .

3.2 Waveform analysis in time domain⁽⁶⁾

Krivorotov *et al.* made a convincing case on how a sampling oscilloscope can be used to capture the ST-induced time-dependent magnetization dynamics, including transients [23]. This measurement technique might be useful in the development of practical spintronics-based devices as it allows a direct observation of, *e.g.*, the ST-driven magnetization reversal. We would like to emphasize some important details that accompanied this study. First, to obtain the desired signal-to-noise ratio (SNR), the authors used trace averaging over multiple (*e.g.*, 2×10^4) measurements. This implies that the acquired measurements were phase-coherent, which was accomplished at the design stage by engineering the samples to have a well-controlled initial (equilibrium) angle between the FL and PL magnetic moments. Second, to minimize the random phase, the authors worked at low temperatures (≤ 40 K) using a temperature-controlled probe station.

The read head samples in our possession did not allow for adequate control over the initial angle between the FL and PL magnetic moments. Moreover, the read heads' time-domain performance in an uncontrolled environment would be of more interest because it can clarify the question of their reliability. As discussed in Section 1.2, the sampling oscilloscope used in [23] requires a *repetitive* waveform. To capture one-time temperature- or ST-induced instabilities in magnetization dynamics would require a real-time oscilloscope. These instabilities can be thought of as the evolution of the FMR spectral lines over time.

As illustrated in Fig. 18, an equivalent-time sampling oscilloscope triggers and samples differently than a real-time oscilloscope. The real-time oscilloscope does not require an

⁽⁶⁾The results of this section are presented in part at [60].

explicit trigger whose main task is to provide a horizontal time reference point for the incoming data. The scope samples the amplitude of the input waveform, stores that value in memory, and continues to the next sample as shown in Fig. 18b. The equivalent-time sampling scope does need an explicit trigger in order to operate, and this trigger must be synchronized with the input data. The sampling works as follows. A trigger event initiates the acquisition of the first sample. Then, the scope re-arms and waits for another trigger event. The next trigger event initiates the second acquisition and adds a small delay before sampling the second data point. This process is repeated until the entire waveform is acquired as illustrated in Fig. 18a. Comprehensive application notes elaborating on the difference between an equivalent-time sampling oscilloscope and a real-time oscilloscope can be found in [24, 61].

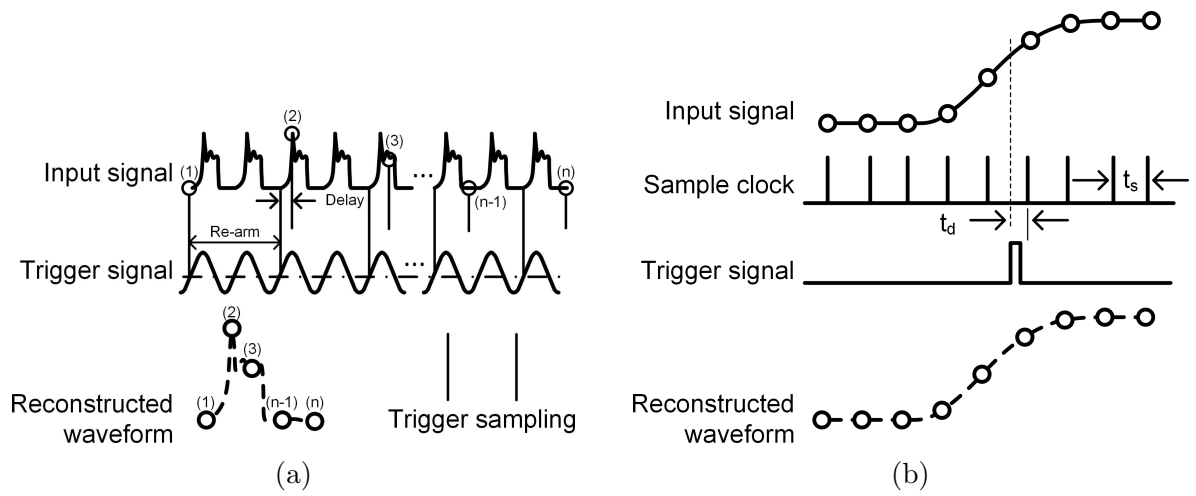


Fig. 18. Waveform acquisition using a (a) sampling or (b) real-time oscilloscope

The experimental waveforms were acquired with a Keysight DSO91204A oscilloscope limited by 1 Gpts memory and 40 GSa/s sample rate. Then, an exemplary waveform was analyzed *via* the short-time Fourier transform (STFT) technique⁽⁷⁾, which is one of the simplest time-frequency analysis techniques. In practice, the STFT is implemented as a sliding window and can be thought of as a spectral representation of an input signal at a given time; it can also be viewed as a function of time for each frequency.

The STFT of the signal $x[n]$ is defined as [62]

$$\dot{X}[k, l] \triangleq \frac{1}{M} \sum_{m=1}^M w[m] x[m + lH] e^{-j2\pi \frac{mk}{M}}, \quad (74)$$

where $k \in \{1, \dots, M\}$ is the index of a frequency bin, $l \in \mathbb{N}$ is the frame index, $m \in \{1, \dots, M\}$ is the local time index (*i.e.*, index relative to the beginning of the sliding

⁽⁷⁾STFT routine used in this work: <https://www.mathworks.com/matlabcentral/fileexchange/45197-short-time-fourier-transform-stft-with-matlab>

window), $w[m]$ is the window function, $M \in \mathbb{N}$ is the window length, and $H \in \mathbb{N}$ is the hop size (*i.e.*, the time advance, expressed in samples, from one signal frame to the next).

The term $\dot{X}[k, l]$ corresponds to the signal's local time-frequency behavior around the time index lH and the frequency bin k . If the sampling frequency is denoted as f_s , the above-mentioned indices correspond to the continuous time $t = lH/f_s$ and linear frequency $f = kf_s/K$, where K is the discrete Fourier transform size. Finally, the magnitude squared of the STFT yields the spectrogram [62–64].

The spectrogram's fragment in Fig. 19a was obtained with the following signal processing considerations. The time-frequency analysis' properties are a matter of resolution. In this context, resolution denotes the ability to distinguish between two spectral peaks (in the frequency domain) or instability events (in the time domain). Since we used the STFT, our main variable is the window function, which should provide a sufficient frequency and time resolution as well as adequate amplitude resolution (optimizing frequency resolution comes at the expense of time resolution and vice versa). In the present study, we used the Blackman window, which has a small time-bandwidth product, strong side-lobes attenuation of approximately -60 dB (important for the amplitude resolution), and medium main-lobe width (important for the frequency resolution) [25]. Finally, the window length should be equivalent to the time during which the recorded signal can be considered stationary. For most applications, the recommended number of overlapped samples is 50–75% of the window length [62–66].

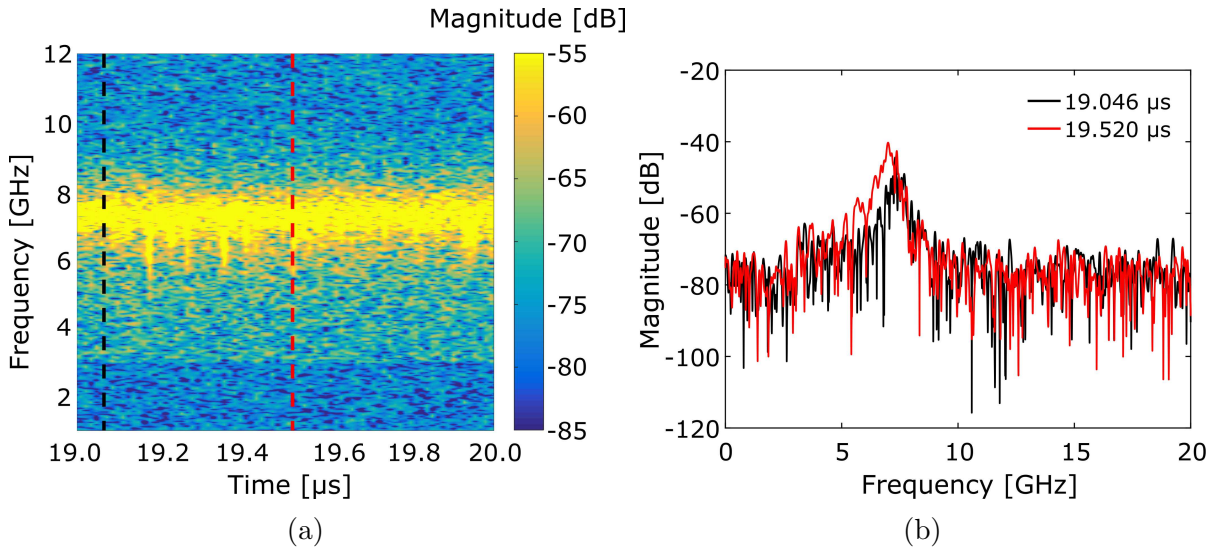


Fig. 19. (a) Spectrogram of the measured waveform and (b) its cross-sections at a given time indicating the FL mode instability. The measurement was performed on a short stripe height (reduced y -axis length) read sensor at $+600 \mu\text{A}$ DC bias current.

In the spectrogram, we discovered time instances when the FL mode broadens, increases in amplitude, and shifts over frequency. To track fast time variations in the FL mode, we

sacrificed frequency resolution. Nevertheless, the spectral cross-sections (Fig. 19b) plotted at 19.046 and 19.520 μs resolved the frequency shift between the two time instances of around 0.464 GHz. Appendix A describes the signal processing procedure that was used to obtain the measurements in Fig. 19.

We suggest the following reasons for such evolution of the FL FMR mode over time: 1) DC-driven transition to the nonlinear regime; 2) appearance of another mode, whose frequency is *accidentally* close to the FL FMR frequency but has a qualitatively different spatial location of the oscillation power; 3) switching between the FL's two metastable "S" states. The DC-driven transition to the nonlinear regime, however, usually appears as a *systematic* FL FMR frequency shift with an increasing absolute value of the DC bias and might eventually result in the FL mode foldover (Fig. 13). In contrast, FL mode's frequency "jumps" over time shown in Fig. 19a resemble an interaction of two coupled sub-systems (*i.e.*, modes) appearing as the FL mode splitting, thus making suppositions 2) and 3) more probable.

3.3 Summary

The two measurement techniques (spectrum analysis in frequency domain and waveform analysis in time domain) discussed in this chapter were already standardized for electrical characterization of the FMR in multilayers. In this work, we demonstrated that these techniques can still be used to uncover new physical phenomena. We utilized the spectrum-analyzer-based FMR to study the magnetic coupling in DFL sensors. Using this technique, we identified that higher couplings on the low/high M_s interfaces push the intralayer modes to higher frequencies, which is an indirect measure of the ferromagnetic coupling strength at these interfaces. Furthermore, we used the real-time oscilloscope to quantify instabilities in the FMR spectral lines, which may contribute to the read sensors' low-frequency magnetoresistance noise.

4 Coupling between the AC excitation signal and magnetization precession

The objective of this chapter is to gain more insight into the magnetic tunnel junctions' (MTJs') magnetization dynamics driven by a combination of AC and DC signals. The resultant signals of interest are naturally weak. Due to the broadband nature of the analyzer used in electrical ferromagnetic resonance (FMR) measurements, the detectable signal levels are limited by the intrinsic noise of the instrumentation. Earlier FMR measurements demonstrated that frequency-domain characterizations can overcome measurement limitations caused by the instrument's design. Firstly, the spectrum analyzer performs filtering, which enables accurate measurements of weak signals in the presence of relatively strong excitation signals. Secondly, the spectrum analyzer also allows the detection of transient signals that do not have a stable phase relation with the excitation signal. Meanwhile, the linear vector network analyzer (VNA) requires synchronization between drive and response signals. The "noise floor" investigated in Section 4.2 covers a frequency band that intentionally excludes the drive frequency, thus not requiring the drive and observation frequency to be the same or to have linear phase relation over time.

4.1 Vector network analysis in frequency domain

In Section 2.1, we demonstrated that a VNA can be used to characterize the read head system as a whole. The resultant S-parameters, or scattering parameters, revealed the system's RC roll-off characteristic coming from the parallel resistor and shield-to-shield capacitance (Fig. 8). The change in the tunnel magnetoresistance (TMR) sensor's complex impedance at FMR frequencies before and after applying the DC bias can also be detected with the VNA. In [22], Synogatch *et al.* presented the vector network analyzer-based ferromagnetic resonance (VNA-FMR) measurements of MTJ heads and contrasted the results to the FMR spectra obtained with the spectrum analyzer as described in Section 3.1. In the subsequent work by Xue *et al.*, the authors used the VNA to quantitatively measure the bias dependence of spin-torque (ST) in MTJs [26].

To understand how the FMR modes couple to the VNA's incident wave, let us first briefly review the fundamentals of vector network analysis [43]. As was mentioned in Section 2.1, the VNA uses the so-called "wave" quantities. The incident wave A_1 propagates from the analyzer to the device under test (DUT), while the reflected wave B_1 travels in the opposite direction from the DUT back to the analyzer (Fig. 20a).

Voltage and current V_1 and I_1 recovered from the wave variables are

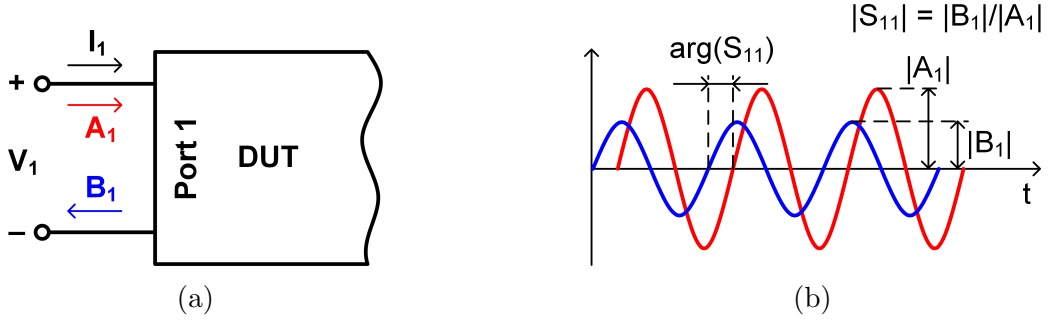


Fig. 20. Wave quantities and S-parameters: (a) one-port device with incident and reflected waves and (b) signals A_1 and B_1

$$\begin{aligned} V_1 &= \sqrt{Z_0}(A_1 + B_1), \\ I_1 &= \frac{1}{\sqrt{Z_0}}(A_1 - B_1). \end{aligned} \quad (75)$$

Wave variables A_1 and B_1 , in turn, can be written as linear combinations of V_1 and I_1 at Port 1:

$$\begin{aligned} A_1 &= \frac{1}{2\sqrt{Z_0}}(V_1 + Z_0 I_1), \\ B_1 &= \frac{1}{2\sqrt{Z_0}}(V_1 - Z_0 I_1), \end{aligned} \quad (76)$$

where A_1 , B_1 , V_1 , and I_1 can be considered the root-mean-square (RMS) vectors⁽⁸⁾.

The time-dependent sinusoidal voltage signal at Port 1 is equal to

$$v_1(t) = \text{Re} \left\{ V_1^{(pk)} e^{j\omega t} \right\}, \quad (77)$$

where $V_1^{(pk)}$ is the peak value.

Then, the time-dependent “wave” quantities are

$$\begin{aligned} v_1(t) &= \sqrt{Z_0}(a_1(t) + b_1(t)), \\ i_1(t) &= \frac{1}{\sqrt{Z_0}}(a_1(t) - b_1(t)). \end{aligned} \quad (78)$$

In the frequency domain, we obtain

⁽⁸⁾For a real signal $s(t) = \text{Re} \{ S e^{j\omega t} \}$ with a complex amplitude $S = S^{(r)} e^{j\phi}$ (where $S^{(r)}$ denotes the real amplitude), the complex amplitude’s RMS value is $S^{(RMS)} = S/\sqrt{2}$. Here, its vector representation is called the “RMS vector” [67].

$$\begin{aligned}
V_1(\omega) &= \sqrt{Z_0}(A_1(\omega) + B_1(\omega)), \\
I_1(\omega) &= \frac{1}{\sqrt{Z_0}}(A_1(\omega) - B_1(\omega)),
\end{aligned} \tag{79}$$

and

$$\begin{aligned}
A_1(\omega) &= \frac{1}{2\sqrt{Z_0}}(V_1(\omega) + Z_0 I_1(\omega)), \\
B_1(\omega) &= \frac{1}{2\sqrt{Z_0}}(V_1(\omega) - Z_0 I_1(\omega)).
\end{aligned} \tag{80}$$

If the described system is *linear*, then the relationship between the phasor representation of the incident and reflected waves yields Eq. (71). Thus, coupling between the VNA’s incident wave and magnetization precession translates into the amplitude ratio and phase difference between the two wave quantities A_1 and B_1 . The magnitude of S_{11} corresponds to the amplitude ratio of A_1 and B_1 , while the phase of S_{11} corresponds to the phase difference between A_1 and B_1 (Fig. 20b).

S-parameters are defined with the condition that the DUT behaves as a *linear* system. When the DUT behaves linearly relative to the applied port power, S-parameters are *independent* from the port power level [68]. If S-parameters change significantly with varying port power levels as in [22], the DUT can be said to be operating *nonlinearly*, negating the validity of S-parameters. In [26], Xue *et al.* verified that their device linearly translates the input to the output (as expected in the linear regime), thus resulting in the simulated magnetization precession angles of $< 3^\circ$.

In Fig. 21, we experimentally found the highest port power level, -10 dBm at ± 150 mV operating DC bias voltage, that should be applied to magnetic read heads while still assuring their linear behavior. Port powers significantly below this level should be avoided, but for a different reason. Sufficient power levels ensure high dynamic range, which is the difference between the measured power level and the noise floor [68].

Note that the VNA-FMR measurements in Fig. 21 differ from the thermal noise ferromagnetic resonance (T-FMR) power spectra in Fig. 12. Specifically, contrary to the power spectra, the VNA-FMR measurements acquired for opposite DC bias voltages are qualitatively different: FL “peak” at $+150$ mV *versus* FL “dip-peak” at -150 mV. Most importantly, Figs. 12 and 21 represent different physical quantities. A power spectrum is the distribution with frequency of the power content of the signal [69]. Meanwhile, by measuring the amplitude ratio and phase difference between A_1 and B_1 as a function of the excitation frequency, the VNA shows a frequency response [70]. Also, in contrast to the spectrum analyzer, the VNA provides the phase information (discussed below).

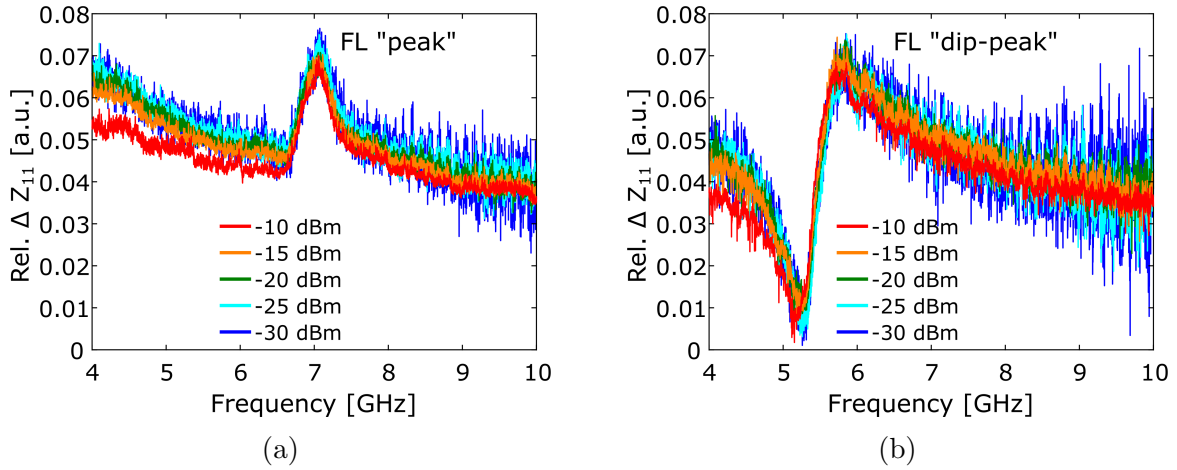


Fig. 21. VNA measurements of two different samples obtained with a Keysight N5230C at 50 Hz intermediate frequency bandwidth (IFBW) and different port power levels for (a) +150 mV and (b) -150 mV DC bias voltage. Positive DC bias corresponds to the electron flow from the pinned layer (PL) to free layer (FL).

The measurement dynamic range can be improved not only by increasing the port power but also by decreasing the VNA’s intermediate frequency bandwidth (IFBW) or by trace averaging [27]. As mentioned in Sections 1.2 and 3.2, we cannot sufficiently control the initial (equilibrium) angle between the read sensors’ free layer (FL) and pinned layer (PL2) magnetic moments. As a result, the phase between magnetization precession and the VNA’s incident wave is unstable. Thus, trace averaging can lead to the loss of small FMR signals in averaging while the IFBW must be sufficiently lowered to retrieve the sought after FMR modes. In Fig. 22, we fail to recover the FL’s “dip-peak” feature if the IFBW exceeds 10 kHz.

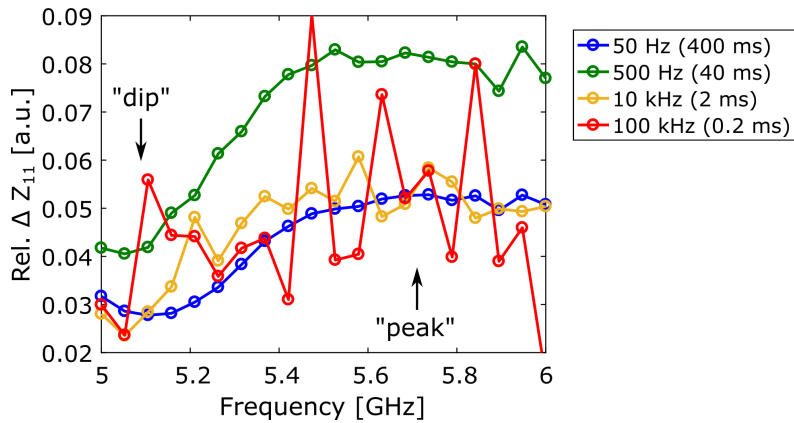


Fig. 22. VNA measurements obtained at -10 dBm port power and -150 mV DC bias voltage for different IFBW’s. The number in parentheses is the corresponding sweep time.

Unfortunately, any change in the IFBW also influences the sweep time (number in parentheses in Fig. 22). Sweep time specifies the time the VNA requires to collect data for one measurement sweep. For small IFBW’s, these two quantities are inversely proportional:

if the number of measurement points is the same, doubling the IFBW cuts the sweep time in half. For large IFBW's, however, other settings (*e.g.*, constants for the phase lock loops) become predominant [43].

De-embedding is intended to remove the effect of the extrinsic device components (*i.e.*, magnetic shields, parallel resistor, sputtered and plated leads as well as contact pads) and move the reference plane from the contact pads to the MTJ itself (Fig. 7). At the early stage of this work, we did not perform de-embedding and recovered the FMR modes from the VNA measurements by plotting the relative impedance change between select non-zero and zero DC bias levels. Thus, "Rel. ΔZ_{11} " in Figs. 21 and 22 is defined as $|Z(\omega) - Z_0(\omega)|/|Z_0(\omega)|$. In practice, the large RC time constant coming from the parallel resistor and shield-to-shield capacitance masks the MTJ's magnetization dynamics, thus requiring de-embedding. To plot S_{11} and Z_{11} in Fig. 23, we did perform de-embedding based on the one-port error model [71].

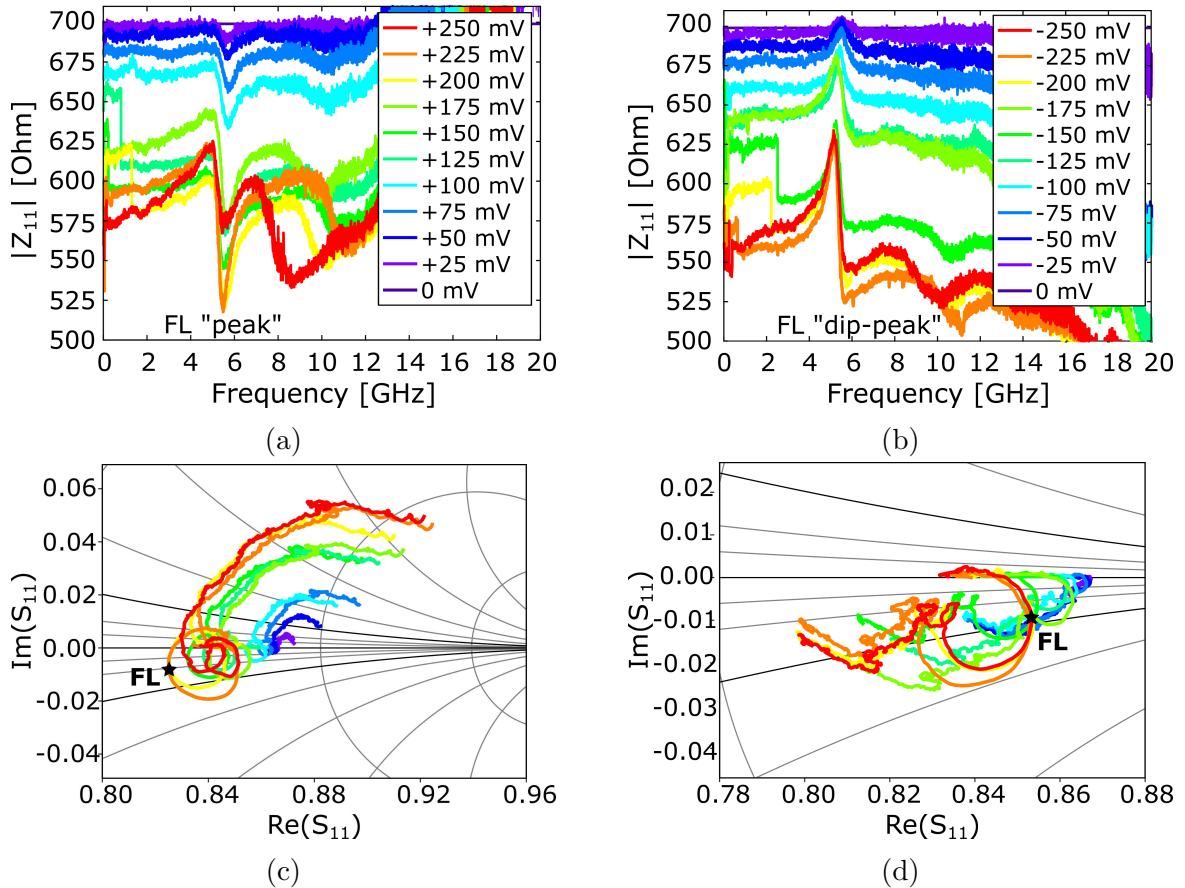


Fig. 23. VNA measurements obtained with a Keysight N5247A at 500 Hz IFBW and -10 dBm port power for (a), (c) positive and (b), (d) negative DC bias voltage polarity.

For positive V_{DC} , S_{11} shows only one resonant circle corresponding to a peak on the Z_{11} versus frequency plot. In contrast, for negative V_{DC} , there are two resonant circles corresponding to the dip-peak scenario. At $V_{DC} \geq +100$ mV, there is a resonant circle offset from the center, which may be related to the peak shape becoming more asymmetric.

For negative values of $V_{\text{DC}} \geq -150$ mV, there is only one resonant circle indicating a symmetric dip on the Z_{11} *versus* frequency plot. Lastly, there is a phase shift of about 90° between the positive and negative V_{DC} scenarios. Appendix B is a useful reference for understanding how to interpret resonant modes mapped onto the complex plane.

Synogatch *et al.* reported similar observations of the S_{11} asymmetry with respect to polarity of the DC bias current and field [22]. The authors suggested the following reasons for the peak-to-dip transformation: 1) Current flowing through the MTJ head creates an approximately circular, in-plane magnetic field at the edges of the device. Therefore, the abovementioned asymmetry with respect to the DC bias current polarity can be attributed to whether this field is parallel or anti-parallel to the FL magnetization at the edges due to the asymmetry of the Oersted field relative to the MTJ. 2) Changes in the FL FMR response can be related to switching between its magnetic states. 3) Effects of the spin-polarized current are also asymmetric with respect to the DC bias current polarity.

Sankey *et al.* observed both types of asymmetries using an alternative FMR measurement technique utilizing the same excitation but different readout mechanism (see Section 5.1 for more detail). In [31], the authors reported the FMR lineshape evolution (from peak to dip-peak) with respect to the absolute value of the DC bias current. In [72], the authors observed strong dependence of the FMR lineshape on the DC bias current polarity. The authors attributed the asymmetric Fano shape to the phase difference between the AC excitation signal and the DC-driven magnetization precession.

In our experiments, the resultant VNA measurements also indicate two types of asymmetries in the FL FMR lineshape: 1) peak- *versus* dip-shaped FL mode with respect to the DC bias voltage polarity and 2) transition from symmetric to asymmetric Lorentzian with increasing absolute value of the DC bias voltage. The first observation coincides with the 90° -degree phase shift, thus supporting the supposition expressed in [72]. The second observation, in turn, may be attributed to the FMR response transitioning to the nonlinear regime.

4.2 Strong coupling between the AC excitation signal's phase noise floor and magnetization precession⁽⁹⁾

To understand the physical effect behind coupling between the vector network analyzer's (VNA's) incident wave and magnetization precession driven by a combination of the AC and DC signals (Section 4.1), we designed a measurement system displaying the

⁽⁹⁾The results of this section are published in part in [73].

reader's response at a given excitation frequency point (Fig. 24). A Krytar 1850 directional coupler⁽¹⁰⁾ is used to make the radio frequency (RF) wave travel towards the reader before being reflected in the direction of an Agilent E4446A spectrum analyzer. An Agilent E3634A DC power supply provides the DC bias so that the sample is excited by a combination of AC and DC signals. An Agilent E8244A signal generator's frequency is swept from 1 to 20 GHz.

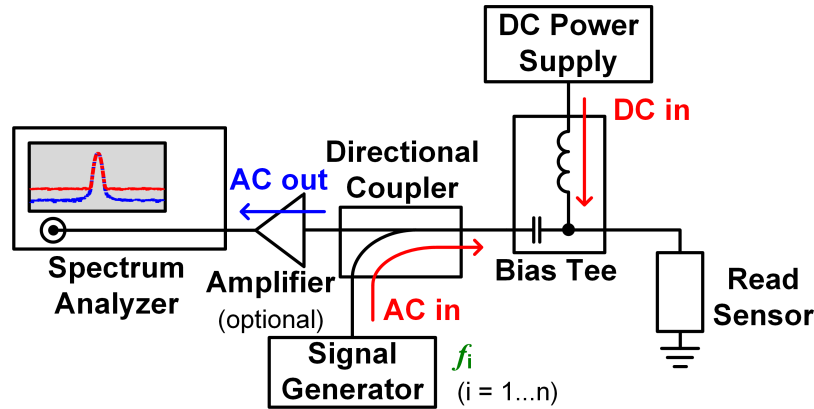


Fig. 24. Measurement system designed to investigate the coupling mechanism between the AC excitation signal and magnetization precession. At each frequency point f_i , the spectrum analyzer displays the noise level difference ΔNL between the spectra at zero and non-zero DC bias.

At each excitation frequency, we observe the noise level difference ΔNL between the two states: at zero and non-zero DC bias. Figure 25 shows that at non-zero DC bias, magnetization precession coupling to the AC carrier's phase noise produces an increase in the phase noise floor level while the carrier's amplitude stays mostly unchanged. The closer the excitation frequency f_i to the reader's FL FMR mode, the greater the ΔNL .

Assuming that we operate below the critical current required for steady-state magnetization precession, thermally-excited magnetization fluctuations would indeed appear as phase noise sidebands around f_i , displayed as a continuous spectrum over a range of frequencies around the AC carrier (Figs. 25a and 25b) similar to that of broadband noise. This occurs because magnetization fluctuations have no stable phase relation with the AC excitation signal. Thus, the contribution of these thermally-excited magnetization fluctuations is directly proportional to the rise in the AC carrier's phase noise floor. In the VNA-FMR measurement (Section 4.1), in turn, sufficient reduction in the VNA's IFBW seems to create false stability by "smoothing" phase variations.

The absence of artifacts in the measurement system (Fig. 24) was verified by characterizing OPEN, 50Ω LOAD⁽¹¹⁾, and fixture without the junction (Fig. 7). Moreover, we compared

⁽¹⁰⁾There is a 16-dB loss at the directional coupler's coupling port. In addition to transmission losses, we can say that there is ≈ 20 -dB total loss compared to the source power level stated in Figs. 25 to 28.

⁽¹¹⁾OPEN, SHORT, and LOAD is a set of physical devices called "standards." Each standard has a

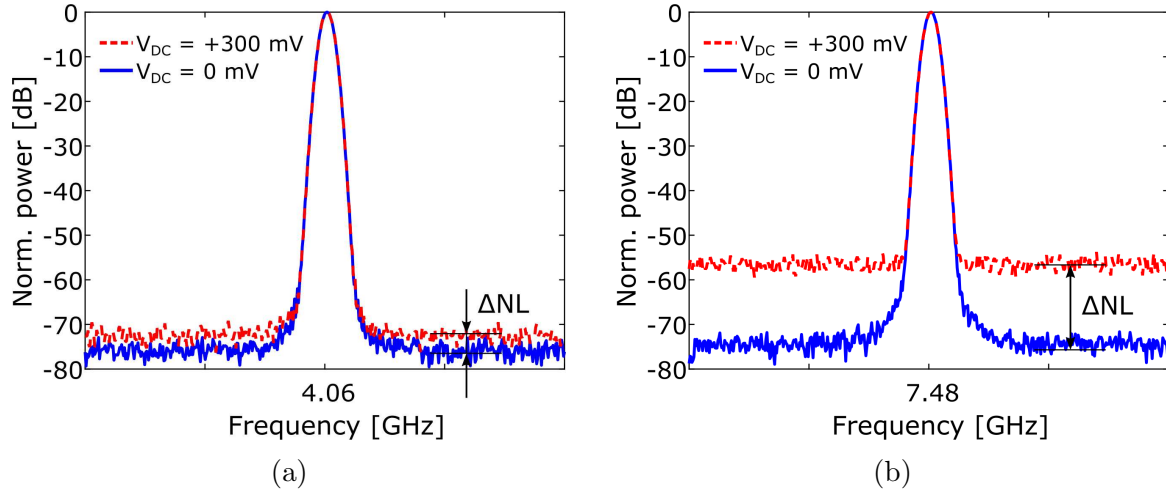
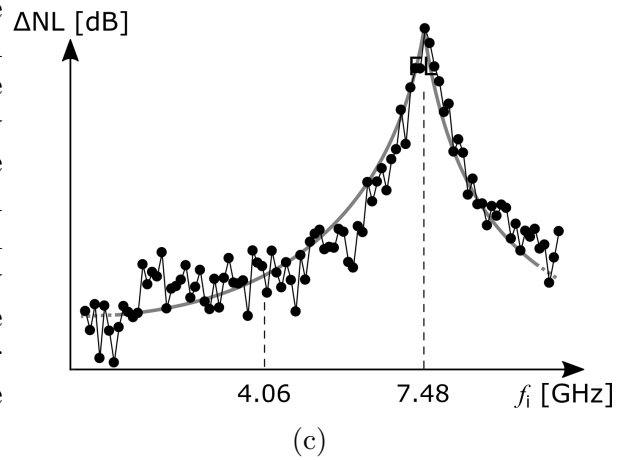


Fig. 25. Change in the noise floor with the DC bias voltage measured (a) away from and (b) around the central frequency of the FL mode. (c) Exemplary ΔNL spectra show the noise level difference as a function of the signal generator's frequency f_i swept around the FL mode. Signal generator's power level is -50 dBm. Spectrum analyzer's frequency span and resolution bandwidth (RBW) are 20 kHz and 500 Hz, respectively. DC power supply's positive DC bias corresponds to the electron flow from the PL to the FL.



the ΔNL spectrum with the T-FMR measurement obtained under the same DC biasing condition. Following the description in Section 3.1, the T-FMR spectrum in Fig. 26 was obtained with the spectrum analyzer by the direct observation of the high-frequency magnetization precession of the FL and pinned layer (PL) under the DC bias current. Figure 26 convincingly states that whether the AC excitation is at a low level or entirely absent, the ΔNL spectrum indeed approaches the T-FMR measurement. As opposed to a *broadband* DC, the AC source provides an additional *frequency-selective* excitation.

In this work, we characterized seven read sensors coming from five different wafers. The results were consistent with ΔNL power spectra obtained from two samples for a set of AC power levels and DC bias voltages (Figs. 27 and 28, respectively). Higher signal generator's power levels revealed peaks not only at the devices' natural FMR modes but also at $1/3$ the frequency of the FL and PL. The FL mode also exhibits a “satellite” peak, which is right above the FL FMR frequency. This feature can be descriptively characterized as “mode splitting.” Interestingly, peaks at $1/3$ the frequency of the FL and PL also exhibit “mode splitting” at higher AC power levels (Fig. 27).

precisely known or predictable magnitude and phase response as a function of frequency.

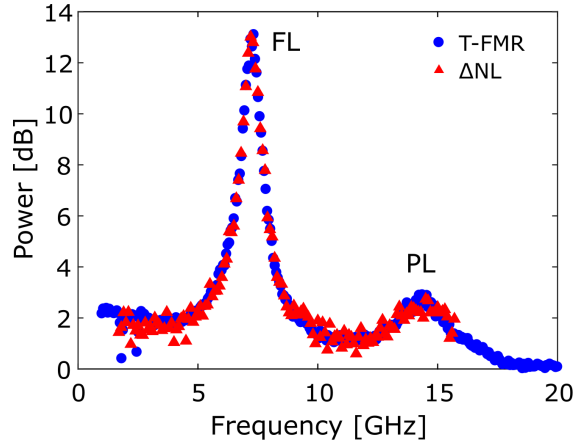


Fig. 26. ΔNL plotted *versus* the observation frequency is equivalent to the T-FMR spectrum (Section 3.1). Both spectra are obtained at $+250 \mu\text{A}$ DC bias current. To obtain the T-FMR spectrum, the spectrum analyzer’s RBW is set to 51 kHz. To obtain the ΔNL power spectrum, the signal generator’s power level is set to -10 dBm , while the measurement frequency span and RBW are 1 kHz and 5 Hz, respectively.

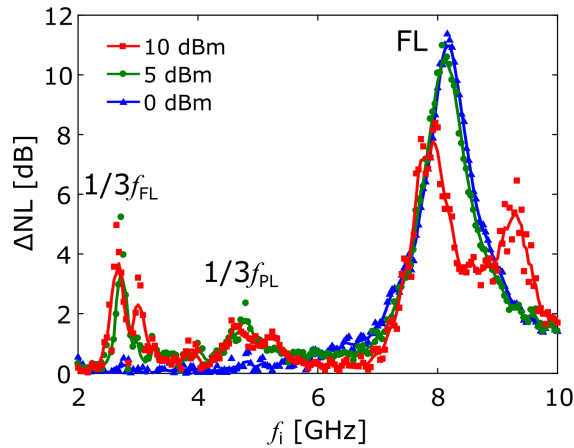


Fig. 27. The ΔNL power spectra show the low-frequency peaks that are distinct from the FL mode as well as the “satellite” peaks. The spectra are obtained at $+300 \text{ mV}$ DC bias voltage. The measurement frequency span and RBW are 10 MHz and 2 kHz, respectively.

Compared with the commonly used FMR techniques, the measurement system in Fig. 24 has several main advantages: 1) Because the measurement is obtained as the difference between the two power spectra, the background noise present in the measurement system is inherently rejected. Here, the background noise is defined by the amplifier, cabling, measurement instruments, *etc.* 2) As with other commonly used FMR techniques in the frequency domain, the described measurement system’s observation time is independent of the FL/PL relaxation time constants. 3) To observe the sought after phenomenon, the spectrum analyzer’s RBW can be significantly reduced (*e.g.*, 5 Hz in Fig. 26), which improves the system’s noise performance.

The presented FMR measurement technique does not require a single frequency offset, where ΔNL must be measured, the caveat being that the measurement frequency should

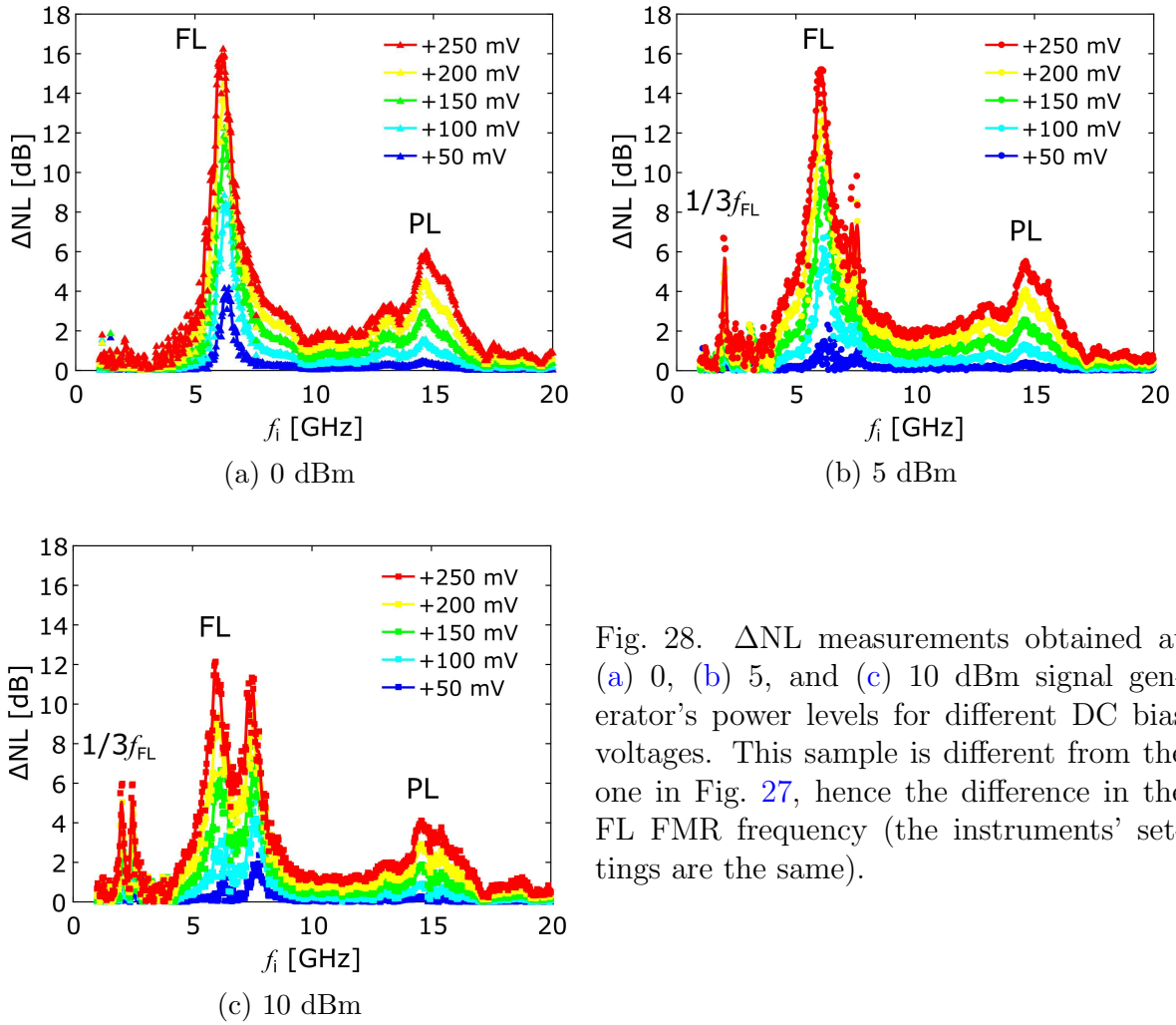


Fig. 28. ΔNL measurements obtained at (a) 0, (b) 5, and (c) 10 dBm signal generator's power levels for different DC bias voltages. This sample is different from the one in Fig. 27, hence the difference in the FL FMR frequency (the instruments' settings are the same).

be neither: 1) too close to the excitation frequency to avoid overloading the spectrum analyzer's receiver nor 2) too far away from the excitation frequency to avoid measuring the spectrum analyzer's phase noise floor. We empirically identified the 700-MHz frequency offset used to obtain the ΔNL spectra in Figs. 26 to 28.

Another reason for an offset between the excitation and measurement (or observation) frequencies comes from the spectrum analyzer design. In particular, the sophistication of the phase-lock loops employed to stabilize the local oscillator determines the *shape* of the phase noise spectrum as shown in Fig. 29. In some spectrum analyzers, the phase noise is a relatively flat pedestal. In others, the phase noise may fall away as a function of frequency offset from the signal [74].

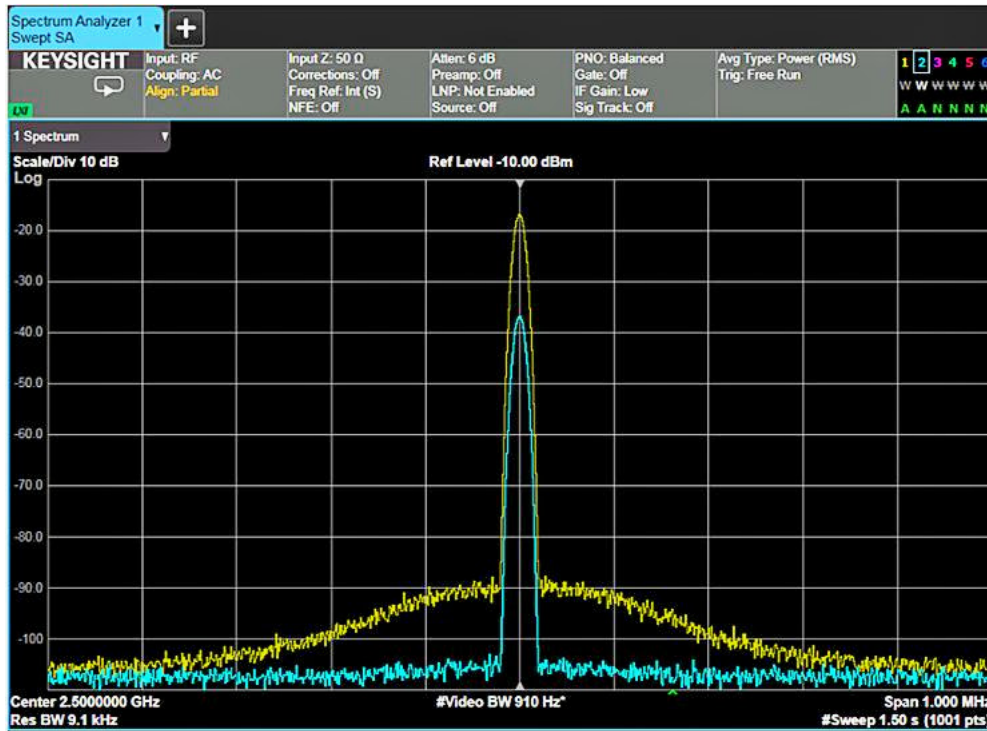


Fig. 29. Flat and pedestal-like shape of the phase noise spectrum

4.3 Summary

In this chapter, we proposed a new measurement technique to characterize FMR arising from magnetization precession that has no stable phase relation with an AC excitation signal. We measure the phase noise floor difference between the two states—at zero and non-zero DC bias—as opposed to relying on weak coupling (due to slow convergence to a steady-state phase locking) between the AC excitation signal and magnetization dynamics. The phase noise floor difference is due to the ferromagnetic layers' magnetization dynamics adding to the phase noise floor of the AC excitation signal. The proposed FMR measurement technique revealed new spectral lines, whose presence is confirmed using an alternative measurement technique that utilizes the same excitation but different readout mechanisms (see Section 5 for more detail).

5 DC and harmonic response resulting from strongly nonlinear magnetization dynamics

Magnetization dynamics are inherently nonlinear because magnetization oscillations arise from the precession of the magnetization vector with a constant magnitude, leading to the following nonlinear relation of the magnetization components [75]:

$$m_x^2 + m_y^2 + m_z^2 = 1. \quad (81)$$

Hence, for small deviations from the x -axis ($m_x \approx 1$), we can apply the Taylor expansion to the x component of the magnetization vector as follows:

$$\begin{aligned} m_x &= [1 - (m_y^2 + m_z^2)]^{1/2} \\ &= 1 - \frac{1}{2} (m_y^2 + m_z^2) - \frac{1}{8} (m_y^2 + m_z^2)^2 - \frac{1}{16} (m_y^2 + m_z^2)^3 + \dots \end{aligned} \quad (82)$$

Assuming a harmonic solution

$$\begin{aligned} m_y &= m_{y0} \cos(\omega t + \phi_{y0}), \\ m_z &= m_{z0} \cos(\omega t + \phi_{z0}), \end{aligned} \quad (83)$$

we obtain

$$\begin{aligned} m_x &= 1 - \frac{1}{4} (m_{y0}^2 + m_{z0}^2) - \frac{3}{64} (m_{y0}^4 + m_{z0}^4) - \frac{1}{16} m_{y0}^2 m_{z0}^2 \\ &\quad - \frac{1}{32} m_{y0}^2 m_{z0}^2 \cos(2\phi_{y0} - 2\phi_{z0}) \\ &\quad - \frac{1}{4} m_{y0}^2 \cos(2\omega t + 2\phi_{y0}) - \frac{1}{4} m_{z0}^2 \cos(2\omega t + 2\phi_{z0}) \\ &\quad - \frac{1}{16} m_{y0}^4 \cos(2\omega t + 2\phi_{y0}) - \frac{1}{16} m_{z0}^4 \cos(2\omega t + 2\phi_{z0}) + \dots \end{aligned} \quad (84)$$

Equation (84) contains the DC component determined by m_{y0} and m_{z0} as well as the higher-order harmonics of the resonant precession frequency f .

Both the tunnel magnetoresistance (TMR) and spin-torque (ST) effects are nonlinear

since they strongly depend on the precession angle. We briefly described the TMR's angular dependence in Section 2.3. Meanwhile, in Eq. (31), the angular dependence of the Slonczewski torque's amplitude is given by [76, 77]⁽¹²⁾

$$a_j \propto \frac{2\Lambda^2}{(\Lambda^2 + 1) + (\Lambda^2 - 1) \cos \theta}, \quad (85)$$

where the angle θ is defined between the adjacent layers' magnetizations (*i.e.*, free layer (FL) and pinned layer (PL2) in Fig. 9a). The asymmetry parameter Λ depends on the sample configuration and various transport coefficients.

Experimentally, these nonlinear characteristics are most widely described with respect to their nonlinear bias (voltage or current) dependence. The nonlinear TMR effect is analyzed using simple I - V curves and analytically described by the, *e.g.*, generalized Brinkman's model:

$$I(V) \approx f_1(\bar{\Phi})V + f_2(\bar{\Phi})\Delta\Phi V^2 + f_3(\bar{\Phi})V^3, \quad (86)$$

where f_1 , f_2 , and f_3 are the functions of the average tunnel barrier height $\bar{\Phi} = \frac{1}{2}(\Phi_1 + \Phi_2)$. $\Delta\Phi = \Phi_1 - \Phi_2$ is the barrier asymmetry. Rough interfaces may also contribute to nonlinearities in I - V curves by modifying the spin-dependent interface transmission function [79, 80].

As for the nonlinear ST effect, the bias-voltage dependence of the two ST terms [Eq. (31)] can also be expressed *via* polynomials and extracted from a simple DC measurement as a function of applied magnetic field and bias voltage [81]:

$$\begin{aligned} a_j(V) &= a_1V + a_2V^2 + \dots \\ b_j(V) &= b_1V + b_2V^2 + \dots \end{aligned} \quad (87)$$

When the magnetization precession angles become large, the system's nonlinearities start playing an important role in magnetization dynamics. To directly observe their manifestation, one must go beyond the static bias-voltage characterization. In this chapter, we describe several measurement tools suitable for high-frequency *nonlinear* characterization of the magnetic tunnel junctions (MTJs) response under various experimental conditions (*e.g.*, DC bias level and AC power).

⁽¹²⁾To describe the ST's angular dependence in MgO-based junctions, we used the common formulations for metallic junctions. Recent work (Ref. [78]) shows that the effective difference in angular dependence for these two scenarios is insignificant.

5.1 Steady-state DC readout

Following Eq. (84), we would like to briefly introduce the linear systems' (or devices') fundamental properties that differentiate them from nonlinear ones. First, linear systems are signal operators, which obey superposition: if the input is the sum of two elementary signals, then the output can be represented as the sum of the two outputs to these elementary signals taken individually. Also, linear systems can *modify* amplitude and/or phase of each spectral component as shown in Fig. 30b. They *do not eliminate or generate* new ones. In contrast, nonlinear systems can qualitatively modify spectra by eliminating or generating spectral components as shown in Fig. 30c [82].

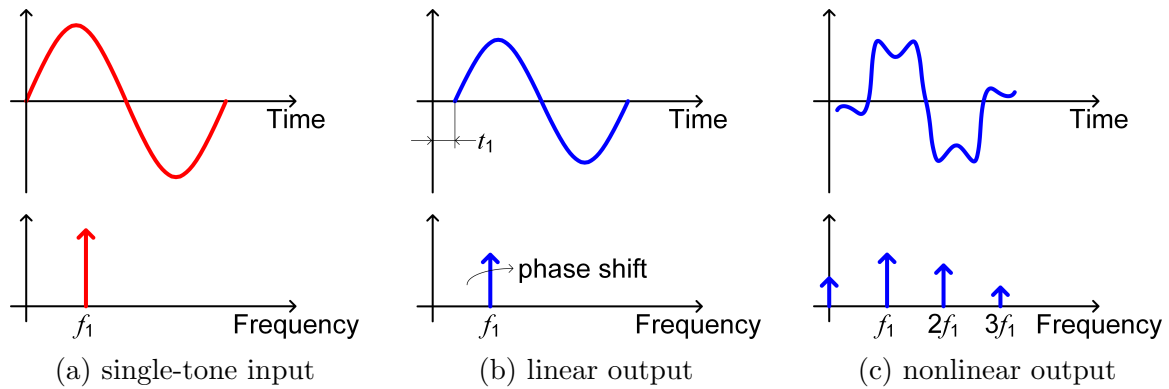


Fig. 30. Using a single-tone stimulus signal (a), linear devices' input and output frequencies remain the same (b), while nonlinear devices generate harmonics (c).

We devote this section to the calculation and characterization of the MTJ heads' DC spectral component. To replicate the measurement system in Fig. 5, we start with the definition of the voltage induced in the system, which is subjected to both DC and AC currents:

$$I = I_{DC} + I_{AC} \sin(\omega t). \quad (88)$$

In the presence of the TMR effect, the system's resistance has two constituents: magnetization-independent ohmic resistance R_0 and magnetization-dependent, TMR-caused resistance $R_{TMR}(t)$. Hence, the resultant time-dependent voltage response is

$$V(t) = I(t)R(t) = [I_{DC} + I_{AC} \sin(\omega t)] \times [R_0 + R_{TMR}(t)]. \quad (89)$$

If I_{DC} is less than the critical current above which the ST-induced steady-state oscillations arise, the only excitation present in the system is the periodic AC current. Thus, the time-dependent magnetization resulting in the time-dependent TMR term is a periodic

function with a period $T = 2\pi/\omega$. Due to various sources of nonlinearities in the system, the TMR-caused resistance can be non-harmonic and subsequently be expressed as a Fourier series:

$$R_{\text{TMR}}(t) = R_{\text{TMR}}^{\text{av}} + \sum_{n=1}^{\infty} a_n \cos(n\omega t) + \sum_{n=1}^{\infty} b_n \sin(n\omega t), \quad (90)$$

where the Fourier coefficients a_n and b_n have the physical quality of resistance. The averaged $R_{\text{TMR}}^{\text{av}}$ is determined by the magnetization oscillations' nonlinearity and is highly sensitive to the asymmetry parameter Λ . This is discussed in more detail in Section 6.3. Substituting Eq. (90) in (6.3) and then time-averaging the result produces the following DC voltage response:

$$V_{\text{DC}} = \langle V(t) \rangle = \underbrace{I_{\text{DC}} R_0 + I_{\text{DC}} R_{\text{TMR}}^{\text{av}}}_{\text{“constant”}} + \underbrace{\frac{I_{\text{AC}} b_1}{2}}_{\text{“oscillating”}}, \quad (91)$$

where all other higher-order terms disappear after time-averaging due to the orthogonality properties of harmonic functions.

In Eq. (91), the “constant” term comes from the magnetization-independent (ohmic resistance) and time-averaged magnetization-dependent, TMR-caused resistances. The “oscillating” term involves mixing the excitation signal with the TMR oscillations only at the same frequency [31]. It can also be seen that the contribution from the “oscillating” term depends on the phase condition between these two signals: maximum at 0° or 180° (in- or out-of-phase) and minimum at 90° or 270° (quadrature).

Experimentally, the MTJ heads' DC response can be extracted using the steady-state DC readout measurement technique described in Section 1.2. It uses the same excitation as the methods outlined in Section 4 but a different readout mechanism. The magnetic read sensor is excited with an AC signal (we used Keysight PNA-X N5247A as the AC source) for different DC bias currents, while the DC voltage across the sensor is measured with a sourcemeter.

The DC response at the free layer's (FL's) resonant precession frequency is especially pronounced at higher AC power levels (Fig. 31). Similar to the VNA-FMR, the DC readout measurements show that the FL mode's lineshape changes qualitatively (from “dip-peak” at $-250 \mu\text{A}$ to “dip” at $+250 \mu\text{A}$) when the direction of the DC bias current is reversed. At non-zero DC bias current, the DC readout curves exhibit frequency dependence, which may be associated with the predominant contribution of the second harmonic of B_1 (the supporting data and explanation will follow in Section 5.3).

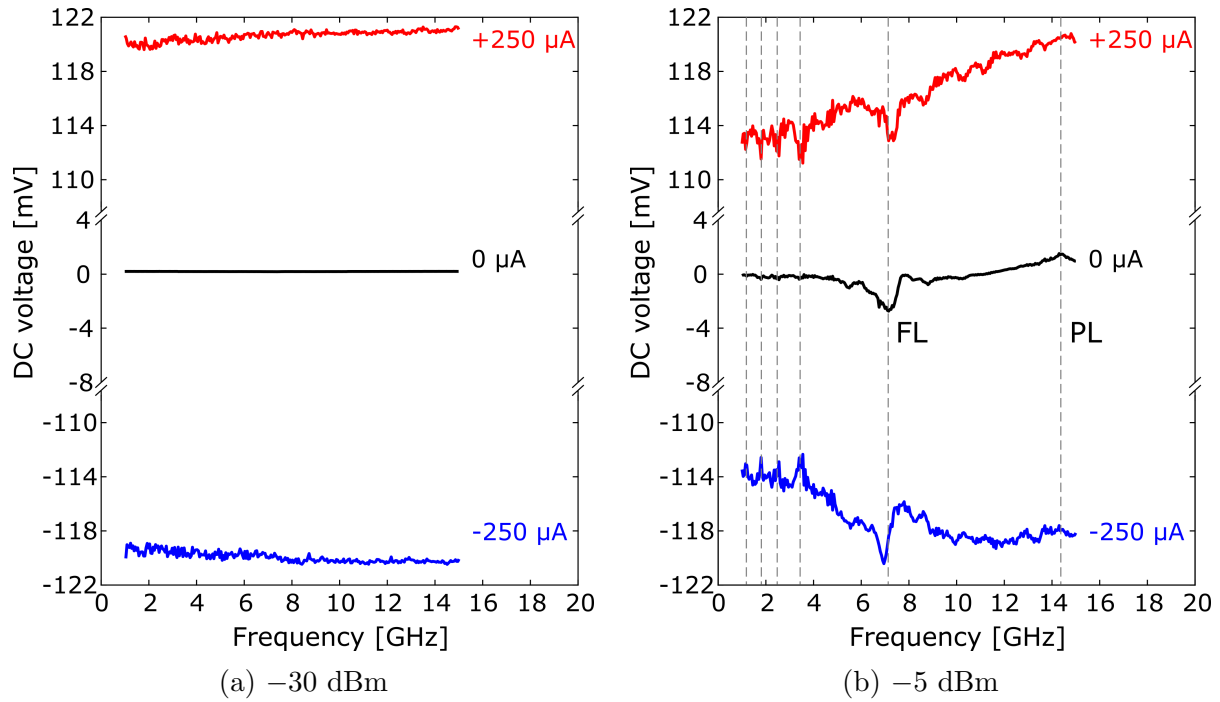


Fig. 31. DC frequency response obtained with a Keysight N5247A for (a) -30 dBm and (b) -5 dBm port power levels. A Keithley 2400 sourcemeter is used to supply the device under test (DUT) with a DC bias current and measure the resultant DC voltage response. Positive DC bias corresponds to the electron flow from the PL to FL.

Moreover, at non-zero DC bias current, the DC readout measurements reveal peaks at lower frequencies than the FL mode. Namely, they are located at fractional frequencies ($1/2$, $1/3$, $1/4$, and $1/6$) of the FL's resonant precession frequency (Fig. 31b). One of the similar observations was made in a micromagnetic study of the current-perpendicular-to-plane (CPP) spin valve heads under ST excitation [83]. The subsequent study of ST-induced magnetization dynamics in thin magnetic nanoelements demonstrated that nanoelements of a certain size can exhibit splitting of their magnetization precession trajectory into limiting sub-cycles [84]. In the spectrum, these sub-cycles corresponded to peaks at frequencies lower than that of the complete motion cycle. In [84], this regime precedes the state of chaos characterized by strongly inhomogeneous large-angle magnetization precession producing chaotic trajectories and almost continuous spectrum with no distinct ferromagnetic resonance (FMR) peaks. In both micromagnetic studies, however, the state of bifurcation is characterized by the presence of peaks at the fractional frequencies of the natural FMR mode in a narrow range of applied DC bias currents (2.8 to 3.6 mA) or sizes of nanoelements (40 to 52 nm) [83, 84]. In contrast, we observe peaks at the FL's fractional frequencies in a wide range of applied AC and DC signals. This requires an alternative explanation, which is provided in the subsequent sections.

5.2 Harmonic response under one- and two-tone AC excitation signal⁽¹³⁾

Static I-V curve measurements are commonly used to characterize read sensors' nonlinear effects. Unfortunately, these do not capture the sensors' magnetization *dynamics*. In the following sections, we explore the use of the one- and two-tone measurement techniques (commonly used in microwave engineering) for better treatment of the sensors' nonlinear effects in conjunction with dynamic ones.

5.2.1 One-tone measurement

We devote this section to characterization of the higher-order harmonics produced in response to a single-tone stimulus signal (Fig. 30c) [86–88]. The fundamental frequency f_1 supplied by the signal generator is 1 GHz, which is the upper limit of the 2.5-inch hard drives' operating bandwidth. We measure the second and the third multiple of the fundamental frequency ($2f_1$ and $3f_1$) for various DC bias voltages. We go beyond the sensor's typical bias voltages, which range from 100 to 150 mV. The sensor can withstand AC input power levels up to -5 dBm. The AC and DC excitations are combined and applied directly through the radio frequency (RF) probe needle (Fig. 32).

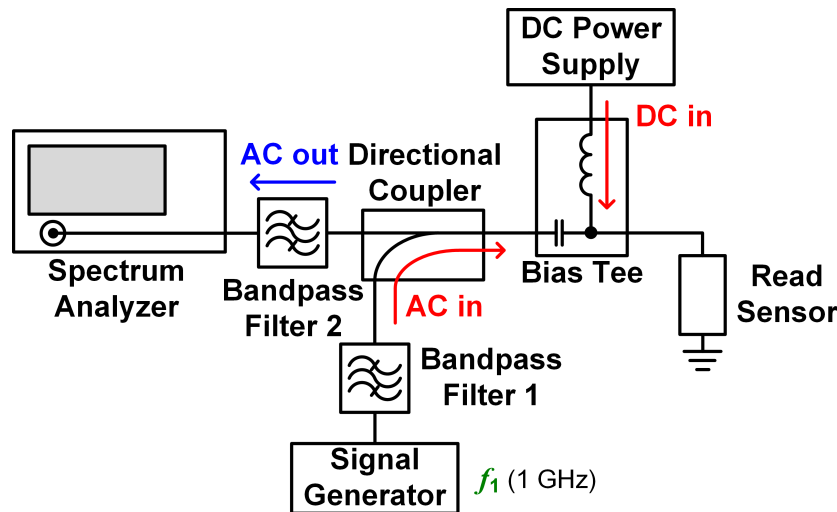


Fig. 32. Measurement setup allowing direct higher-order harmonic measurement

The signal generator itself is nonlinear, which means it will also generate higher-order harmonics. We use the bandpass filter (marked as “Bandpass Filter 1”) tuned to f_1 to filter out all undesired higher-order harmonics from the measurement. The DC power supply provides DC bias for the nonlinear device under test (DUT). A signal reflected from the device carries not only the fundamental but also higher-order harmonics, which

⁽¹³⁾The results of this section are published in part in [85].

are generated due to the sensor's nonlinear characteristics. Finally, the other bandpass filter (marked as "Bandpass Filter 2") filters the sought after harmonic ($2f_1$ or $3f_1$).

Let us derive a simple nonlinear system's response to a typical sinusoidal input [86]:

$$x(t) = A \cos(\omega t + \theta(t)). \quad (92)$$

This nonlinear system is a nonlinear operator that can be represented as a low-degree polynomial:

$$y_{\text{NL}}(t) = S_{\text{NL}}[x(t)] = a_1 x(t - \tau_1) + a_2 x^2(t - \tau_2) + a_3 x^3(t - \tau_3) + \dots \quad (93)$$

or

$$y_{\text{NL}}(t) = \underbrace{a_1 A \cos(\omega t + \theta(t - \tau_1) - \phi_1)}_{\text{linear response}} + \underbrace{a_2 A^2 \cos^2(\omega t + \theta(t - \tau_2) - \phi_2) + a_3 A^3 \cos^3(\omega t + \theta(t - \tau_3) - \phi_3)}_{\text{nonlinear response}} + \dots \quad (94)$$

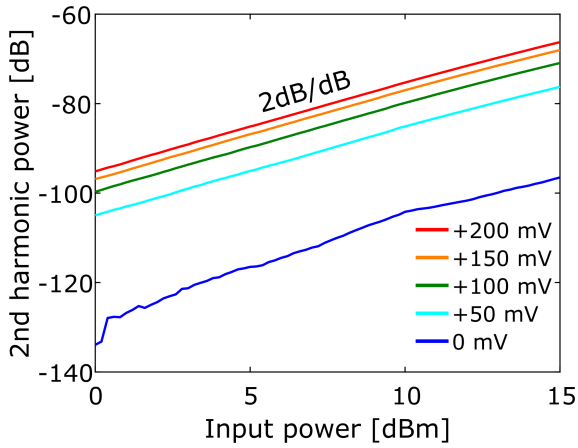
Expanding Eq. (94) using trigonometric identities,

$$y_{\text{NL}}(t) = \underbrace{\frac{1}{2} a_2 A^2}_{\text{DC}} + \underbrace{a_1 A \cos(\omega t + \theta(t - \tau_1) - \phi_1) + \frac{3}{4} a_3 A^3 \cos(\omega t + \theta(t - \tau_3) - \phi_3)}_{\text{fundamental}} + \underbrace{\frac{1}{2} a_2 A^2 \cos(2\omega t + 2\theta(t - \tau_2) - 2\phi_2)}_{\text{2nd harmonic}} + \underbrace{\frac{1}{4} a_3 A^3 \cos(3\omega t + 3\theta(t - \tau_3) - 3\phi_3)}_{\text{3rd harmonic}} + \dots \quad (95)$$

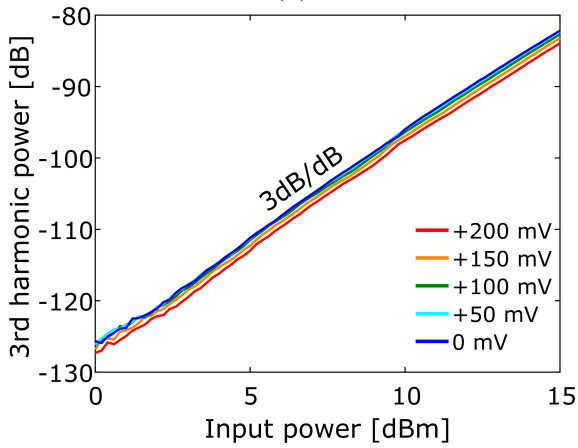
Equation (95) demonstrates that nonlinear systems qualitatively modify signal spectra as shown in Fig. 30c. It also defines harmonic power levels in terms of the input power: in case of simple *static* nonlinearity [Eq. (93)], doubling of the input power multiplies the output power of the second harmonic by 4 (2^2) and multiplies the output power of the third harmonic by 8 (2^3). Thus, the expected asymptotic slope of the second harmonic is 2 dB/dB while that of the third harmonic is 3 dB/dB [89].

If we now observe the sensor's power slopes measured at different biasing conditions and compare them to the ones of the permalloy resistor, there is an obvious difference—the

sensor's are *bias-dependent*. Specifically, the third harmonic power slopes change from 3 dB/dB to 4 dB/dB while for the permalloy resistor they are *bias-independent*. In Figs. 33 and 34, the true power level at the RF probe is approximately 20 dB less due to transmission losses and -16 dB at the coupled port of the directional coupler.

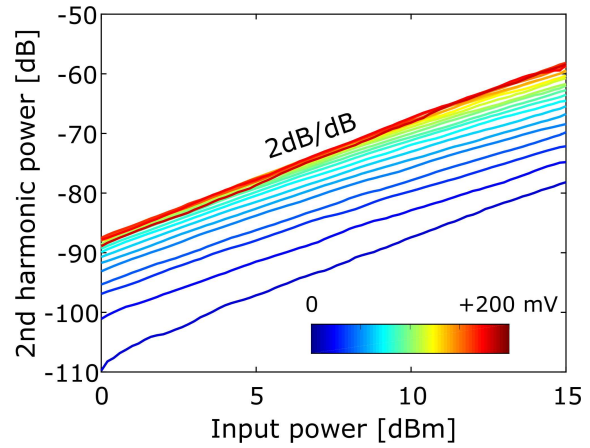


(a)

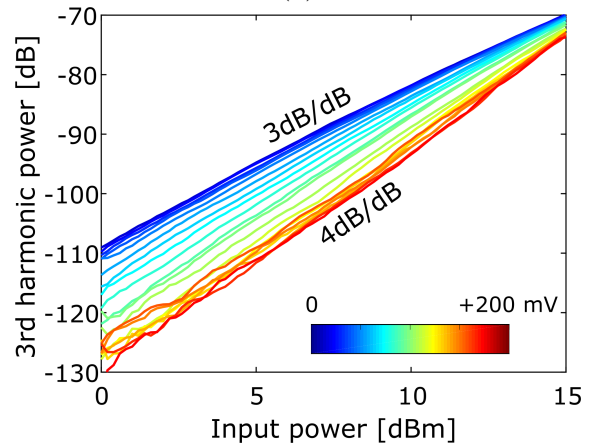


(b)

Fig. 33. Permalloy resistor's *DC bias-independent* power slopes of the second (a) and third (b) harmonics



(a)



(b)

Fig. 34. MTJ's *DC bias-dependent* power slopes of the second (a) and third (b) harmonics

The permalloy resistor is a bulk magnetic material, which exhibits nonlinear characteristics due to the heating effect. It is magnetic and therefore also subject to magnetization fluctuations. The read sensor design, however, is much more complicated than that of a simple permalloy stripe. Thus, the complex physical interactions (*e.g.*, magnetodipolar, ST, TMR) within these sensors could lead to the observed unexpected bias-dependence of their power slopes on the input power.

5.2.2 Two-tone measurement

In microwave engineering, the two-tone measurement is used to characterize *dynamic* nonlinear effects, also known as “memory effects.” If these effects are present in a device, its instantaneous output depends not only on the instantaneous input but also on *past values* of the input and/or output signal [86, 87, 90, 91].

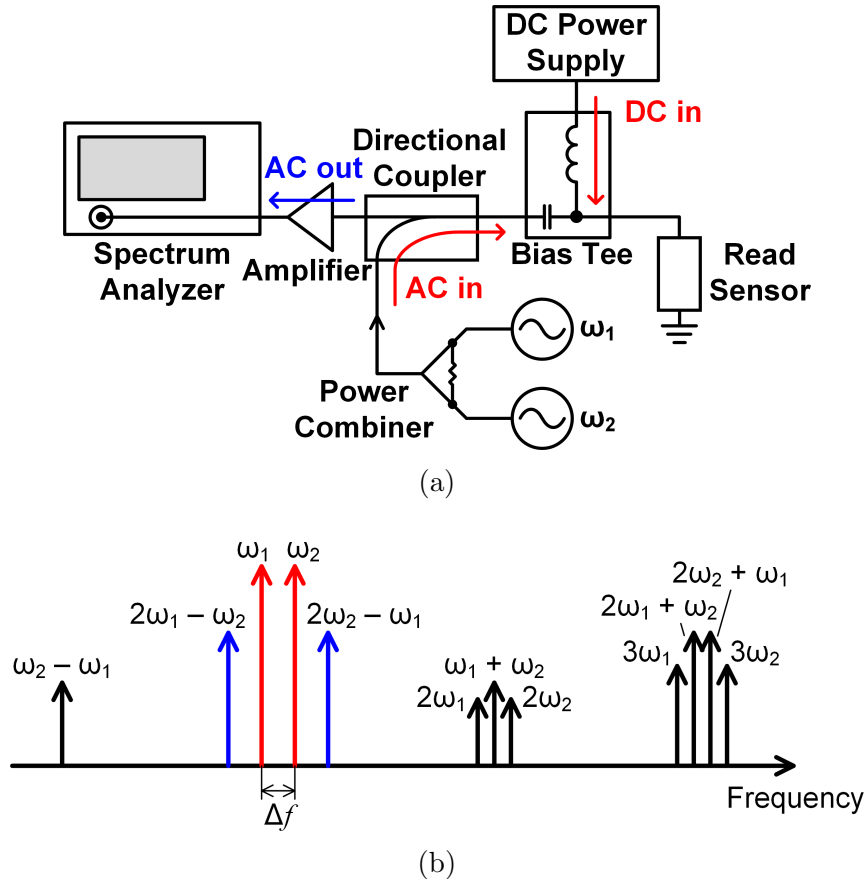


Fig. 35. (a) Two-tone measurement system. (b) IM products generated by a two-tone signal applied to a nonlinear DUT.

As shown in Fig. 35a, the two-tone measurement setup generally utilizes two signal generators, a power combiner, and a spectrum analyzer [86]. When two tones are applied to a nonlinear device, it generates higher-order inter-modulation (IM) products (Fig. 35b and Table 1) [88]. Lower and upper inter-modulation products of the third order (IM3), $2\omega_1 - \omega_2$ and $2\omega_2 - \omega_1$, are of the most interest as they produce signal components whose frequencies are close to the excitation frequencies. In case of *static* nonlinearity, these products’ amplitudes are symmetric and independent of the tone spacing Δf (highlighted rows in Table 1). On the contrary, *dynamic* nonlinearity (or memory effects) manifests as amplitude or phase deviations in IM responses with the tone spacing Δf . Note that the IM distortion (appearance of IM products caused by nonlinearities) itself is not a memory effect, but any variations in IM products with tone spacing can be regarded as one [91].

Frequency component	Output amplitude
ω_1	$a_1 A_1$
ω_2	$a_1 A_2$
$2\omega_1$	$\frac{1}{2} a_2 A_1^2$
$2\omega_2$	$\frac{1}{2} a_2 A_2^2$
$\omega_2 - \omega_1$	$a_2 A_1 A_2$
$\omega_1 + \omega_2$	$a_2 A_1 A_2$
$3\omega_1$	$\frac{1}{4} a_3 A_1^3$
$3\omega_2$	$\frac{1}{4} a_3 A_2^3$
$2\omega_1 - \omega_2$	$\frac{3}{4} a_3 A_1^2 A_2$
$2\omega_2 - \omega_1$	$\frac{3}{4} a_3 A_1 A_2^2$
$2\omega_1 + \omega_2$	$\frac{3}{4} a_3 A_1^2 A_2$
$2\omega_2 + \omega_1$	$\frac{3}{4} a_3 A_1 A_2^2$

Table 1: IM products (up to the third order) arising from a two-tone excitation with amplitudes A_1 and A_2 .

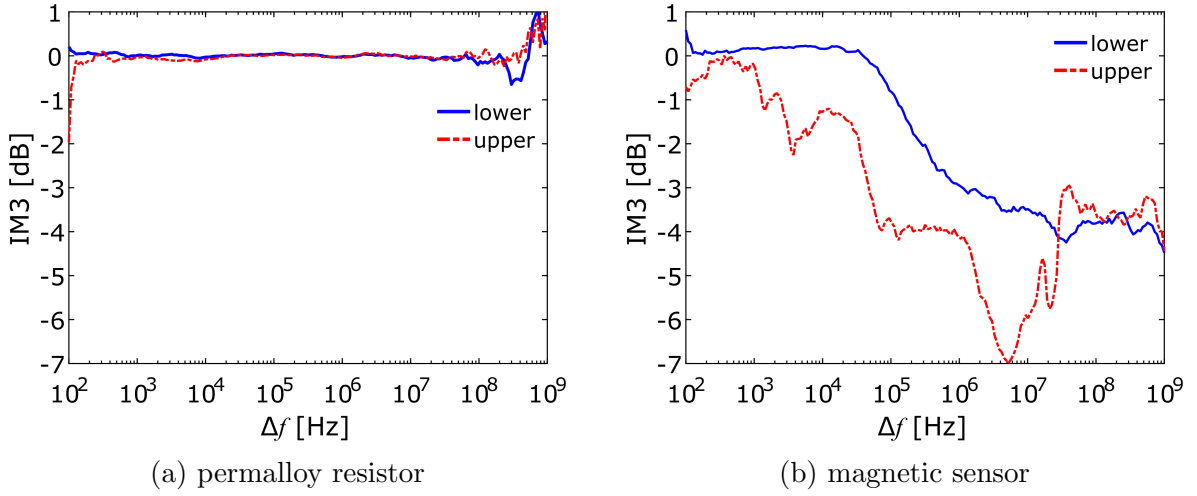


Fig. 36. (a) IM3's insensitivity to Δf indicates the presence of *static* nonlinear effects. (b) IM3 asymmetry indicates the presence of *dynamic* nonlinear effects. In this experiment, f_1 was set to 5 GHz while $f_2 = f_1 + \Delta f$. Both signal generators' power levels are 0 dBm, and the DUTs are biased at +50 mV.

If we now observe these IM products produced by both the permalloy resistor and magnetic sensor for a wide range of tone spacings Δf , they are stunningly different (Fig. 36). Similarly to Section 5.2.1, this observation, again, indicates that the sensor exhibits certain dynamic nonlinear effects that are not typical to all magnetic devices.

5.3 Probing nonlinear magnetization dynamics with a nonlinear vector network analyzer⁽¹⁴⁾

The *linear* vector network analyzer (VNA) and steady-state DC readout (Sections 4.1 and 5.1, respectively) measurement techniques allow analysis only of the input impedance and DC response. Since nonlinear effects are involved, a thorough nonlinear harmonic analysis is highly desired. The one- and two-tone characterization protocols described in Section 5.2 are tailored to nonlinear measurements in the presence of dynamic effects. These, however, do not account for the broadband nature of the gigahertz-range FMR in nanoelements, such as read heads.

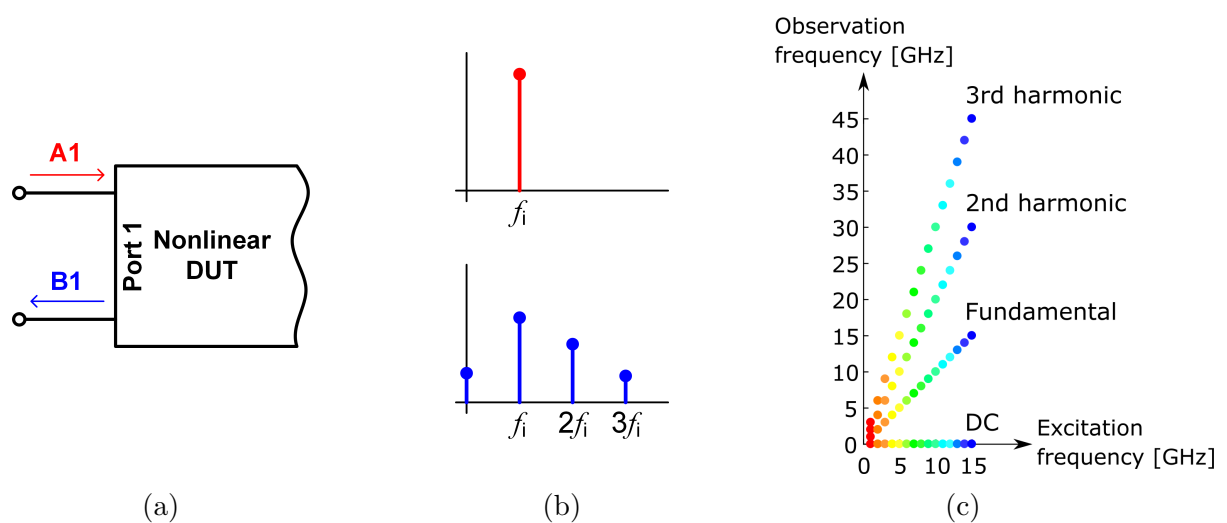


Fig. 37. Nonlinear vector network analyzer (NVNA) measures the incident and reflected waves' (A_1 and B_1 , respectively) magnitudes and phases (a) at the excitation frequency and at harmonic components (b) to which energy may be transferred due to the DUT's nonlinear characteristics. (c) shows the corresponding excitation and observation frequencies.

A comprehensive nonlinear analysis can be accomplished using a nonlinear vector network analyzer (NVNA) [94]. Since the characterized magnetic read sensors are one-port devices, this analysis is limited to the one-port scenario. In contrast to the VNA, which measures the magnitude ratio and phase difference between the incident and reflected waves (A_1 and B_1 , respectively) only at the excitation frequency, the NVNA measures the actual A_1 and B_1 waves' magnitudes and phases at the excitation frequency as well as harmonic components to which energy may be transferred due to the device's nonlinear characteristics (Fig. 37) [95, 96].

In this measurement, the excitation frequency f_i of the incident wave A_1 was swept from 1 to 15 GHz. At each frequency, the fundamental of the reflected wave B_1 was measured

⁽¹⁴⁾The results of this work are presented in part at [92] and published in [93].

at f_i . Naturally, the second harmonic of the reflected wave B_1 was measured at $2f_i$ (2 to 30 GHz) and the third harmonic was measured at $3f_i$ (3 to 45 GHz). We emphasize that in contrast to the measurements presented in, *e.g.*, Sections 3.1 and 4.2, the resultant curves represent the [DC or harmonic] frequency response, not the power spectra. A power spectrum is the distribution with frequency of the power content of the signal [69], whereas the frequency response [70] curves in Figs. 39 to 41 represent the magnitude of the corresponding harmonic component of B_1 as a function of the excitation frequency and are linearly proportional to voltage.

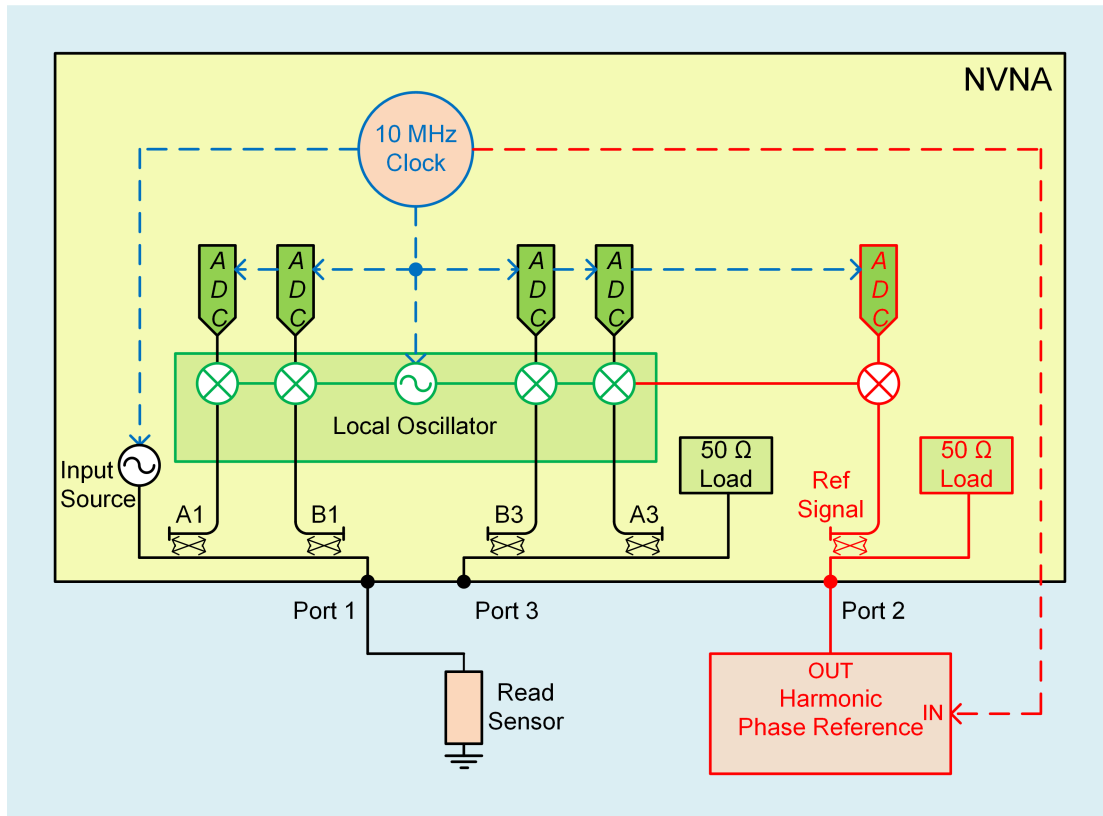


Fig. 38. Simplified block schematic of an NVNA based on the heterodyne principle

The NVNA is based on the heterodyne principle, which involves mixers for the down-conversion process (Fig. 38). As mentioned above, it measures one frequency component at a time. Consequently, each spectral line measured by the NVNA needs to be down-converted, *i.e.*, transferred from the high frequency to the intermediate frequency (IF). Then, all spectral lines must be correctly “stitched together,” especially with respect to the phase. A VNA is the basis for the NVNA. In the *linear* regime, the NVNA measurements collapse to the S-parameters. A DUT can be excited at one or both ports (*i.e.*, 1- versus 2-port measurements). All four waves (A_1 , B_1 , A_3 , and B_3) are measured through couplers and down-converted using mixers, which are all driven by the same Local Oscillator signal. Harmonic Phase Reference generates the reference signal to control the phase relationship between the different harmonic components. The 10 MHz clock insures

a constant phase relationship between the different harmonic components of the phase reference signal over time. After down-conversion by the mixers, the measured signals are digitized. The resultant data can be represented in the time or frequency domain:

$$\begin{aligned} B_k^{(pk)} &= \frac{2}{T} \int_0^T b(t) e^{-jk\omega t} dt, \\ b(t) &= \text{Re} \left(\sum_{k=1}^N B_k^{(pk)} e^{jk\omega t} \right), \end{aligned} \quad (96)$$

where $\omega = 2\pi/T$ and $B_k^{(pk)}$ is the peak value for each harmonic k [97].

Using the NVNA, we characterized six samples coming from two different wafers. We measured each sample's response under various experimental conditions: AC power and DC bias (Figs. 39 and 40). We also experimentally determined the maximum tolerable signal levels that can be used for the excitation of magnetization dynamics: 350 μA DC bias current and -5 dBm (corresponds to 335.2 μA root-mean-square current⁽¹⁵⁾) AC power.

In Figs. 31b and 39a, the DC response revealed the FL mode at ≈ 7.2 GHz⁽¹⁶⁾ as well as peaks located below the device's natural FL FMR frequency. These peaks, in turn, produced the second and third harmonics of B_1 : Figs. 39c, 39d, 40c and 40d.

For a selected experimental condition (-5 dBm AC power level and $+250$ μA DC bias current), we counterposed the resultant fundamental, second, and third harmonics of B_1 to the DC readout curve, all plotted *versus* the excitation frequency. In Fig. 41a, the ripply response at the fundamental of B_1 might understandably be mistaken for measurement noise. In Figs. 41b and 41c, in turn, the second and third harmonics of B_1 indicate *distinct* peaks at multiples of the FL FMR mode's fractional frequencies corresponding to $1/2$, $1/4$, and $1/6$ frequency of the FL. On the contrary, the FL mode and the peak located at $1/3$ the frequency of the FL *do not* produce their second and third harmonics⁽¹⁷⁾. The NVNA measurements imply that the read sensor's nonlinear characteristics give rise to nonlinear oscillations under the AC excitation signal with the frequency considerably lower than, but still an integer ratio of, the FL mode (*i.e.*, $f_{\text{exc}} = f_{\text{FL}}/n$, where $n \in \mathbb{N}$). Naturally, this also produces a measurable DC contribution corresponding to this excitation frequency.

⁽¹⁵⁾Refer to Table 2 in Appendix D for dBm to root-mean-square (RMS) current conversion details.

⁽¹⁶⁾This number is consistent with the thermal noise ferromagnetic resonance (T-FMR) and ΔNL measurements presented in Figs. 12 and 26.

⁽¹⁷⁾Refer to Fig. C.1 in Appendix C. There, the FL FMR mode and the peak located at $1/3$ the frequency of the FL did generate the second harmonic of B_1 .

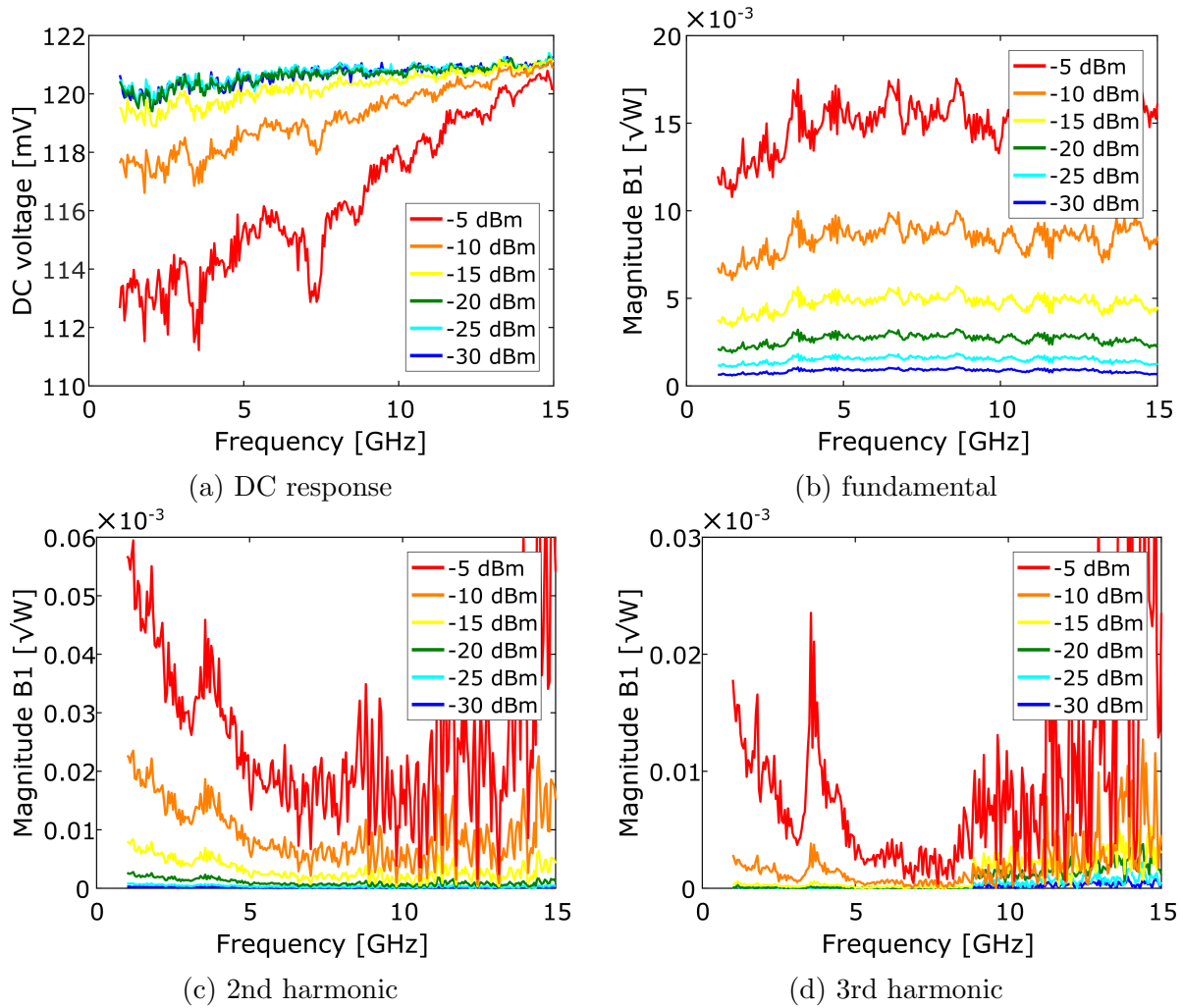


Fig. 39. NVNA measurements obtained with a Keysight N5247A at $+250 \mu\text{A}$ DC bias current and 15 Hz intermediate frequency bandwidth (IFBW) for different AC power levels. (a) DC response, (b) fundamental, (c) second, and (d) third harmonics of B_1 are plotted *versus* the excitation frequency. Positive DC bias corresponds to the electron flow from the PL to FL.

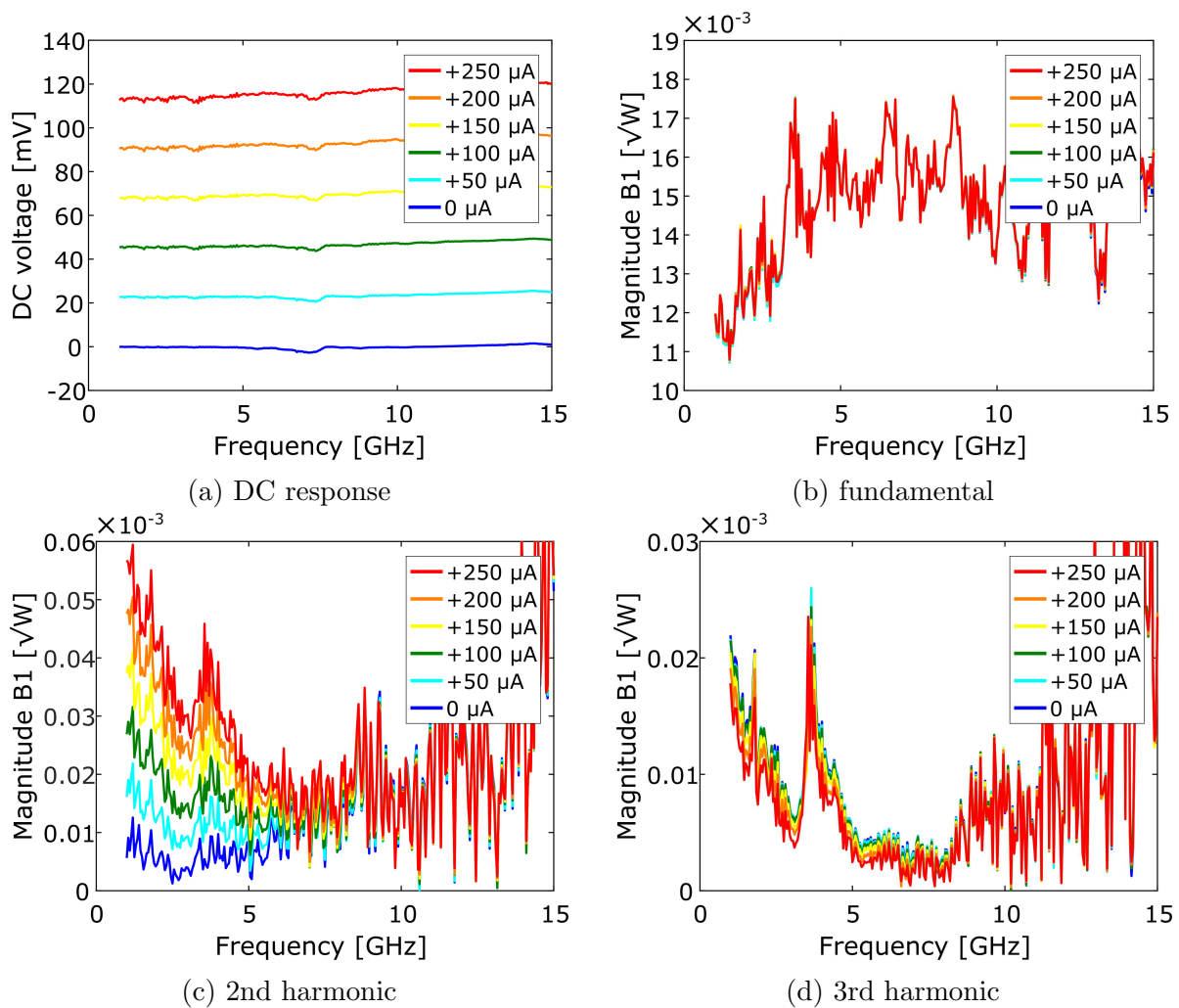


Fig. 40. NVNA measurements obtained at -5 dBm AC power and 15 Hz IFBW for different DC bias currents. (a) DC response, (b) fundamental, (c) second, and (d) third harmonics of B_1 are plotted *versus* the excitation frequency.

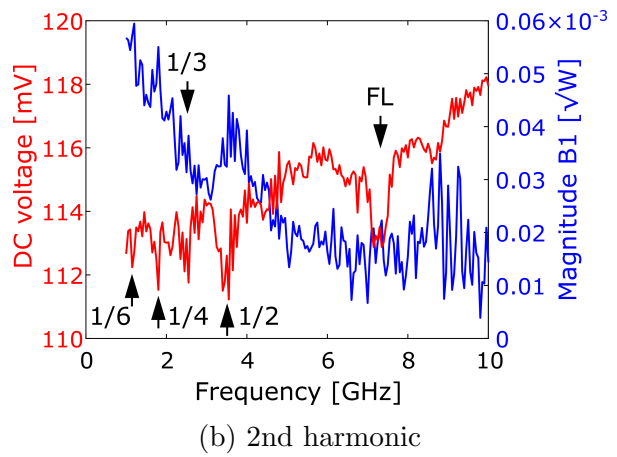
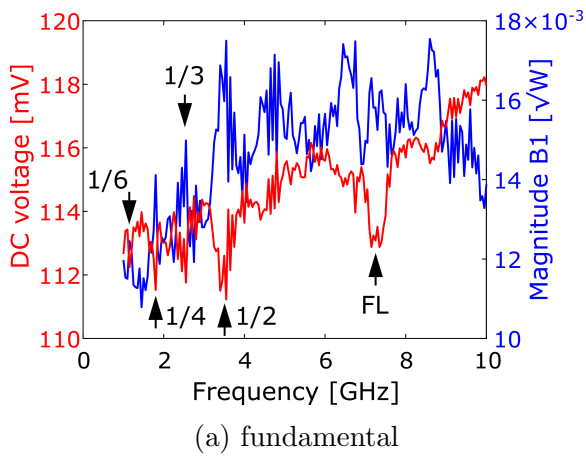
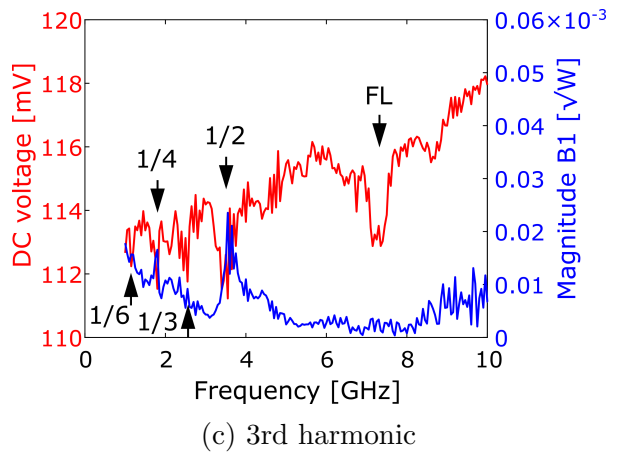


Fig. 41. (a) fundamental, (b) second, and (c) third harmonic response at *fractional frequencies* of the FL mode plotted *versus* the excitation frequency. The sample is characterized at $+250 \mu\text{A}$ DC bias current, -5 dBm AC power, and 15 Hz IFBW.



5.4 Summary

In this chapter, we applied the characterization protocols tailored to nonlinear measurements in the presence of dynamic effects. As these effects occur in the gigahertz range (*i.e.*, ferromagnetic resonance in read sensors), their characterization greatly benefited from advances in microwave measurement techniques. We started with the one- and two-tone measurements, which indicated that nonlinear magnetization dynamics do not behave as expected in the presence of static nonlinear effects. Then, a comprehensive nonlinear analysis of magnetic read sensors was accomplished using an NVNA. The NVNA measurements demonstrated that all characterized magnetic read sensors' DC responses contain peaks at frequencies that are the integer fractions (1/2, 1/3, 1/4, and 1/6) of the devices' natural FL FMR frequency. These peaks, in turn, produce the second and third harmonics of the reflected wave B_1 . The subsequent chapter elaborates on the underlying physics that enabled the DC response at fractional frequencies of the FL mode and the corresponding harmonics.

6 Micromagnetic simulations of strongly nonlinear magnetization dynamics⁽¹⁸⁾

Magnetic tunnel junction (MTJ)-based magnetic sensors are nonlinear dynamic systems. As was mentioned in Section 2.2, room-temperature thermal fluctuations result in random magnetization dynamics of both the free and pinned layers (FL and PL, respectively), which can be quantified by their ferromagnetic resonance (FMR) modes [13]. Another source of magnetization dynamics in MTJs is the spin-torque (ST) effect, which describes a direct transfer of angular momentum from the spin-polarized electrons to the local magnetization [98]. In Section 5, we emphasized that magnetization dynamics are inherently nonlinear because magnetization oscillations arise from the precession of the magnetization vector with a constant magnitude, leading to the following nonlinear relation of the magnetization components: $m_x^2 + m_y^2 + m_z^2 = 1$ [75]. ST-induced magnetization dynamics result in a large-angle magnetization precession where the nonlinear nature of magnetization dynamics becomes especially pronounced.

The fundamental theory of nonlinear oscillations states that their nonlinearity results in new resonances such that oscillations of frequency close to f_0 (intrinsic frequency) can be excited by an external force of frequency considerably different from f_0 . A resonant condition might occur at every excitation frequency pf_0/q , where p and q are positive integers. In practice, however, p and q should be small because the resonance strength rapidly decreases with increasing order of nonlinearity [99].

Bearing this fundamental theory in mind, this chapter presents the identification of the new resonances at fractional frequencies of the FL FMR mode resulting from the nonlinearity of the ST-induced magnetization dynamics.

6.1 Modeling methodology

All numerical simulations presented in this chapter were performed using the micromagnetic software [MicroMagus](#), which solves the modified Landau-Lifshitz-Gilbert (LLG) equation for the magnetization \mathbf{M} :

$$\frac{d\mathbf{M}}{dt} = -\gamma_0 \mathbf{M} \times \mathbf{H} + \frac{\alpha}{M_s} \mathbf{M} \times \frac{d\mathbf{M}}{dt} - \gamma_0 f_J(\theta) \mathbf{M} \times (\mathbf{M} \times \mathbf{p}), \quad (97)$$

where α is the Gilbert damping and γ_0 is the absolute value of the gyromagnetic ratio.

⁽¹⁸⁾The results of this section are published in part in [93].

Equation (97) accounts for the ST effect using the standard Slonczewski formalism [recall Eq. (31)], which introduces an additional torque term to the equation of motion in the Gilbert form [76, 100].

The dimensionless ST amplitude f_J [equal to a_J in Eqs. (31) and (85)] depends on the angle θ between the magnetization \mathbf{M} and the spin-polarization direction \mathbf{p} as follows [76, 77] ⁽¹⁹⁾:

$$f_J(\theta) = a_J \frac{2\Lambda^2}{(\Lambda^2 + 1) + (\Lambda^2 - 1) \cos \theta}, \quad (98)$$

where

$$a_J = \frac{\hbar}{2|e|} \frac{jP}{M_s^2 d}. \quad (99)$$

In Eqs. (98) and (99), e is the electron charge, j is the electric current density, and d is the thickness of the magnetic layer subjected to ST. When the asymmetry parameter $\Lambda = 1$, the ST effect is assumed to be symmetric. P is the degree of spin polarization of the electrical current.

In the LLG equation, thermal effects are accounted for by an additional term \mathbf{H}_{th} describing random fluctuations induced by the interaction of the ferromagnet with the thermal bath [Eq. (28)]. Unless stated otherwise, all micromagnetic simulations in the subsequent sections are performed at $T = 0$ K.

The tunnel magnetoresistance (TMR) response introduced in Section 2.3 is the qualitative description of the TMR's dependence on the angle θ defined between the adjacent layers' magnetizations [Eq. (73)].

6.2 Modeling considerations

In this study, the MgO-based MTJ devices' PL1/PL2 and FL are of a similar CoFe/CoFeB alloy (Fig. 9a). The intrinsic Gilbert dampings of the FL and PL2 are 0.01. The IrMn-exchange-pinned damping of the PL1 was initially assumed to be an order of magnitude larger, 0.1 [101]. The interlayer couplings are similar to those used in [102]: 0.04 erg/cm² between the FL and PL2, -1.6 erg/cm² between the PL1 and PL2⁽²⁰⁾.

⁽¹⁹⁾To describe the ST's angular dependence in MgO-based junctions, we used the common formulations for metallic junctions. Recent work (Ref. [78]) shows that the effective difference in angular dependence for these two scenarios is insignificant.

⁽²⁰⁾where 1 erg/cm² = 10⁻³ J/m²

For each experimental frequency point at a given AC power level and DC bias, we had to perform an independent time-domain micromagnetic simulation. As discussed in Section 5, the reason is that nonlinear systems produce a response not only at the excitation frequency but also at its multiples (*i.e.*, harmonics). As for linear systems that respond only at the excitation frequency, fast broadband excitation can be accomplished *via* sine pulses or multifrequency signals (*e.g.*, Schroeder-phased harmonic signals) that are optimal for uniform excitation of all system modes [103, 104]. To enable faster frequency sweeps around the ranges of interest (*i.e.*, FL FMR frequency and its fractional ratios), the following simplifications to the original read sensor design were adopted⁽²¹⁾: 1) The antiferromagnetic (AFM) layer was excluded from simulations, but its effect on the PL1 was taken into account by the corresponding exchange bias field of 1000 Oe⁽²²⁾ [102]. 2) The left and right Side Bias magnets were also excluded from simulations. Instead, the Side Bias demagnetizing field was calculated in the quasi-static solver and then included as an external field in all subsequent dynamic simulations.

To the best of our knowledge, there have not been any comprehensive micromagnetic studies on the nonlinear magnetization dynamics used to predict the DC-biased MTJ's harmonic response to an AC excitation signal. In general, these dynamics and, by extension, its harmonic response should be sensitive to the various magnetic and ST parameters described above. To test this, we excited the read sensor model *via* a combination of AC and DC signals (as in the experiment in Fig. 41) at 1/4 the frequency of the FL FMR mode (see Appendix E for more detail).

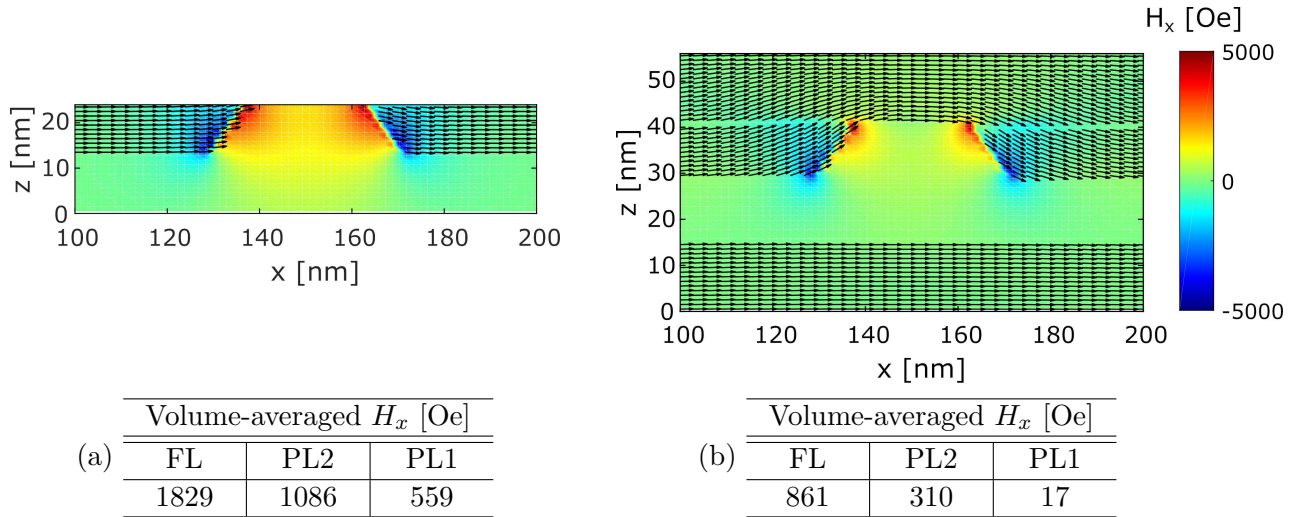


Fig. 42. Simulated Side Bias field (a) without and (b) with the presence of magnetic shields

⁽²¹⁾With these simplifications, it requires ≈ 1 hour to collect 60 nsec of magnetization dynamics at 0 K for a magnetic system consisting of 1920 discretization cells. As for 300 K, it takes ≈ 15 hours to simulate 200 nsec.

⁽²²⁾where $1 \text{ Oe} = 10^3 / (4\pi) \text{ A/m}$

Effect of the Side Bias and magnetic shielding. The read sensor model in Fig. 9a is shown without the magnetic shields. In a real sensor (Fig. 7), the top and bottom magnetic shields isolate the sensor from adjacent bits and large writer fields. Material parameters of both shields are typical of permalloy. We micromagnetically modelled their effect on the field from the Side Bias, and the simulation results are shown in Fig. 42. In the presence of magnetic shields, the simulated Side Bias field, especially onto the pinned layers PL2/PL1, sufficiently decreased. The Side Bias field onto the FL, however, also decreased. This would significantly shift the FL FMR mode towards lower frequencies. Unfortunately, based on the limited information about the shields provided by the MTJ samples manufacturer, we cannot explain such low Side Bias field onto the FL.

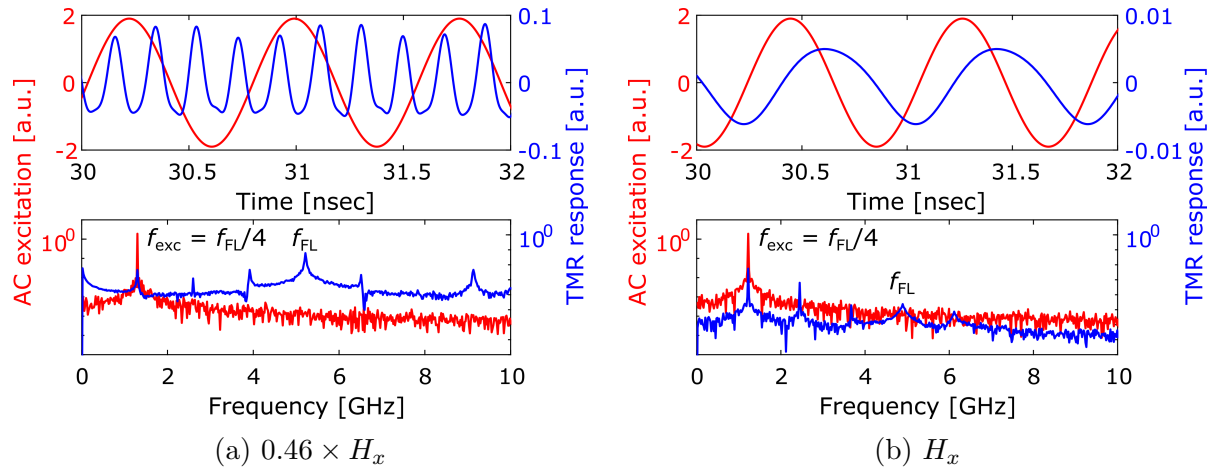


Fig. 43. Time- (top) and frequency-domain (bottom) responses of the read sensor model excited at 1/4 the frequency of the FL FMR mode. Lower Side Bias field onto PL2/PL1 (a) evokes strongly nonlinear magnetization oscillations accompanied by stronger harmonic response than in (b).

Lower Side Bias field onto the FL and PL2/PL1 makes the magnetic system less stiff and more likely to evoke strongly nonlinear magnetization oscillations (Figs. 43 and 44). While the Side Bias field onto the FL cannot be too low (based on the FL FMR frequency), the Side Bias field onto the PL2/PL1 is a subject of concern. Variations in the spacing between the Side Bias and the stack within the prescribed fabrication tolerances may affect the Side Bias field strength. Moreover, the Side Bias magnetization is known to be accurate at least within $\pm 10\%$. These factors introduce uncertainty in our estimation of the Side Bias field.

Effect of damping. The pinned layer PL1 damping significantly affects the read sensor's dynamics (Fig. 45). A lower damping constant corresponds to lower power absorption by the magnetic system consequently leading to nonlinear oscillations with a larger amplitude and, by extension, a stronger harmonic response. While 0.01–0.02 is a typical damping constant for the FL and PL2 [105], the pinned layer PL1 damping was assumed to be much higher, 0.1 [101]. Smith *et al.* studied current-perpendicular-to-plane giant-

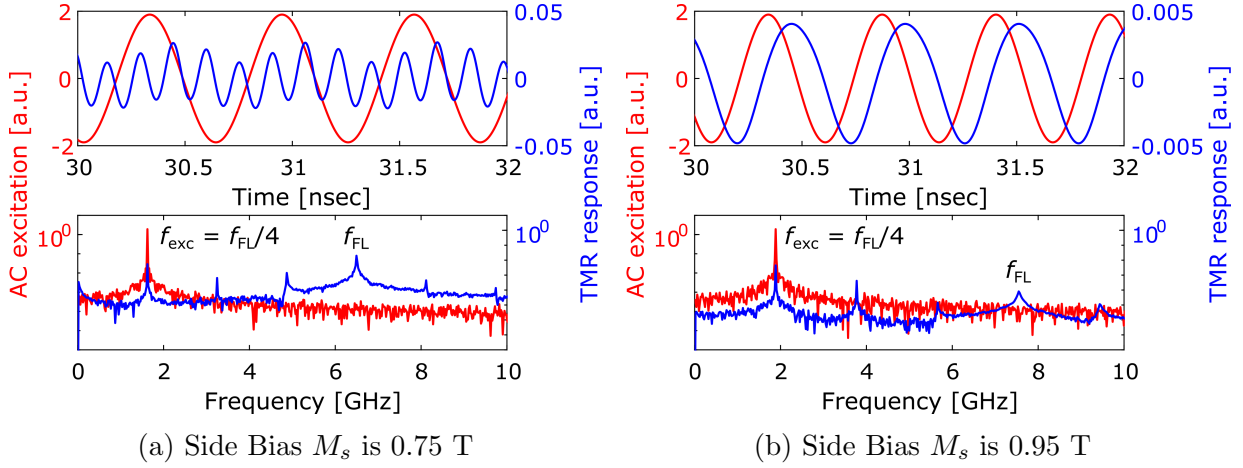


Fig. 44. Time- (top) and frequency-domain (bottom) responses of the read sensor model excited at 1/4 the frequency of the FL FMR mode. Lower Side Bias magnetization (a) evokes strongly nonlinear magnetization oscillations accompanied by stronger harmonic response than in (b).

magneto-resistive (CPP-GMR) spin-valve stacks. Their samples, being just a PL coupled to an AFM, did not have a PL2/PL1 with Ru in between. Nevertheless, the authors made a convincing case that the PL1 should have such a high damping and suggested two mechanisms that can explain a $\sim 10\times$ increase in the PL damping: 1) PL-FL spin-pumping and 2) strong interfacial exchange coupling at the IrMn/PL interface. In a subsequent study [106], Mohammadi *et. al.* reported an inverse-thickness-squared dependence of damping for exchange-biased CoFe layers and increased damping (but still lower than 0.1 for a 3-nm-thick CoFe layer) *via* spin-pumping. Our main argument is that if the PL1 damping is set to 0.1, then the absence of any measurable DC contribution at a fractional frequency contradicts our experimental observations. Thus, it is legitimate to assume that the PL1 damping constant can be lower than 0.1.

Effect of the ST parameters. The ST parameters appear naturally in the derivation of Slonczewski's approximation for asymmetric ferromagnetic/non-ferromagnetic/ferromagnetic multilayers [107]. Experiments and theory have provided estimated values for both P and Λ [77, 108, 109]. Because of the uncertainty in both parameters, $P = 0.35$ and $\Lambda = 1.5$ are only first estimates.

Effect of the interaction between the FL and PL2. The PL2 is not thick enough to neglect the ST effect on this layer. In fact, it is even thinner than the FL (3 nm *versus* 7 nm, respectively). Thus, the FL-PL2 coupling must be considered in any full treatment of magnetization dynamics in the read head system. To account for this interaction, the direction of the electron polarization used to compute the ST acting on the FL must be adjusted based on the magnetization direction of the PL2, and vice versa. Moreover, the magnetodipolar interaction between the FL and PL2 causes positive feedback, which

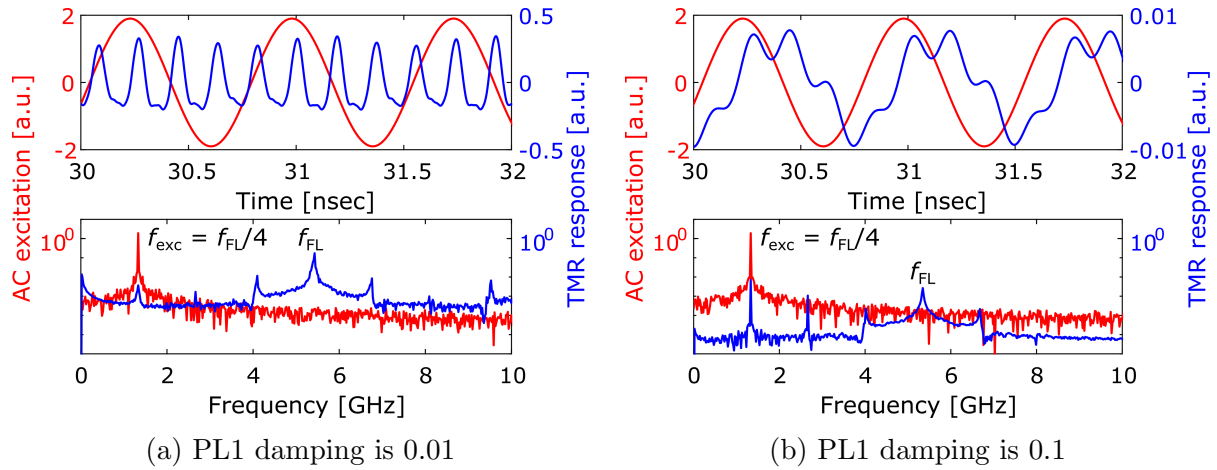


Fig. 45. Time- (top) and frequency-domain (bottom) responses of the read sensor model excited at 1/4 the frequency of the FL FMR mode. Lower pinned layer PL1 damping (a) evokes strongly nonlinear magnetization oscillations accompanied by stronger harmonic response than in (b).

qualitatively affects the system dynamics. This feedback can be thought of as follows. The deviation of the FL magnetization from its preferred orientation generates a stray field. This field causes the PL2 magnetization to deviate in the direction opposite to that of the FL. This, in turn, results in an even larger deviation of the FL magnetization due to the influence of the PL2 stray field, thus producing positive feedback between the magnetization dynamics of the FL and PL2 [110].

6.3 Results and discussion

6.3.1 DC response

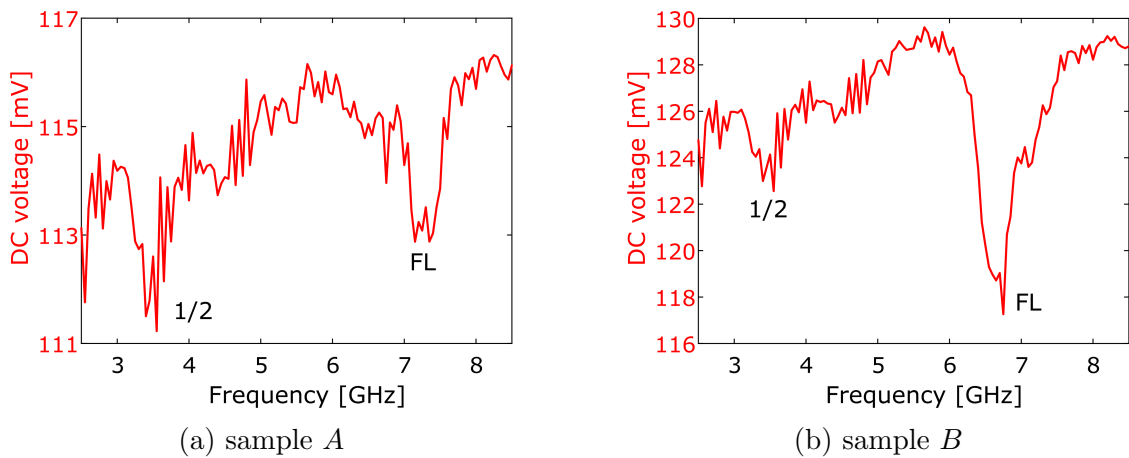


Fig. 46. Quantitatively different experimental DC responses: (a) sample *A*'s nonlinear vector network analyzer (NVNA) measurements are presented in Fig. 41; (b) sample *B*'s NVNA measurements are shown in Appendix C, Fig. C.1

To aid the reader, in Fig. 46 we show the experimental DC responses limited to the frequency range from $1/2$ the frequency of the FL FMR mode to the FL FMR mode. Most characterized samples' DC responses looked similar to that of sample *A*. Contrary to sample *A*, sample *B*'s DC response at the FL FMR frequency is much more pronounced, which may be associated with the FL FMR mode and its “sub-harmonic” located at $1/3$ the frequency of the FL having generated the second harmonic of B_1 (Appendix C, Fig. C.1). This implies a much stronger nonlinear response and occurred for only one sample out of six from the same wafer.

Effect of the ST parameters. The uncertainty in the ST parameters gave us the freedom necessary to achieve sufficient qualitative agreement between the experimental and simulated DC responses. The characteristic “foldover” FL FMR profiles evolve with increasing spin polarization factors P and asymmetry parameters Λ (Fig. 47). Moreover, higher P and Λ significantly broaden the FL mode's linewidth. We estimated our samples' ST parameters by matching the FL mode's linewidths in the experimental and simulated DC responses. The ~ 0.5 GHz experimental linewidth corresponds to $P = 0.4$ and $\Lambda = 4$.

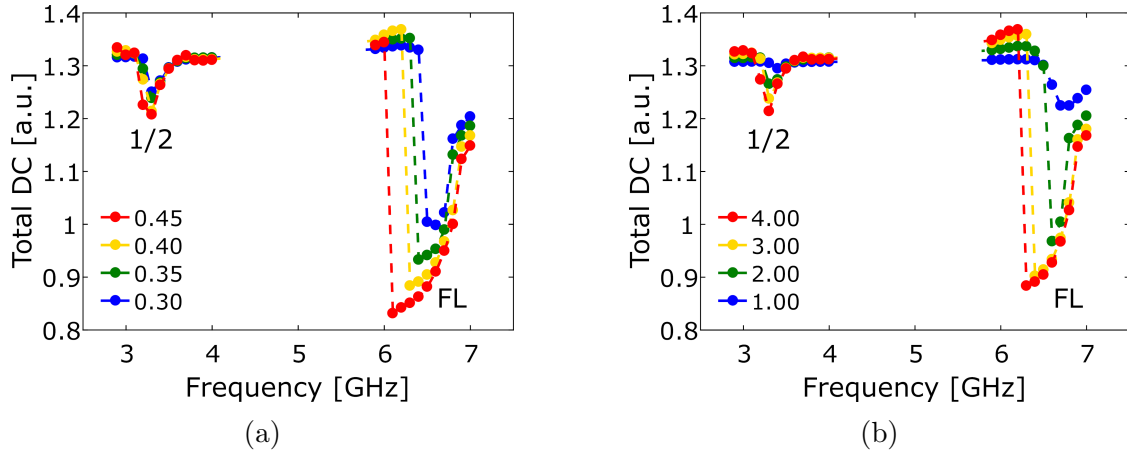


Fig. 47. Simulated DC responses for different (a) spin polarization factors P at $\Lambda = 4$ and (b) asymmetry parameters Λ at $P = 0.4$ plotted *versus* the excitation frequency. The corresponding “constant” and “oscillating” contributions to the total DC responses are shown in Appendix F (Figs. F.1 and F.2).

When excited around a fractional frequency of the FL mode, increasing ST parameters facilitate the strongly nonlinear magnetization dynamics accompanied by the generation of the higher-order harmonics and measurable DC (*e.g.*, as in Fig. 45a). The two contributions to the total DC response contain additional physical insights. Figures F.1 and F.2 in Appendix F show that the DC response at the FL FMR frequency is primarily determined by mixing of the TMR oscillations with the excitation signal [“oscillating” term in Eq. (91)]. On the other hand, the DC response at $1/2$ the frequency of the FL FMR mode is defined by the “constant” term.

Effect of the Side Bias field. As discussed in Section 6.2, there is some uncertainty in our

estimation of the Side Bias field. On one hand, the Side Bias field onto the FL cannot be too low as it would not match the experimental frequency of the FL mode. On the other hand, the Side Bias field onto the pinned layers PL2/PL1 cannot be too high as it would not facilitate the strongly nonlinear magnetization dynamics accompanied by the generation of the higher-order harmonics and measurable DC response. We discovered that the $\times 0.2$ reduction in the estimated Side Bias field onto the PL2/PL1 along $\times 1.7$ increase in the estimated Side Bias field onto the FL satisfy both criteria. Moreover, the proposed adjustments to the Side Bias field shifted the magnetic system’s dynamic regime from quasi-chaotic towards pure phase-locking when excited at a fractional frequency. On one hand, quasi-chaotic regime results in stronger DC response; on the other hand, it is achievable only within a narrow range of the system’s magnetic and ST parameters. Therefore, we conclude that the strength of the non-homogeneous Side Bias field on the system’s magnetization dynamics is a compromise between the FL’s stability and pinned layers’ stiffness.

Effect of the mutual ST between the FL and PL2. In Section 6.2, we suggested that the PL2 might not be thick enough to ignore the ST effect on this layer. Figure 48a supports this supposition: the accounted ST effect on the PL2 contributes to the ST response at $1/2$ the FL frequency. This effect is especially pronounced in the “constant” term (Fig. F.3a in Appendix F).

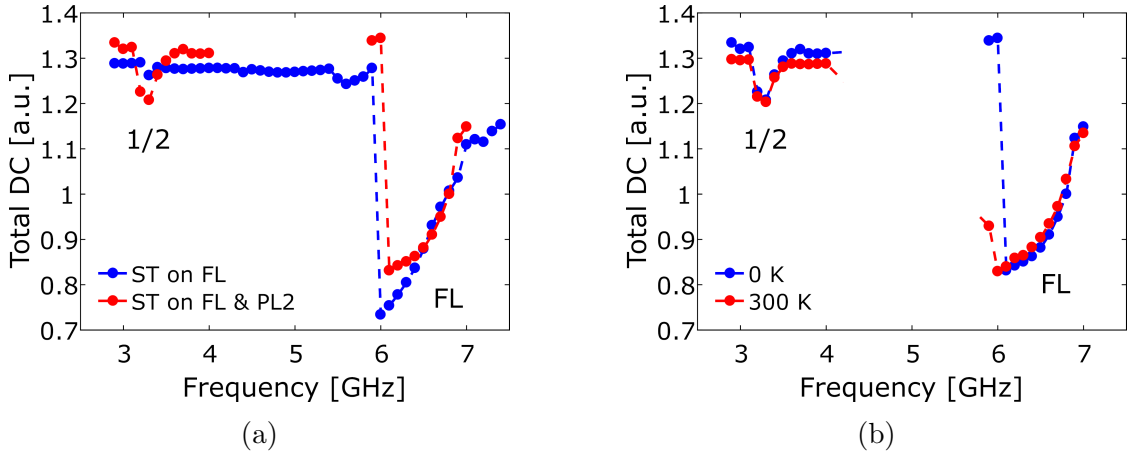


Fig. 48. (a) Simulated DC responses ($\Lambda = 4$, $P = 0.45$) emphasizing the importance of the ST effect not only on the FL but also on the PL2. The corresponding “constant” and “oscillating” contributions to the total DC responses are shown in Appendix F (Fig. F.3). (b) Simulated DC response for $\Lambda = 4$, $P = 0.45$, and different temperature conditions.

Stability of the dynamic regime. Nonlinear dynamic systems are prone to chaotic behavior [111]. For example, in our model we achieved a quasi-chaotic regime when the Side Bias field onto the FL was too low. To verify that our calibrated reader model’s phase-locking regime was stable with respect to thermal fluctuations, we performed a temperature experiment.

Figure 48b shows that room-temperature fluctuations did not disturb the phase-locking regime and resulted only in insignificant changes in the simulated DC responses at 0 and 300 K. Interestingly, in the presence of thermal fluctuations, both peaks’ “linewidths” broadened only insignificantly. This feature, once again, emphasizes the difference between the frequency response and the power spectrum. In the latter case, spectral lines tend to significantly broaden in the presence of thermal noise.

Response at the FL mode’s “sub-harmonics.” The FL precession exhibits an elliptical trajectory. Thus, the m_x component moves back and forth twice during one oscillation cycle, and its oscillation frequency is approximately twice that of the m_y component [112]. Therefore, if f_{FL} is the FL’s resonant precession frequency, then $f(m_x) = 2f(m_y) = 2f_{FL}$. In this physical scenario, the magnetodipolar feedback introduced in Section 6.1 has the following effect. The magnetodipolar interaction induces coupling between the FL and PL2. Due to the large y -component of the FL’s stray field induced by strong m_y oscillations with the frequency f_{FL} , the above-mentioned coupling induces the m_y oscillations of the PL2 with the same frequency f_{FL} . These oscillations, in turn, result in the m_x oscillations of the PL2 with the frequency $1/2f_{FL}$. The feedback *via* the PL2’s magnetodipolar field leads to the oscillation of the FL with the frequency $1/2f_{FL}$ as well as all its harmonics. Thus, the FL power spectrum would contain the FL mode, its “sub-harmonic” at $1/2f_{FL}$ the frequency of the FL mode, and their higher-order modes, all of which are produced due to the nonlinear nature of the FL’s m_y oscillations and the contribution of the PL2’s m_x and m_y oscillations excited by the presence of the magnetodipolar interaction.

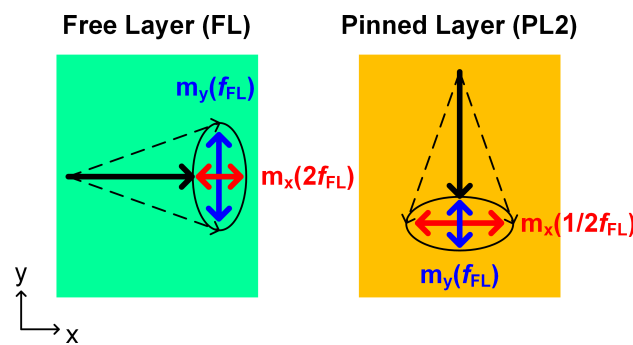


Fig. 49. Magnetization precession’s elliptical trajectory and magnetodipolar feedback between the FL and PL2 facilitate the response at $1/2$ the FL frequency.

To facilitate the DC response at $1/2$, $1/3$, $1/4$, and $1/6$ the frequency of the FL FMR mode, it is enough to combine the magnetodipolar feedback between the FL and PL2 with a low-order nonlinearity. The DC response at $1/5$ the frequency of the FL FMR mode is not present in the measurement: it requires a fifth-order nonlinearity, but the fifth harmonic is usually too small to evoke phase locking.

6.3.2 Harmonic response

Figure 50 shows the fundamental and second harmonic of TMR counterposed to the total DC response. Whereas the TMR response at $1/2$ the FL FMR frequency has a weak fundamental and a strong second harmonic, the TMR response at the FL FMR frequency has a strong fundamental and a weak second harmonic.

The former observation implies that the MTJ's nonlinear characteristics give rise to nonlinear oscillations under the AC excitation signal with the frequency corresponding to $1/2$ the FL natural precession frequency. As the TMR response at the second harmonic is stronger than at the fundamental, the FL FMR mode seems to phase lock to this harmonic. As for the latter observation, the FL FMR mode phase locks to the TMR oscillations at the excitation frequency, thus producing a strong fundamental at the FL FMR frequency.

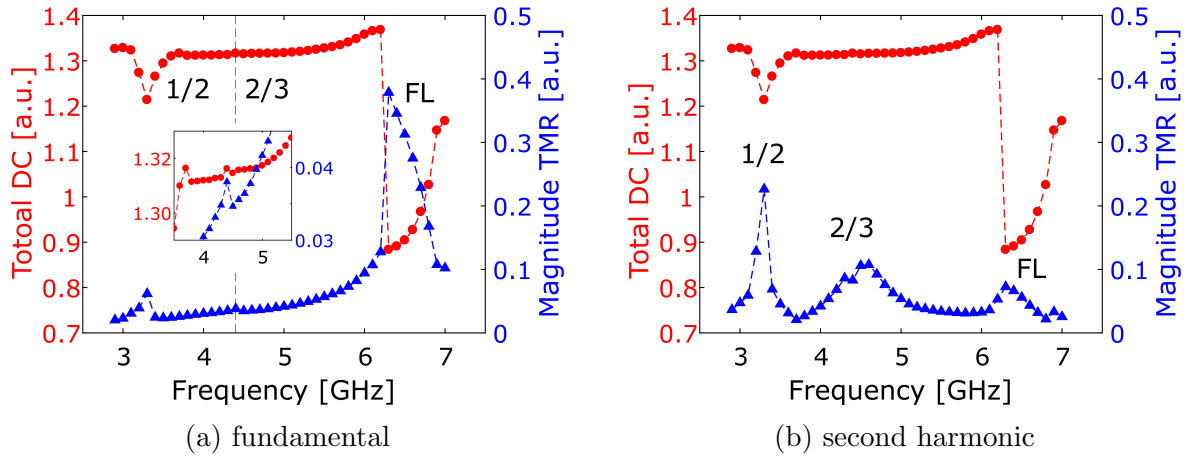


Fig. 50. Simulated TMR response at the (a) excitation frequency (fundamental) and (b) its second harmonic plotted *versus* the excitation frequency for $\Lambda = 4$ and $P = 0.4$.

The major discrepancy between the measurements in Figs. 41a and 41b and simulations in Fig. 50 is the absence of the strong fundamental of B_1 at the FL FMR frequency. We attribute this difference to weak coupling (due to convergence to steady-state phase locking) between the NVNA's incident wave and magnetization precession. We suggest that the experimental magnetization precession has a less stable phase relation with the NVNA's incident signal than in the model.

In Fig. 41a, the ripply response in the fundamental of B_1 suggests that there are more peaks at fractional frequencies of the FL mode than what we have identified. In particular, the enlarged DC responses in Fig. 46 indicate a resonant feature between $1/2$ the FL FMR mode and the FL FMR mode. We qualitatively replicated this feature in the simulated TMR response [Fig. 50a (inset) and Fig. 50b]. Contrary to the experiment, however, the FL FMR mode seems to phase lock to the second harmonic, not to the

TMR oscillations at the excitation frequency corresponding to $2/3$ the FL FMR frequency. This is clearly seen in the time- and frequency-domain TMR responses for two selected excitation frequencies: $2/3$ the frequency of the FL FMR mode and 5 GHz (Fig. 51). The magnetic system's harmonic response (specifically, of the second harmonic) is stronger if the excitation frequency corresponds to a fractional frequency of the FL FMR mode.

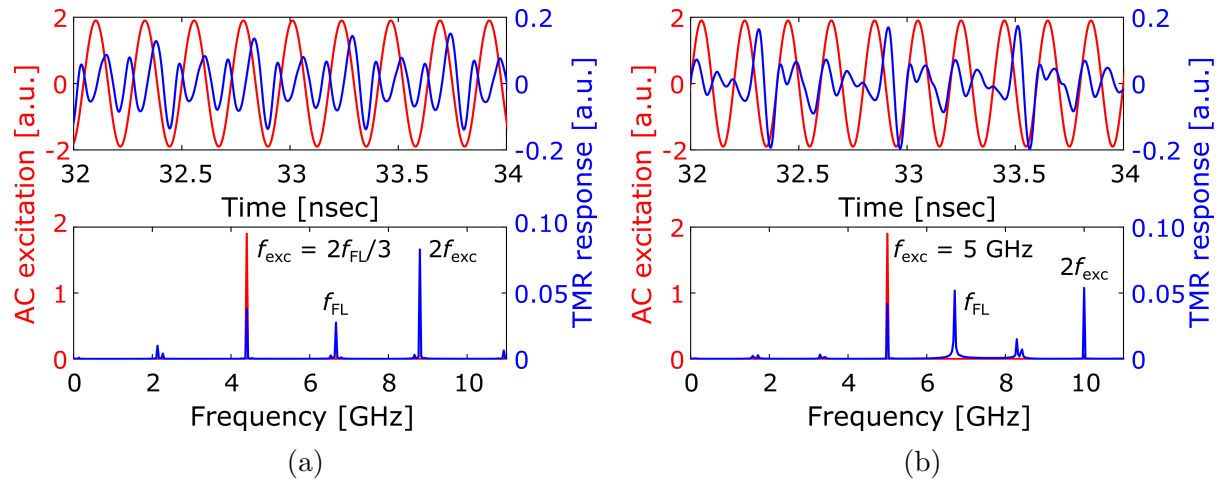


Fig. 51. Time- (top) and frequency-domain (bottom) responses of the read sensor model excited at (a) $2/3$ the frequency of the FL FMR mode and (b) 5 GHz. These frequency points are chosen from the simulations presented in Fig. 50.

6.4 Summary

In the previous chapter, we discovered that all characterized magnetic sensors' DC responses reveal peaks at frequencies that are the integer fractions ($1/2$, $1/3$, $1/4$, and $1/6$) of the devices' natural FL FMR frequency. These peaks, in turn, generate the corresponding second and third harmonics of B_1 .

In this chapter, we employed micromagnetic modeling to understand the underlying physics that enabled the DC response at “sub-harmonics” of the FL mode. A comprehensive micromagnetic study suggested that the experimentally observed DC response at $1/2$, $1/3$, $1/4$, and $1/6$ the frequency of the FL mode can be defined by a low-order nonlinearity and strong magnetodipolar feedback between the FL and PL. As the PL is significantly thinner than the FL, additionally accounting for the ST effect on this layer notably enhanced the ST-driven harmonic response. Interestingly, the orthogonality of the FL and PL also facilitated the magnetic sensors' response at $1/2$ the FL FMR frequency.

7 Conclusion

In this thesis, we first elaborated on advances in electrical characterization of magnetization dynamics—*via* ferromagnetic resonance (FMR)—in multilayers. The selected measurement techniques (spectrum analysis, waveform analysis, and vector network analysis) were then applied to the MgO-based magnetic tunnel junctions (MTJs) embedded in the read sensor path.

The inherent nonlinear nature of magnetization dynamics made it necessary to go beyond the established measurement techniques for electrical characterization of FMR. Advanced nonlinear microwave measurement techniques (*e.g.*, one- and two-tone measurements, nonlinear vector network analysis) proved to be suitable for full treatment of MTJs' nonlinear effects in conjunction with dynamic ones. Additionally, we demonstrated that, by means of measuring the noise floor around the AC carrier, FMR characterization relying on coupling between the AC excitation and magnetization dynamics can be tailored to account for the absence of the stable phase relation between these two signals.

A substantial body of our work focused on the identification of the new resonances at fractional frequencies of the free layer (FL) FMR mode resulting from the nonlinear nature of the spin-torque (ST)-induced magnetization dynamics. A complimentary micromagnetic study showed that the experimentally observed DC response at frequencies that are the integer fractions of the FL's resonant precession frequency can be defined by a low-order nonlinearity and strong magnetodipolar feedback between the magnetic layers adjacent to an MgO barrier. Additionally, the harmonic response is enhanced by the mutual ST effect between these layers. We determined that the MTJ-based read sensors' nonlinear magnetization dynamics and, by extension, their harmonic response are sensitive to various magnetic and ST parameters. Our study demonstrated that a comprehensive synthesis of nonlinear measurements and modeling can clarify the uncertainty in the definition of these parameters.

Most importantly, as magnetic nanodevices continue to shrink in size, the inherent nonlinear nature of magnetization dynamics becomes especially pronounced and can serve as a basis for new applications, such as frequency multipliers that use sub-harmonic injection locking and broadband rectifiers based on ST rectification phenomena.

A Noise reduction *via* spectral subtraction and signal filtering in the frequency domain

The signal processing procedure used to obtain the measurements in Section 3.2 includes: signal “de-noising” and signal filtering. De-noising emphasizes specific areas of the spectrum by lowering the noise level [113]. In this work, we de-noised the signal *via* spectral subtraction and signal filtering in the frequency domain (also known as “Fourier filtering”). The results in Fig. A.1 demonstrate much lower noise levels in the de-noised and filtered signal.

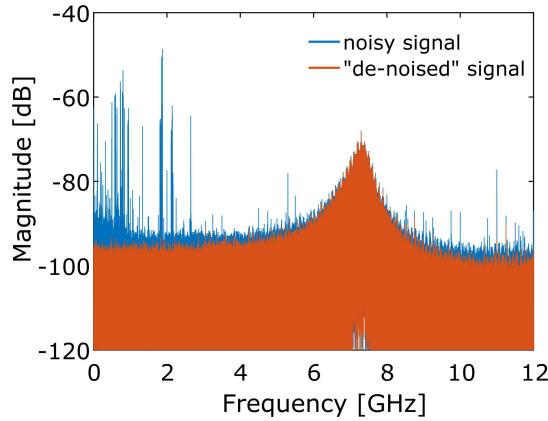


Fig. A.1. This signal processing procedure lowers the noise level while keeping the phase uncorrupted. Note that the real-time oscilloscope measurements presented in Section 3.2 did not utilize the AC excitation. So, the strong peaks below 3 GHz are telecommunication signals.

This signal processing solution is somewhat expensive computationally, thus rendering it ill-suited for real-time applications. Nevertheless, it has a tremendous advantage over other signal processing techniques: the signal parameters, especially the signal phase, remain uncorrupted.

Spectral subtraction is achieved by subtracting the estimated noise spectrum from the noisy signal spectrum. In case the noise is not measured separately, it is estimated and updated from the periods when the signal is absent. To restore the de-noised signal, the estimated noise spectrum is combined with the phase of the noisy signal and then transformed *via* the inverse Fourier transform into the time domain [62, 114].

Assuming that the noisy signal $y(t)$ is the sum of the signal $x(t)$ and the noise $n(t)$, its time- and frequency-domain representations are:

$$y(t) = x(t) + n(t) \quad (100)$$

and

$$|Y(f)|^2 = |X(f)|^2 + |N(f)|^2. \quad (101)$$

The de-noised power spectrum can be estimated by subtracting the noise power estimate from the noisy power spectrum:

$$|\hat{X}(f)|^2 = |Y(f)|^2 - |\hat{N}(f)|^2 = |Y(f)|^2 H_{ss}^2(f), \quad (102)$$

where the equivalent spectral subtraction filter's frequency response is equal to

$$H_{ss}^2(f) = 1 - \frac{1}{\text{SNR}(f)}, \quad (103)$$

and the frequency-dependent signal-to-noise ratio (SNR) is

$$\text{SNR}(f) = \frac{|Y(f)|^2}{|\hat{N}(f)|^2}. \quad (104)$$

For many applications, the spectral subtraction technique's weakest point is in estimating the noise power spectrum. For our application, the measured waveforms are obtained by the direct observation of the high-frequency magnetization dynamics of the free and pinned layers (FL and PL, respectively) under the DC bias. Therefore, the waveform measured at zero DC bias is the sought after noise $n(t)$.

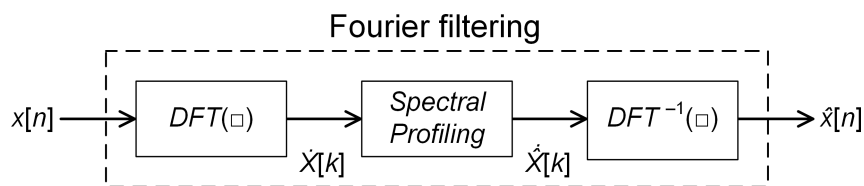


Fig. A.2. Fourier filtering removes unwanted signal features in the spectral domain

The Fourier filtering requires us to 1) compute the signal's Fourier transform, 2) multiply the Fourier transform bins by a given filter function (*i.e.*, spectral profiling), and 3) calculate the inverse Fourier transform of the result [115]. Special care must be taken when using both the amplitude and phase spectrum to reconstruct the filtered signal in the time domain. The critical moment is to adequately determine the cut-off frequencies allowing most of the noise to be eliminated while keeping the signal itself undistorted.

B Smith chart analysis: single resonant mode

In Section 4.1, we related the magnitude of the complex input impedance Z_{11} plotted as a function of frequency (Figs. 23a and 23b) to the imaginary part of the measured reflection coefficient S_{11} plotted *versus* its real part (Figs. 23c and 23d). Equation (72) connects the 50 Ω -referenced S_{11} and Z_{11} .

When the reflection coefficient S_{11} representing a single resonant mode is plotted in the complex plane (also known as ‘‘Smith chart’’), it forms a circle in canonical position with its center on the real axis (Fig. B.1a). This circle intersects the real axis at the location of the resonant frequency [116, 117]. In Figs. 23c and 23d, this point corresponds to the FL ferromagnetic resonance (FMR) mode.

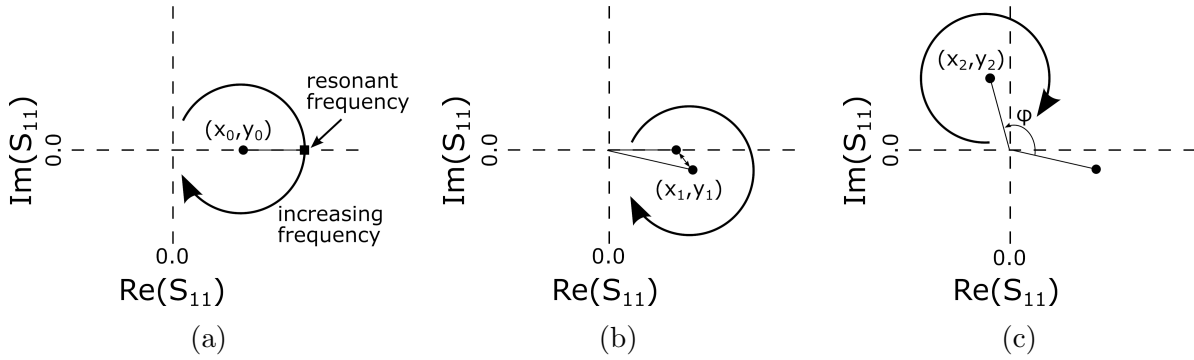


Fig. B.1. Exemplary real and imaginary parts of the complex reflection coefficient S_{11} for a single resonant mode. (b) and (c) show the offset and rotation of an ideal resonant circle (a).

Real measurement scenarios alter the ideal resonant circle’s position on the complex plane [116, 117]. Crosstalk between cables and/or coupling structures offset the circle away from its place on the real axis (Fig. B.1b). As our measurement setup has only one cable (Fig. 4), this kind of shift may occur, *e.g.*, due to imperfect de-embedding. A phase shift due to transmission lines connected to the device under test (DUT) causes the resonant circle to rotate around the origin (Fig. B.1c). In our measurement setup, the electrical length between the calibrated probe tip and the DUT is less than 1 mm. Such a short connection could not possibly produce a significant rotation of the resonant circle. So, the phase shift between the positive and negative V_{DC} scenarios (Figs. 23c and 23d) is a feature of the device, not a measurement artifact.

The complex translation and/or rotation of the ideal resonant circle can be expressed as $\tilde{S}_{11} = (S_{11} + X)e^{j\phi}$, where X is the complex constant offset, and ϕ is the phase shift [116, 117].

C Anomalous sample

Similar to the description in Section 5.3, the selected nonlinear vector network analyzer (NVNA) measurements in Fig. C.1 were obtained using the instrument in its standard configuration: we measured 3 harmonics (fundamental, second, and third) for each excitation frequency. Then, the resultant harmonics of B_1 were counterposed to the DC readout curve, all plotted *versus* the excitation frequency.

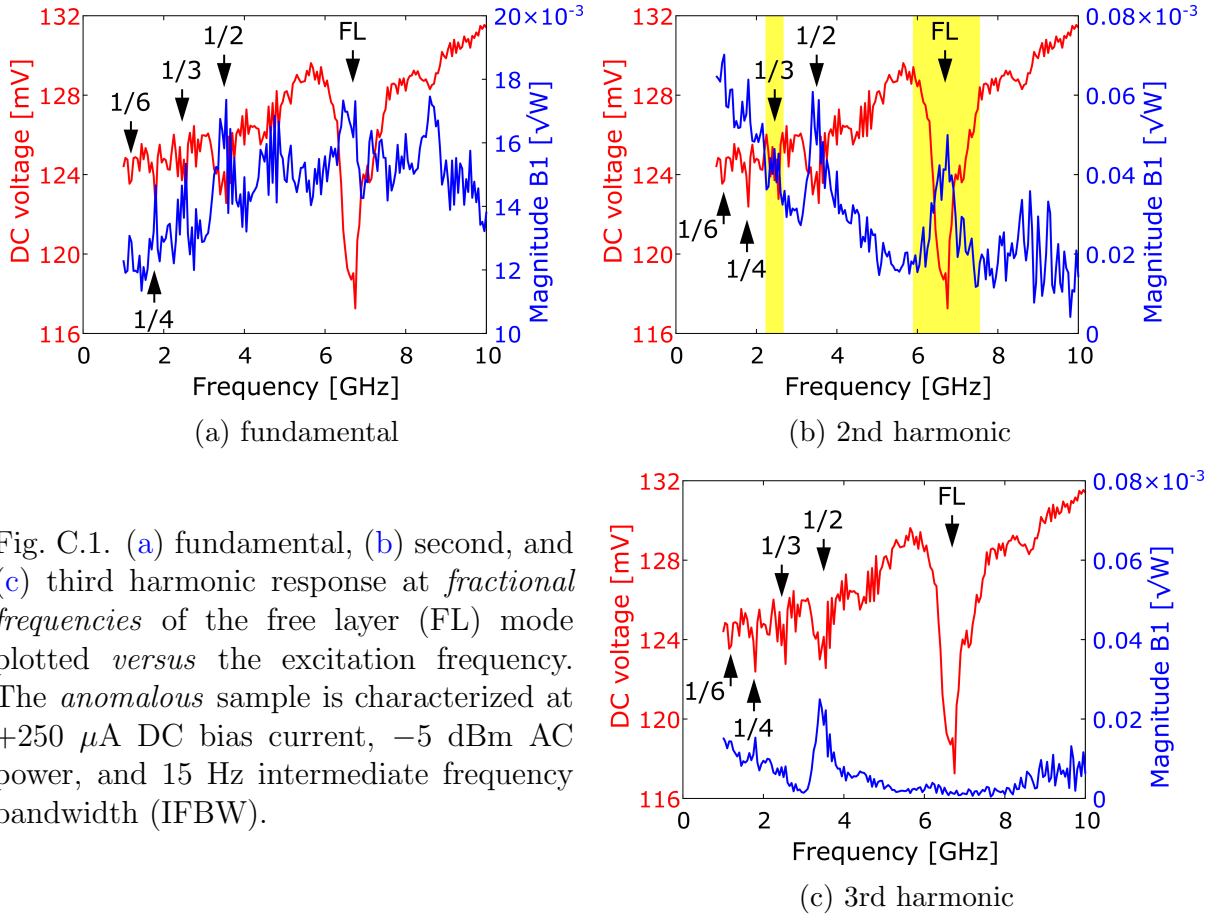


Fig. C.1. (a) fundamental, (b) second, and (c) third harmonic response at *fractional frequencies* of the free layer (FL) mode plotted *versus* the excitation frequency. The *anomalous* sample is characterized at $+250 \mu\text{A}$ DC bias current, -5 dBm AC power, and 15 Hz intermediate frequency bandwidth (IFBW).

In Fig. C.1b, the FL ferromagnetic resonance (FMR) mode and the peak located at $1/3$ the frequency of the FL generated the second harmonic of B_1 . Theoretically, we did not expect to see the harmonics of the magnetic read sensor's FL mode as they are caused by *non-homogeneous* magnetization oscillations [118]. Nevertheless, their presence may explain stronger DC response at the FL frequency for this anomalous sample.

D AC-power-to-current conversion

AC power supplied by the signal generator				
dBm	μA at 50- Ω	mV at 50- Ω	mV at open-circuit terminal	μA at 750- Ω TMR sensor
-5	2500	125.7	251.4	335.2
-10	1400	70.7	141.4	188.5
-15	795.3	39.8	79.6	106.1
-20	447.2	22.4	44.8	59.7
-25	251.5	12.6	25.2	33.6
-30	141.4	7.1	14.2	18.9

Table 2: AC-power-to-current conversion

dBm to root-mean-square (RMS) current conversion for the 50- Ω system is misleading (second column in Table 2):

$$\sqrt{\frac{10^{\text{dBm}/10}}{Z_0} \times 10^{-3}}, \quad (105)$$

where Z_0 is the 50- Ω system impedance [119].

To estimate more realistically AC current through the read sensor, the RMS voltage for the 50- Ω system is first calculated (third column in Table 2) [119]:

$$\sqrt{10^{\text{dBm}/10} \times Z_0 \times 10^{-3}}. \quad (106)$$

The system as a whole represents an open circuit (Fig. 8a). Thus, the value in the third column should be doubled to obtain the total voltage at the open end [120].

Finally, the AC current through the read sensor can be obtained for a given tunnel magnetoresistance (TMR) resistance (last column in Table 2).

E Effect of magnetic parameters on read sensor's dynamic regime

In Section 6.2, we presented the time- and frequency-domain responses of the read sensor model for selected magnetic parameters that effectively shift the magnetic system's dynamic regime from weakly to strongly nonlinear. In these micromagnetic studies, we fixed the spin-torque (ST) parameters: spin polarization P and ST asymmetry Λ are equal to 0.55 and 1, respectively. The AC and DC excitation signals match the experiment in Fig. 41. Then, we excited the system at 1/4 the frequency of the free layer (FL) ferromagnetic resonance (FMR) mode and observed the resultant harmonic response (Figs. E.1 to E.3) at the excitation frequency, $f_{\text{FL}}/4$, as well as at $f_{\text{FL}}/2$, $3f_{\text{FL}}/4$, and f_{FL} .

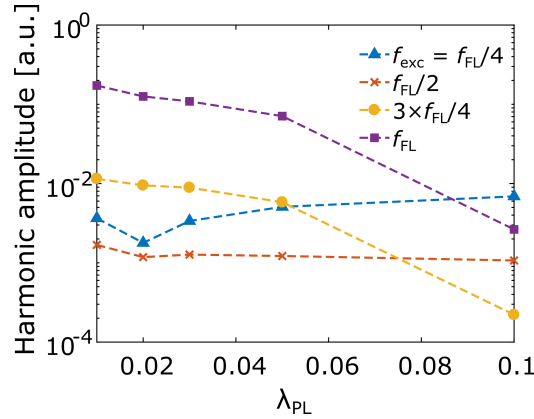


Fig. E.1. Effect of the pinned layers' damping constant

If the pinned layers' damping is lower than 0.1, the response at the fourth harmonic of the excitation frequency (which coincides with the FL frequency) becomes stronger than at the drive frequency. This threshold corresponds to the magnetization oscillations becoming strongly nonlinear as demonstrated in Fig. 45a.

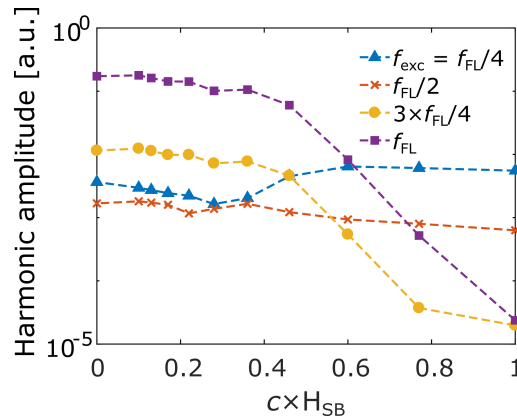


Fig. E.2. Effect of the Side Bias field on the pinned layers

Accompanied by the response at the fourth harmonic of the excitation frequency (which

coincides with the FL frequency) becoming stronger than at the drive frequency, the threshold below which we observe strongly nonlinear magnetization oscillations (Fig. 43a) corresponds to $0.6\times$ reduction in the Side Bias field onto the pinned layers.

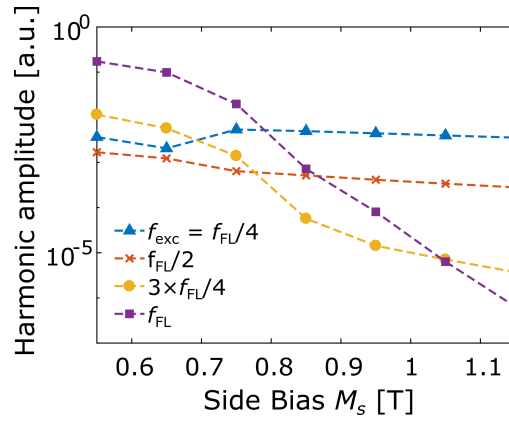


Fig. E.3. Effect of the Side Bias magnetization

Analogously, to shift the system's dynamic regime from weakly to strongly nonlinear (Fig. 44), it is enough to sufficiently lower (*i.e.*, less than 0.8 T) the Side Bias magnetization.

F Effect of spin-torque parameters on read sensor's DC response

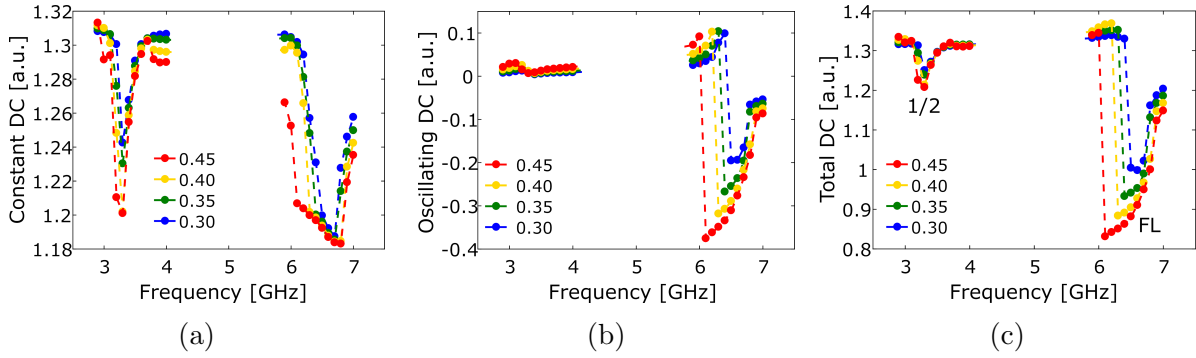


Fig. F.1. Simulated (a) “constant” and (b) “oscillating” contributions to the (c) total DC response for different spin polarization factors P at $\Lambda = 4$

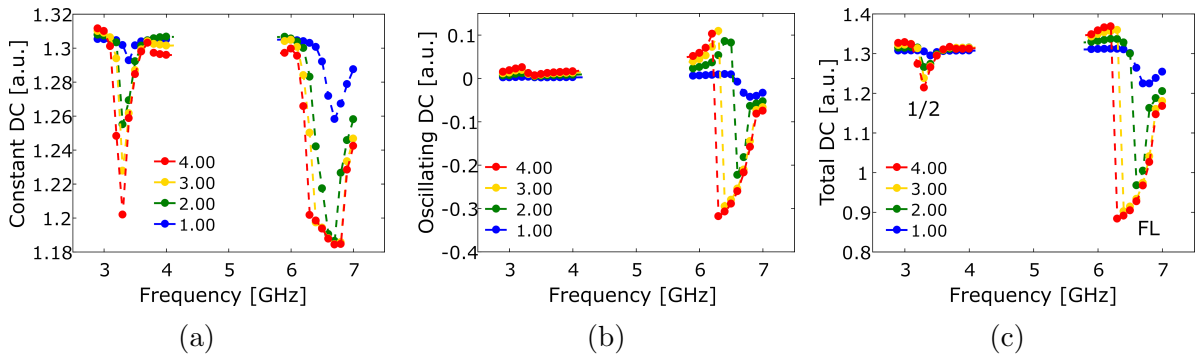


Fig. F.2. Simulated (a) “constant” and (b) “oscillating” contributions to the (c) total DC response for different asymmetry parameters Λ at $P = 0.4$

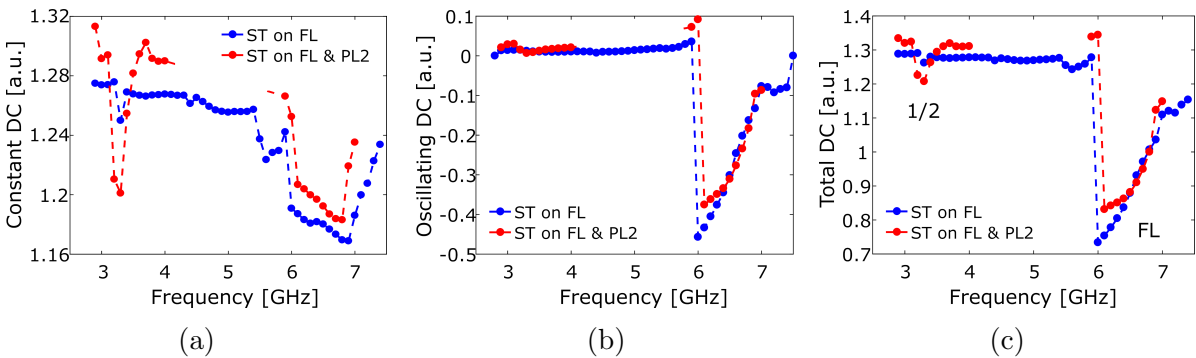


Fig. F.3. Simulated (a) “constant” and (b) “oscillating” contributions to the (c) total DC response for $\Lambda = 4$, $P = 0.45$, and different ST scenarios

References

- [1] G. Bertotti, I. Mayergoyz, and C. Serpico, *Nonlinear Magnetization Dynamics in Nanosystems*, ch. 2, pp. 21–34. Amsterdam: Elsevier Ltd., 2009.
- [2] J. E. Miltat and M. J. Donahue, “Numerical micromagnetics: Finite difference methods,” in *Handbook of Magnetism and Advanced Magnetic Materials* (H. Kronmüller and S. Parkin, eds.), vol. 2, pp. 1–23, Chichester: John Wiley & Sons Ltd., 2007.
- [3] D. Berkov, “Basic physical principles,” in *Magnetism in Medicine* (W. Andrä and H. Nowak, eds.), pp. 26–64, Weinheim: Wiley-VCH Verlag GmbH & Co. KGaA, 2007.
- [4] H. Kronmüller, “General micromagnetic theory,” in *Handbook of Magnetism and Advanced Magnetic Materials* (H. Kronmüller and S. Parkin, eds.), vol. 2, pp. 1–39, Chichester: John Wiley & Sons Ltd., 2007.
- [5] J. Fidler, R. W. Chantrell, T. Schrefl, and M. A. Wongsam, “Micromagnetics: Basic principles,” in *Encyclopedia of materials: Science and technology* (K. H. J. Buschow, M. C. Flemings, E. J. Kramer, P. Veysière, R. W. Cahn, B. Ilschner, and S. Mahajan, eds.), pp. 5642–5651, Amsterdam: Elsevier Ltd., 2001.
- [6] M. d’Aquino, *Nonlinear Magnetization Dynamics in Thin-films and Nanoparticles*. PhD thesis, Università degli Studi di Napoli Federico II, 2004.
- [7] D. V. Berkov, “Magnetization dynamics including thermal fluctuations: Basic phenomenology, fast remagnetization processes and transitions over high-energy barriers,” in *Handbook of Magnetism and Advanced Magnetic Materials* (H. Kronmüller and S. Parkin, eds.), vol. 2, pp. 1–29, Chichester: John Wiley & Sons Ltd., 2007.
- [8] C. Serpico, G. Bertotti, I. D. Mayergoyz, and M. d’Aquino, “Nonlinear magnetization dynamics in nanomagnets,” in *Handbook of Magnetism and Advanced Magnetic Materials* (H. Kronmüller and S. Parkin, eds.), vol. 2, pp. 1–34, Chichester: John Wiley & Sons Ltd., 2007.
- [9] U. Atxitia, D. Hinzke, and U. Nowak, “Fundamentals and applications of the Landau-Lifshitz-Bloch equation,” *J. Phys. D: Appl. Phys.*, vol. 50, pp. 1–23, 12 2017.
- [10] E. N. Kaufmann, *Characterization of Materials*, p. 522. New Jersey: John Wiley & Sons, Inc., 2003.

- [11] S. Petit, C. Baraduc, C. Thirion, U. Ebels, Y. Liu, M. Li, P. Wang, and B. Dieny, “Spin-torque influence on the high-frequency magnetization fluctuations in magnetic tunnel junctions,” *Phys. Rev. Lett.*, vol. 98, p. 077203, 7 2007.
- [12] S. Petit, N. de Mestier, C. Baraduc, C. Thirion, Y. Liu, M. Li, P. Wang, and B. Dieny, “Influence of spin-transfer torque on thermally activated ferromagnetic resonance excitations in magnetic tunnel junctions,” *Phys. Rev. B*, vol. 78, p. 184420, 11 2008.
- [13] C. Kittel, “Ferromagnetic resonance,” *J. Phys. Radium.*, vol. 12, pp. 291–302, 3 1951.
- [14] C. Kittel, “On the theory of ferromagnetic resonance absorption,” *Phys. Rev.*, vol. 73, pp. 155–161, 1 1948.
- [15] V. Vonsovskii, *Ferromagnetic Resonance*. Oxford: Pergamon Press Ltd., 1 ed., 1966.
- [16] L. F. Chen, C. K. Ong, C. P. Neo, V. V. Varadan, and V. K. Varadan, *Microwave Electronics: Measurement and Materials Characterization*, ch. 8.4, pp. 370–381. Chichester: John Wiley & Sons Ltd., 2004.
- [17] J. C. Sankey, *Microwave-frequency characterization of spin transfer and individual nanomagnets*. PhD thesis, Cornell University, 8 2007.
- [18] S. Urazhdin, personal communication, August 2016.
- [19] M. Farle, T. Silva, and G. Woltersdorf, “Spin dynamics in the time and frequency domain,” in *Magnetic Nanostructures: Spin Dynamics and Spin Transport* (H. Zabel and M. Farle, eds.), vol. 246 of *STMP*, pp. 37–83, Berlin, Heidelberg: Springer, 2013.
- [20] S. S. Kalarickal, P. Krivosik, M. Wu, C. E. Patton, M. L. Schneider, P. Kabos, T. J. Silva, and J. P. Nibarger, “Ferromagnetic resonance linewidth in metallic thin films: Comparison of measurement methods,” *J. Appl. Phys.*, vol. 99, p. 093909, 3 2006.
- [21] S. I. Kiselev, J. C. Sankey, I. N. Krivorotov, N. C. Emley, R. J. Schoelkopf, R. A. Buhrman, and D. C. Ralph, “Microwave oscillations of a nanomagnet driven by a spin-polarized current,” *Nature*, vol. 425, pp. 380–383, 9 2003.
- [22] V. Synogatch, N. Smith, and J. R. Childress, “Ferromagnetic resonance in tunnel junctions: Mag-noise and complex impedance analysis,” *J. Appl. Phys.*, vol. 93, pp. 8570–8572, 5 2003.
- [23] I. N. Krivorotov, N. C. Emley, J. C. Sankey, S. I. Kiselev, D. C. Ralph, and R. A. Buhrman, “Time-domain measurements of nanomagnet dynamics driven by spin-transfer torques,” *Science*, vol. 307, pp. 228–231, 1 2005.

- [24] “What is the difference between an equivalent time sampling oscilloscope and a real-time oscilloscope?,” Tech. Rep. 5989-8794EN, Keysight Technologies, 1 2019.
- [25] T. Zielinski, “Joint time-frequency resolution of signal analysis using Gabor transform,” *IEEE Trans. Instrum. Meas.*, vol. 50, p. 7164944, 10 2001.
- [26] L. Xue, C. Wang, Y.-T. Cui, J. A. Katine, R. A. Buhrman, , and D. C. Ralph, “Network analyzer measurements of spin transfer torques in magnetic tunnel junctions,” *Appl. Phys. Lett.*, vol. 101, p. 022417, 6 2012.
- [27] “Understanding and improving network analyzer dynamic range,” Tech. Rep. 5980-2778EN, Keysight Technologies, 9 2018.
- [28] C. Wang, Y.-T. Cui, J. A. Katine, R. A. Buhrman, and D. C. Ralph, “Time-resolved measurement of spin-transfer-driven ferromagnetic resonance and spin torque in magnetic tunnel junctions,” *Nature Phys.*, vol. 7, pp. 496–501, 6 2011.
- [29] K. Livesey, “Nonlinear behavior in metallic thin films and nanostructures,” in *Magnetism of Surfaces, Interfaces, and Nanoscale Materials* (R. Camley, Z. Celinski, and R. Stamps, eds.), vol. 5, ch. 4, pp. 169–214, The address of the publisher: Elsevier, 1 ed., 2016.
- [30] A. A. Tulapurkar, Y. Suzuki, A. Fukushima, H. Kubota, H. Maehara, K. Tsunekawa, D. D. Djayaprawira, N. Watanabe, and S. Yuasa, “Spin-torque diode effect in magnetic tunnel junctions,” *Nature*, vol. 438, pp. 339–342, 11 2005.
- [31] J. C. Sankey, P. M. Braganca, A. G. F. Garcia, I. N. Krivorotov, R. A. Buhrman, and D. C. Ralph, “Spin-transfer-driven ferromagnetic resonance of individual nanomagnets,” *Phys. Rev. Lett.*, vol. 96, p. 227601, 6 2006.
- [32] S. J. Blundell, *Magnetism in Condensed Matter*, ch. 6.7, pp. 127–139. Oxford Master Series in Condensed Matter Physics, Oxford: Oxford University Press, 2001.
- [33] C. Tannous and J. Gieraltowski, “The Stoner-Wohlfarth model of ferromagnetism: Static properties,” *arXiv e-prints*, p. physics/0607117, 7 2006.
- [34] E. Schlömann, “A sum rule concerning the inhomogeneous demagnetizing field in nonellipsoidal samples,” *J. Appl. Phys.*, vol. 33, pp. 2825–2826, 9 1962.
- [35] B. Azzerboni, G. Consolo, and G. Finocchio, “Micromagnetic modeling of nanoscale spin valves,” in *Handbook of Nanophysics: Nanoelectronics and Nanophotonics* (K. D. Sattler, ed.), ch. 8, pp. 1–17, New York: CRC Press, 2010.
- [36] T. Schrefl, G. Hrkac, S. Bance, D. Suess, O. Ertl, and J. Fidler, “Numerical methods in micromagnetics: Finite element method,” in *Handbook of Magnetism and*

Advanced Magnetic Materials (H. Kronmüller and S. Parkin, eds.), vol. 2, pp. 1–30, Chichester: John Wiley & Sons Ltd., 2007.

- [37] G. Sarau, *Spin-dependent transport in cobalt nanocontacts*. PhD thesis, Universität Duisburg-Essen, 4 2007.
- [38] M. J. Donahue and D. G. Porter, “Exchange energy formulations for 3D micromagnetics,” *Phys. B: Conden. Matt.*, vol. 343, pp. 177–183, 1 2004.
- [39] D. V. Berkov and N. L. Gorn, “Numerical simulation of quasistatic and dynamic remagnetization processes with special applications to thin films and nanoparticles,” in *Handbook of Advanced Magnetic Materials: Nanostructural Effects* (Y. Liu, D. Sellmyer, and D. Shindo, eds.), vol. 1, ch. 10, pp. 421–507, New York: Springer, 2006.
- [40] J. Fischbacher, A. Kovacs, H. Oezelt, T. Schrefl, L. Exl, J. Fidler, D. Suess, N. Sakuma, M. Yano, A. Kato, and T. S. A. Manabe, “Nonlinear conjugate gradient methods in micromagnetics,” *AIP Adv.*, vol. 7, p. 045310, 4 2017.
- [41] E. Auerbach, S. Gider, G. Albuquerque, and D. Mauri, “Influence of parasitic capacitance on single and dual 2-D magnetic recording read head performance,” *IEEE Trans. Magn.*, vol. 52, p. 3000804, 7 2016.
- [42] J. Heidmann and A. M. Taratorin, “Magnetic recording heads,” in *Handbook of Magnetic Materials* (K. H. J. Buschow, ed.), vol. 19, ch. 1, pp. 1–105, Amsterdam: Elsevier, 1 ed., 2011.
- [43] “Fundamentals of vector network analysis,” Tech. Rep. Version 1.1, Rohde & Schwarz.
- [44] E. Jang, “HDD-level electrostatic discharge (ESD) failure voltage of tunneling magnetoresistive (TMR) heads,” in *Proc. 29th Electrical Overstress/Electrostatic Discharge Symposium*, IEEE, 8 2007.
- [45] J.-G. Zhu and C. Park, “Magnetic tunnel junctions,” *Mater. Today*, vol. 9, pp. 36–45, 11 2006.
- [46] G. Vallejo-Fernandez, L. E. Fernandez-Outon, and K. O’Grady, “Antiferromagnetic grain volume effects in metallic polycrystalline exchange bias systems,” *J. Phys. D: Appl. Phys.*, vol. 41, p. 112001, 5 2008.
- [47] A. Tuggle, S. Gider, D. Mauri, and M. Ho, “A dual free layer sensor with side shields,” *IEEE Trans. Magn.*, vol. 48, pp. 3547–3550, 11 2012.

- [48] Y. Zhou, “Low noise dual free-layer magnetoresistive sensor with coupled resonance,” *J. Appl. Phys.*, vol. 105, p. 07B708, 11 2009.
- [49] Y. Zhou, K. Zhang, Y.-H. Chen, T. Zhao, and M. Dovek, “Low noise magnetoresistive sensor utilizing magnetic noise cancellation.” U.S. Patent 8,031,445.
- [50] E. Auerbach, S. Gider, G. Albuquerque, N. Leder, H. Arthaber, and D. Süss, “High-frequency modes of the dual free layer sensor,” in *Proc. IEEE International Magnetism Conference*, IEEE, 4 2017.
- [51] T. Zhao, H.-C. Wang, Y.-C. Zhou, M. Li, and K. Zhang, “Tmr device with novel free layer structure.” U.S. Patent 9,437,812.
- [52] H.-C. Wang, T. Zhao, K. Zhang, and M. Li, “Magnetic memory cell.” U.S. Patent 8,335,105.
- [53] S. Yuasa, “Tunneling magnetoresistance: Experiment (MgO magnetic tunnel junctions),” in *Handbook of Spin Transport and Magnetism* (E. Y. Tsymbal and I. Žutić, eds.), ch. 11, pp. 217–231, Florida: CRC Press, 1 ed., 8 2012.
- [54] K. D. Belashchenko and E. Y. Tsymbal, “Tunneling magnetoresistance: Theory,” in *Handbook of Spin Transport and Magnetism* (E. Y. Tsymbal and I. Žutić, eds.), ch. 12, pp. 233–250, Florida: CRC Press, 1 ed., 8 2012.
- [55] H. Jaffrès, D. Lacour, F. N. V. Dau, J. Briatico, F. Petroff, and A. Vaurès, “Angular dependence of the tunnel magnetoresistance in transition-metal-based junctions,” *Phys. Rev. B*, vol. 64, p. 064427, 7 2001.
- [56] M. Tsoi, “Spin torque effects in magnetic systems: Experiment,” in *Handbook of Spin Transport and Magnetism* (E. Y. Tsymbal and I. Žutić, eds.), ch. 7, pp. 137–156, Florida: CRC Press, 1 ed., 8 2012.
- [57] E. Auerbach, S. Gider, G. Albuquerque, N. Leder, H. Arthaber, and D. Süss, “High-frequency modes of the dual free layer sensor.” IEEE International Magnetism Conference, 9 2017.
- [58] M. d’Aquino, C. Serpico, G. Miano, and C. Forestiere, “A novel formulation for the numerical computation of magnetization modes in complex micromagnetic systems,” *J. Comput. Phys.*, vol. 228, pp. 6130–6149, 9 2009.
- [59] N. Smith, “Micromagnetic modeling of magnoise in magnetoresistive read sensors,” *J. Magn. Magn. Mater.*, vol. 321, pp. 531–538, 3 2009.

- [60] D. Berkov, E. Auerbach, H. Zhivomirov, N. Leder, and H. Arthaber, “Spin-torque-induced instability in MgO-based magnetic tunnel junctions.” Joint European Magnetic Symposia, 9 2018.
- [61] “Basic oscilloscope fundamentals,” Tech. Rep. 5989-8064EN, Keysight Technologies, 12 2017.
- [62] J. Benesty, M. M. Sondhi, and Y. Huang, *Springer Handbook of Speech Processing*. Berlin: Springer, 2008.
- [63] B. Boashash, *Time-Frequency Signal Analysis and Processing: A Comprehensive Reference*. Kidlington: Elsevier Ltd., 2003.
- [64] F. Hlawatsch and F. Auger, *Time-Frequency Analysis*. London: ISTE Ltd., 2008.
- [65] J. O. Smith and X. Serra, “PARSHL: An analysis/synthesis program for non-harmonics sound based on a sinusoidal representation.” 1987.
- [66] T. Dutoit and F. Marqués, *Applied Signal Processing: A MATLAB[®]-Based Proof of Concept*. New York: Springer, 2009.
- [67] D. E. Root, J. Verspecht, J. Horn, and M. Marcu, *X-Parameters: Characterization, Modeling, and Design of Nonlinear RF and Microwave Components*. Cambridge, United Kingdom: University Printing Press, 2013.
- [68] R. A. Groves, “AC measurement techniques,” in *Measurement and Modeling of Silicon Heterostructure Devices* (J. D. Cressler, ed.), ch. 4.2, pp. 2–10, Florida: CRC Press, 1 ed., 2007.
- [69] R. B. Randall, *Frequency analysis*, ch. 2.2.1, p. 23. Nærum, Denmark: Brüel & Kjær, 3 ed., 9 1987.
- [70] R. E. Ziemer and W. H. Tranter, *Principles of communications: Systems, modulation, and noise*, ch. 2.6.4, pp. 201–213. USA: John Wiley & Sons Ltd., 7 ed., 2014.
- [71] “VNA help: One-port error model.” <http://www.vnahelp.com/tip20.html>. Online; accessed March 13, 2019.
- [72] J. C. Sankey, Y.-T. Cui, J. Z. Sun, J. C. Slonczewski, R. A. Buhrman, and D. C. Ralph, “Measurement of the spin-transfer-torque vector in magnetic tunnel junctions,” *Nat. Phys.*, vol. 4, pp. 67–71, 1 2008.

- [73] E. Auerbach, N. Leder, S. Gider, and H. Arthaber, “Characterization of MgO-based magnetic tunnel junctions’ nonlinear ferromagnetic resonance modes,” *IEEE Trans. Magn.*, vol. 54, p. 3400205, 2 2018.
- [74] “Spectrum analysis basics,” Tech. Rep. 5952-0292, Keysight Technologies, 11 2016.
- [75] D. V. Berkov and J. Miltat, “Spin-torque driven magnetization dynamics: Micro-magnetic modeling,” *J. Magn. Magn. Mater.*, vol. 320, pp. 1238–1259, 4 2008.
- [76] J. C. Slonczewski, “Currents and torques in metallic magnetic multilayers,” *J. Magn. Magn. Mater.*, vol. 247, pp. 324–338, 6 2002.
- [77] J. Xiao, A. Zangwill, and M. D. Stiles, “Boltzmann test of Slonczewski’s theory of spin-transfer torque,” *Phys. Rev. B*, vol. 70, p. 172405, 11 2004.
- [78] E. Kowalska, A. Fukushima, V. Sluka, C. Fowley, A. Kákay, Y. Aleksandrov, J. Lindner, J. Fassbender, S. Yuasa, and A. M. Deac, “Tunnel magnetoresistance angular and bias dependence enabling tuneable wireless communication,” *arXiv e-prints*, p. arXiv:1808.10812, 8 2018.
- [79] A. Kalitsov, P.-J. Zermatten, F. Bonell, G. Gaudin, S. Andrieu, C. Tiusan, M. Chshiev, and J. P. Velev, “Bias dependence of tunneling magnetoresistance in magnetic tunnel junctions with asymmetric barriers,” *J. Phys.: Condens. Matter.*, vol. 25, p. 496005, 11 2013.
- [80] A. Kalitsov, W. Silvestre, M. Chshiev, and J. P. Velev, “Spin torque in magnetic tunnel junctions with asymmetric barriers,” *Phys. Rev. B*, vol. 88, p. 104430, 9 2013.
- [81] S. Boyn, J. Sampaio, V. Cros, J. Grollier, A. Fukushima, H. Kubota, K. Yakushiji, and S. Yuasa, “Twist in the bias dependence of spin torques in magnetic tunnel junctions,” *Phys. Rev. B*, vol. 93, p. 224427, 6 2016.
- [82] J. C. Pedro and N. B. Carvalho, *Intermodulation Distortion in Microwave and Wireless Circuits*, ch. 3, pp. 73–196. Norwood: Artech House, 1 ed., 2003.
- [83] J.-G. Zhu and X. Zhu, “Spin transfer induced noise in CPP read heads,” *IEEE Trans. Magn.*, vol. 40, pp. 182–188, 2 2004.
- [84] D. Berkov and N. Gorn, “Transition from the macrospin to chaotic behavior by a spin-torque driven magnetization precession of a square nanoelement,” *Phys. Rev. B*, vol. 71, p. 052403, 2 2005.

- [85] E. Auerbach, N. Leder, S. Gider, D. Suess, and H. Arthaber, “Characterization of dynamic nonlinear effects in MTJ-based magnetic sensors,” in *Proc. Integrated Nonlinear Microwave and Millimetre-wave Circuits Workshop*, IEEE, 4 2017.
- [86] J. C. Pedro and N. B. Carvalho, *Intermodulation Distortion in Microwave and Wireless Circuits*, ch. 2, pp. 25–72. Norwood: Artech House, 1 ed., 2003.
- [87] N. B. Carvalho and D. Schreurs, *Microwave and Wireless Measurement Techniques*, ch. 3, pp. 133–165. The Cambridge RF and Microwave Engineering Series, Cambridge: Cambridge University Press, 2013.
- [88] R. Minihold and R. Wagner, “Measuring the nonlinearities of RF amplifiers using signal generators and a spectrum analyzer,” Tech. Rep. 5.2014-1MA71-2e, Rohde & Schwarz.
- [89] K. S. Kundert, *The Designer’s Guide to SPICE and Spectre[®]*, ch. 5, pp. 251–258. The Designer’s Guide Book Series, Norwell: Kluwer Academic Publishers, 1995.
- [90] K. A. Remley, D. F. Williams, D. Schreurs, and J. Wood, “Simplifying and interpreting two-tone measurements,” *IEEE Trans. Microw. Theory Tech.*, vol. 52, pp. 2576–2584, 11 2004.
- [91] J. H. K. Vuolevi, T. Rahkonen, and J. P. A. Manninen, “Measurement technique for characterizing memory effects in RF power amplifiers,” *IEEE Trans. Microw. Theory Tech.*, vol. 49, pp. 1383–1389, 8 2001.
- [92] E. Auerbach, B. Pichler, N. Leder, S. Gider, and H. Arthaber, “Nonlinear characterization of magnetic read sensors using a nonlinear vector network analyzer.” 29th Magnetic Recording Conference, 8 2018.
- [93] E. Auerbach, D. Berkov, B. Pichler, N. Leder, S. Gider, and H. Arthaber, “Injection locking at fractional frequencies of magnetic tunnel junction (MTJ)-based read sensors’ ferromagnetic resonance modes.” manuscript in preparation, 2019.
- [94] “Nonlinear vector network analyzer (NVNA),” Tech. Rep. 5989-8575EN, Keysight Technologies, 5 2018.
- [95] K. A. Remley, “Practical applications of nonlinear measurements,” in *Proc. 73rd ARFTG Microwave Measurement Conference*, pp. 1–15, IEEE, 10 2009.
- [96] P. Roblin, *Nonlinear RF Circuits and Nonlinear Vector Network Analyzers*. Cambridge: Cambridge University Press, 1 ed., 7 2011.
- [97] W. V. Moer and L. Gomme, “NVNA versus LSNA: enemies or friends?,” *IEEE Microw. Mag.*, vol. 11, pp. 1238–1259, 4 2008.

- [98] A. Brataas, A. D. Kent, and H. Ohno, “Current-induced torques in magnetic materials,” *Nat. Mater.*, vol. 11, pp. 372–381, 4 2012.
- [99] L. D. Landau and E. M. Lifshitz, *Course of Theoretical Physics: Mechanics*, vol. 1, ch. 29, pp. 87–92. Oxford, UK: Butterworth-Heinemann, 3 ed., 1976.
- [100] J. C. Slonczewski, “Current-driven excitation of magnetic multilayers,” *J. Magn. Magn. Mater.*, vol. 159, pp. L1–L7, 6 1996.
- [101] N. Smith, M. J. Carey, and J. R. Childress, “Measurement of Gilbert damping parameters in nanoscale CPP-GMR spin valves,” *Phys. Rev. B*, vol. 81, p. 184431, 5 2010.
- [102] M. Pauselli, A. Stankiewicz, Y. Zhang, and G. Carlotti, “Magnetic noise and spin-wave eigenmodes in a magnetic tunnel junction read head,” *IEEE Trans. Magn.*, vol. 53, p. 4400606, 11 2017.
- [103] M. R. Schroeder, “Synthesis of low-peak-factor signals and binary sequences with low autocorrelation,” *IEEE Trans. Inf. Theory*, vol. 16, pp. 85–89, 1 1970.
- [104] E. Van der Ouderaa, J. Schoukens, and J. Renneboog, “Peak factor minimization of input and output signals of linear systems,” *IEEE Trans. Ins. Meas.*, vol. 37, pp. 201–213, 6 1988.
- [105] N. Smith and P. Arnett, “White-noise magnetization fluctuations in magnetoresistive heads,” *Appl. Phys. Lett.*, vol. 78, p. 1448, 1 2001.
- [106] J. B. Mohammadi, J. M. Jones, S. Paul, B. Khodadadi, C. K. A. Mewes, T. Mewes, and C. Kaiser, “Broadband ferromagnetic resonance characterization of anisotropies and relaxation in exchange-biased IrMn/CoFe bilayers,” *Phys. Rev. B*, vol. 95, p. 064414, 2 2017.
- [107] J. C. Slonczewski, “Currents, torques, and polarization factors in magnetic tunnel junctions,” *Phys. Rev. B*, vol. 71, p. 024411, 1 2005.
- [108] I. N. Krivorotov, D. V. Berkov, N. L. Gorn, N. C. Emley, J. C. Sankey, D. C. Ralph, and R. A. Buhrman, “Large-amplitude coherent spin waves excited by spin-polarized current in nanoscale spin valves,” *Phys. Rev. B*, vol. 76, p. 024418, 7 2007.
- [109] W. H. Rippard, A. M. Deac, M. R. Pufall, J. M. Shaw, M. W. Keller, S. E. Russek, G. E. W. Bauer, and C. Serpico, “Spin-transfer dynamics in spin valves with out-of-plane magnetized CoNi free layers,” *Phys. Rev. B*, vol. 81, p. 014426, 1 2010.

- [110] D. V. Berkov and N. L. Gorn, “Spin-torque driven magnetization dynamics in a nanocontact setup for low external fields: Numerical simulation study,” *Phys. Rev. B*, vol. 80, p. 064409, 8 2009.
- [111] B. K. Shivamoggi, *Nonlinear Dynamics and Chaotic Phenomena: An Introduction*. Dordrecht, Netherlands: Springer, 2 ed., 2014.
- [112] D. V. Berkov and N. L. Gorn, “Magnetization precession due to a spin-polarized current in a thin nanoelement: Numerical simulation study,” *Phys. Rev. B*, vol. 72, p. 094401, 9 2005.
- [113] U. Zölzer, *DAFX: Digital Audio Effects*. Chichester: John Wiley & Sons Ltd., 2011.
- [114] S. V. Vaseghi, *Advanced Digital Signal Processing and Noise Reduction*. Chichester: John Wiley & Sons Ltd., 2008.
- [115] D. G. Manolakis and V. K. Ingle, *Applied Digital Signal Processing: Theory and Practice*. New York: Cambridge University Press, 2011.
- [116] K. Leong, J. Mazierska, and J. Krupka, “Measurements of unloaded Q-factor of transmission mode dielectric resonators,” in *Proc. IEEE MTT-S International Microwave Symposium*, pp. 1639–1642, IEEE, 8 1997.
- [117] P. J. Petersan and S. M. Anlage, “Measurement of resonant frequency and quality factor of microwave resonators: Comparison of methods,” *J. Appl. Phys.*, vol. 84, p. 3392, 9 1998.
- [118] E. K. Semenova, F. Montoncello, S. Tacchi, G. Dürr, E. Sirotkin, E. Ahmad, M. Madami, G. Gubbiotti, S. Neusser, D. Grundler, F. Y. Ogrin, R. J. Hicken, V. V. Kruglyak, D. V. Berkov, N. L. Gorn, and L. Giovannini, “Magnetodynamical response of large-area close-packed arrays of circular dots fabricated by nanosphere lithography,” *Phys. Rev. B*, vol. 87, p. 174432, 5 2013.
- [119] “Convert from dBm.” <http://www.cantwellengineering.com/calculator/convert/dBm>. Online; accessed March 14, 2019.
- [120] A. L. Shenkman and M. Zarudi, *Circuit Analysis for Power Engineering Handbook*, p. 652. Boston: Kluwer Academic Publishers, 1998.